Fault Reactivation Potential of the Aurora Area, Northern North Sea: Implications for Successful Storage of CO_2

Haakon C. Nedberg

Master Thesis in Geosciences
Structural Geology and Tectonics
60 credits

Department of Geosciences
Faculty of Mathematics and Natural Sciences

UNIVERSITY OF OSLO

May 2022

Fault Reactivation Potential of the Aurora Area. Northern North Sea: Implications for Successful Storage of CO_2

Supervisors: Alvar Braathen and Elin Skurtveit

This work is published digitally on DUO – Digitale Utgivelser ved UiO

https://www.duo.uio.no/

Printed at: Reprosentralen, Universitetet I Oslo

Acknowledgements

I want to express my gratitude to my principal supervisor Alvar Braathen and co-supervisor Elin Skurtveit for their encouragement, guidance and thorough feedback throughout the project. I would also like to thank past supervisors Mark J. Mulrooney and Emma H. Michie for their contributions while employed at UiO.

A most sincere thanks to Johnathon L. Osmond, Nora Holden, and Muhammad Hassaan for their invaluable assistance and guidance with the Petrel and Move software and their contagious enthusiasm.

A final and most personal thank you to my friends and fellow students at the Geoscience M.Sc. program at UiO, for adding so much fun and colour to the world, and for making it enjoyable to work on the thesis.

Haakon C. Nedberg

Oslo, Norway, May 16th, 2022

Preface

This master's thesis (ECTS 60) is submitted to the Department of Geosciences, University of Oslo (UiO), in the candidacy for the Master of Science program Structural Geology and Tectonics (ECTS 120). The main supervisor is Professor Alvar Braathen and Senior researcher Elin Skurtveit (UiO, NGI).

This thesis is a contribution to the University of Oslo and the Norwegian CCS Research Center (NCCS), under Task 9 – Structural De-risking, and the associated FRISK project (NGI).

Seismic data and well data are courtesy of the NPD Diskos archive and the Northern Lights project (Total E&P Norge AS, Equinor, and A/S Norske Shell). Software is courtesy of Schlumberger (Petrel E&P Software Platform) and Petroleum Experts (Move Suite).

Abstract

Carbon capture and storage (CCS) is planned by the Northern Lights project for the Aurora area in the northern North Sea. Targeted storage complexes within the Lower Jurassic Dunlin Group are represented by the Cook and Johansen reservoir units, with the overlying Drake Formation as the intended seal. Above, the producing Troll oil and gas fields utilize the Sognefjord Formation as its reservoir, whereas the Draupne and Shetland formations act as primary and tertiary seals. The Aurora area is bounded by 1st-order fault zones Svartalv and Tusse, between which numerous 2nd-order faults intersect and displace the storage complexes.

A challenge toward securely trapping CO_2 is to evaluate the fault systems within the targeted storage complex. To achieve geological control of selected faults within the Aurora area a detailed geomodel is created using the GN10M1 3D seismic survey plus well data. Faults are then divided into four intervals of reservoirs and cap rocks. Fault rocks within the intervals are assigned lithological properties derived from their respective host rocks, such as cohesion and coefficient of friction. The fault models are then subjected to four methods of assessing reactivation potentials: slip tendency, dilation tendency, slip stability, and fracture stability. Critical perturbation pressure is calculated, the likely mode of failure is determined, and their correlation with fault dip, strike, and situ stresses is investigated. It is concluded that the majority of fault segments within the storage complexes would fail as a mix between hybrid and shear (Mode II/III). Consequently, reactivation of faults might create conduits for fluid flow, thus jeopardizing the integrity of the storage complexes.

The fault reactivation potential analysis herein shows that the Aurora area predominantly exhibits a significant tolerance to increases in pressure due to CO_2 injection. However, a considerable risk of reactivation lies within fault segments intersecting the proposed cap rock, the Drake Formation. Depending on the nature of the fault rocks within the Drake fault segments, their tolerance to increased pressure can be perilously low. A sensitivity analysis is completed to test the analyses dependence on cohesion as a fault rock property. Herein it is shown that cohesion has a significant effect on the calculated critical perturbation pressure, i.e. the amount of extra pressure needed to put a fault segment into a critically stressed state, where the faults might leak fluids. Areas of considerably high risk within the Drake interval fault segments are highlighted and compared to previously determined storage complexes within the Aurora area.

Table of Contents

1 Introduction

This thesis provides a high-resolution fault model and detailed reactivation potential analysis of selected faults within the Aurora storage sites. The study discusses the likelihood of faults being reactivated by an increase in pressure due to injected CO2. The focus is on fault segments within the Drake Formation, the intended cap rock for the Northern Lights project. This chapter introduces the main research objectives, the study area, previous research on faults within or in the proximity of the Aurora storage sites, and the motivation for the study.

1.1 Research Objectives

To successfully execute a carbon capture and storage (CCS) project, a suitable subsurface storage site is required to store CO_2. Such a site usually consists of high porosity and permeable sandstones structurally enclosed with a low permeability caprock and bounded either stratigraphically or by sealing faults. One of the challenges towards securely trapping CO_2 within a prospect is to evaluate fault systems surrounding the target storage complex. Induced pressure from injected CO_2 might significantly alter the resolved in-situ pressure over time, and so the vulnerability of the storage complexes cannot be neglected. Pre-existing weaknesses, such as faults and fractures, that are preferentially aligned with the in-situ stress field are liable to get critically stressed and subsequently reactivate if the extra pressure reaches a threshold. A critically stressed fault is likely to leak, and the event of fault reactivation can create conduits that allow fluids to escape out of the storage unit. Fault reactivation analysis considers several parameters when assessing reactivation potential such as orientation and magnitude of in-situ stresses, fault location, geometry and orientation, hydrostatic or induced pressure gradients (where higher pressure favours reactivation), and the geomechanical properties of the fault rocks, such as cohesion and coefficient friction (van Ruth et al., 2006). To advance the geological control and assess the likelihood of fault reactivation in the Aurora area, the main objectives of this study are to:

i) Advance geological control of 1^{st}- and 2^{nd}-order faults within the Aurora area by investigating fault scale, displacement, dip angle and strike orientation.

ii) Use literature to determine the orientation and magnitude of the in-situ stresses in the Aurora area as well as the lithology and geomechanical properties of inherent fault rocks.

iii) Utilize four methods of assessing fault reactivation potential and investigate links between critical perturbation pressure, failure mode, fault rock composition, fault dip angle, strike orientation, and in-situ pressures.

iv) Especially investigate the Drake Formation, the intended cap rock, considering increased pressures due to CO_2 injection and the integrity of the storage complexes.

v) Detect and highlight zones of considerably high risk of fault reactivation and determine the faults' tolerance to increased pressure within the zones.

These objectives will be achieved by creating a high-resolution 3D fault model of faults within the Aurora area, and then splitting the faults into separate segments of cap rock and reservoir rock intervals based on 3D mapping of two reservoir-quality successions, the Sognefjord and Cook formations, and two cap rock-quality successions, the Shetland and Drake formations. Because the Drake Formation is intended as the cap rock for the Northern Lights project, this formation will be more thoroughly investigated. The fault models will then be subjected to four different types of reactivation analysis: slip tendency, dilation tendency, slip stability and fracture stability. The faults' likelihood of reactivation and eventual failure mode will be determined and areas of high risk will be detected and highlighted.

1.2 The Aurora Area

The Aurora area and exploitation license (EL001) is situated within the Horda Platform, immediately south of the oil and gas producing Troll West and East fields (Figures 1.1 and 1.2). The field is also in proximity to the Oseberg East, Veslefrikk and Brage hydrocarbon fields to the west, and to the Smeaheia CCS prospects Alpha, Beta and Gamma to the east and northeast (Figures 1.1 and 1.2). The Aurora area is structurally within a westward tilted fault block bounded by two major, thick-skinned fault zones (termed 1st-order), namely the Tusse Fault Zone (TFZ) to the east and Svartalv Fault Zone (SFZ) to the west (Figure 1.1). Numerous smaller thin-skinned faults intersect the sedimentary successions between the two major fault zones, mainly abutting into or being isolated from the two.

Among the sedimentary successions in the Aurora area are the Upper Jurassic-Lower Cretaceous Viking Group and the Lower Jurassic Dunlin Group. While the Viking Group comprises the main reservoir and cap rock formations exploited in the Troll oil and gas fields, the deeper Dunlin Group has been suggested as a CO_2 storage complex by the Norwegian authorities (Halland et al., 2014). The Dunlin Group storage complex accommodates the clay-rich and regionally sealing Drake Formation, which directly overlies the saline aquifer sandstones of the Cook and Johansen Formations (Gassnova, 2011; Thompson et al., 2022).

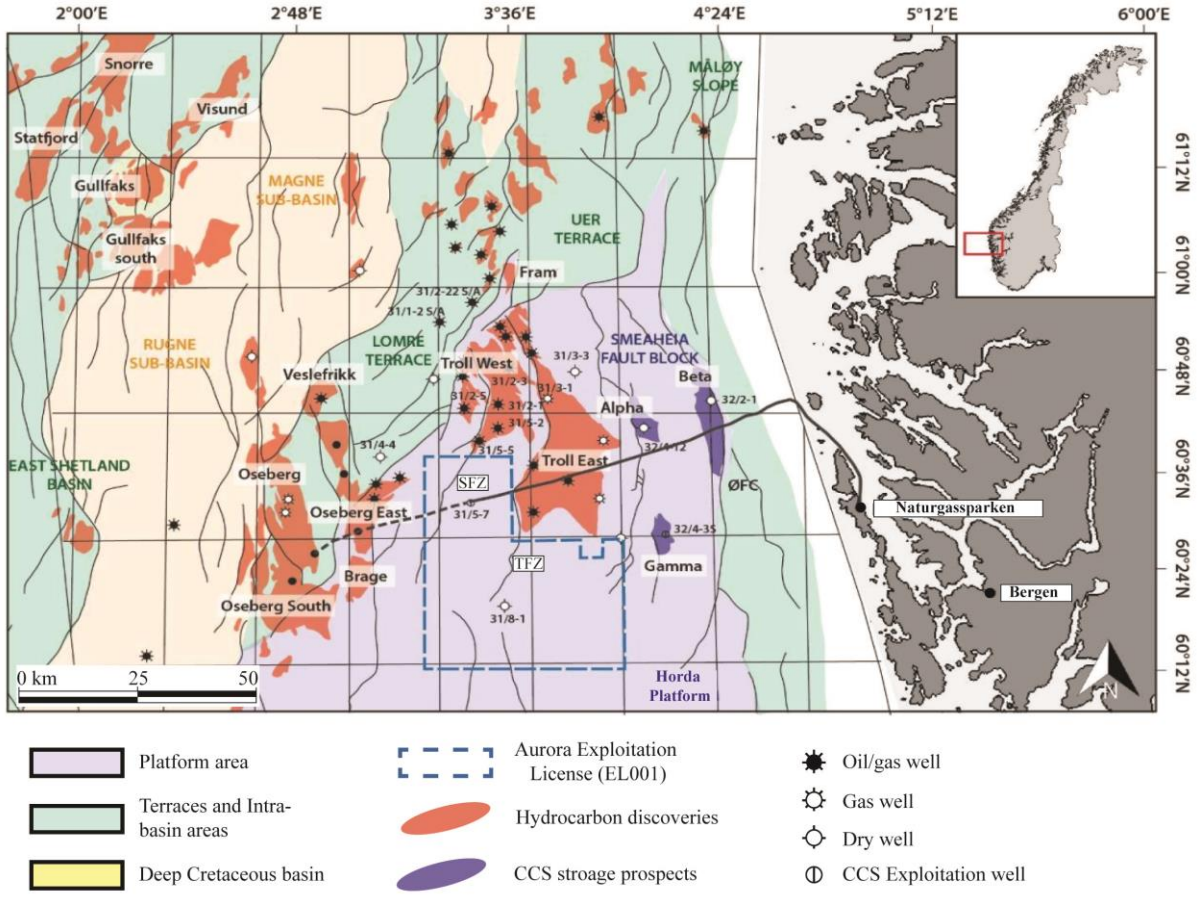

Figure 1.1: Regional map presenting the location of the Aurora Exploitation License (EL001) and its spatial relationship with significant structural features as well as outlines of hydrocarbon discoveries and other CCS prospects. Structural elements and outlines are compiled from the NPD and Wu et al. (2021). Modified from Holden (2021). Note that all available wells from the NPD were included in this map and that fault zones explored in this study are highlighted. Abbreviations: TFZ = Tusse Fault Zone, SFZ = Svartalv Fault Zone, ØFC = Øygarden Fault Complex.

To investigate the actual storage possibilities and reservoir quality within the Aurora storage complex, the Northern Lights project drilled the first purely CCS well on the Norwegian Continental Shelf (NCS): the 31/5-7 (EOS) well. The well was used to investigate the Dunlin

Group succession and to resolve in-situ pressures around the well. The investigation subsequently confirmed both storage resources and integrity within the Dunlin Group and proved the area as that of a relaxed/normal-stress tectonic character (Thompson et al., 2022).

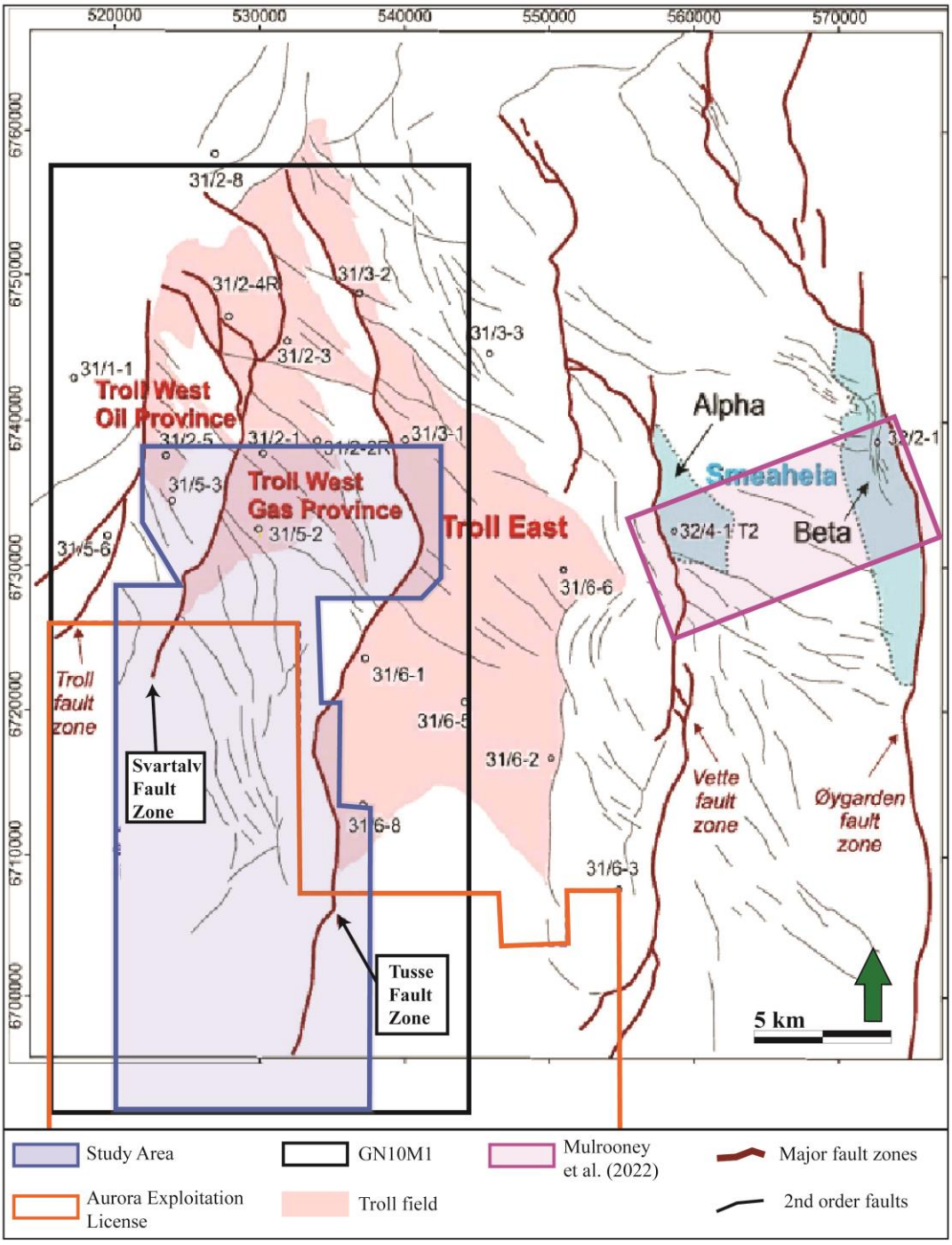

Figure 1.2: Regional map showcasing the spatial relationship between the GN10M1 seismic survey, the Aurora Exploitation License (EL001) and the study area. The neighbouring Smeaheia area, as investigated by Mulrooney et al. (2022), Svartalv and Tusse Fault Zones are highlighted. Note that wells are displayed with NPD symbols and names, the Alpha and Beta CO_2-storage prospects are shown in blue, and that the figure shows the northern part of the Aurora field. Modified from Wu et al. (2021).

The study area herein was designed to encompass all relevant fault zones and selected smaller-scale faults within the Aurora Exploitation License and the extent of the GN10M1 3D seismic survey (Figure 1.2). The study area encompasses the southern fault tip of the Tusse Fault Zone in the south and southern parts of the Troll West and East oil and gas fields in the north. To the east and west, the study area is extended to accommodate as much of the Tusse and Svartalv fault zones as the GN10M1 allows (Figure 1.2). Central areas within the study area contain the thin-skinned fault population. Careful consideration when choosing the extent of the study area allows a more thorough investigation of all manner of fault types within the Aurora Exploitation License, and so achieving a complete assessment of fault reactivation potential within the area.

1.3 Research Background

Considering the study area's proximity to the Troll oil and gas fields, the area has been extensively investigated and described in previous research (e.g. Bolle, 1992; Faleide et al., 2015; Spencer & Larsen, 1990; Ziegler, 1992). Recently, a plethora of works on structural characterization and geological evolution has been made through contributions by great scientists. Examples of such studies include the assessment of the Troll East and West fields by Bretan et al. (2011), Whipp et al. (2014) and Duffy et al. (2015) where across-fault seals, CO_2 migration pathways, fault growth, timing and interaction styles were determined. The Smeaheia fault block was extensively investigated by Harris (2019), Mulrooney et al. (2020) and Wu et al. (2021), identification of structural traps and seals on the Horda Platform was performed by Osmond et al. (2022) and structural characterization of the Aurora Storage Complex was completed by Holden (2021), who also investigated post-charge migration pathways of CO_2 into structural closures. Resolving of in-situ pressures around the 31/5-7 EOS well was done by Thompson et al. (2022). Considering this study, Mulrooney et al.'s (2022) fault reactivation analysis of the neighbouring Smeaheia fault block was of particular importance and provided opportunities to compare results (see Figure 1.2). Many subjects related to characterizing and investigating potential CO_2 storage sites have been covered by these endeavours. However, to the author's knowledge, no fault reactivation potential has previously been investigated or calculated for the faults within the Aurora Exploitation License.

The theoretical foundation of this study is based on the notion that pre-existing weaknesses such as faults and fractures are prone to reactivate if they are preferentially aligned with the in-

situ stress regime (e.g. Sibson, 1985). The theory behind fault reactivation is extensively researched by authors such as Sibson (1985, 1995) and Wiprut et al. (2000, 2002). Research on the influence of fault reactivation when injecting CO_2 by van Ruth (2006) and Deng (2017) are major contributors as well as works on fault rocks such as Fisher & Knipe (1998), Dewhurst & Jones (2002, 2003), Haines et al. (2014) and Pei et al. (2015). The theories behind the reactivation analyses utilized in this study were developed by: Morris et al. (1996), who defined slip tendency (T_s), Ferrill et al. (2010), who defined dilation tendency (T_d) and Mildren et al. (2005) who defined fracture stability (F_s). No clear definition was found for slip stability (S_s), although to the author's knowledge the method was first used to assess fault reactivation along a dormant normal fault in the northern North Sea (see: Wiprut & Zoback, 2000).

1.4 Political Background

This thesis is motivated by IPCC's Third Assessment Report which states that a significant portion of the observed warming of our planet over the past 50 years is traceable to human activities (Metz et al., 2005). The influence of our endeavours, of which emissions of carbon dioxide (CO_2) undeniably is the dominant factor, is expected to continuously affect atmospheric composition into the future. In an effort to address this growing issue the European Commission outlined a goal of reducing anthropogenic emission of greenhouse gasses by 80-90% by 2050 (European Commission, 2018). A significant amount of technological advancement and adjustments are necessary, in which Norway is a key contributor, especially in carbon capture and storage (CCS). CCS will prove an essential contribution to reach this target, as it provides the option of capturing and storing CO2 physically, preventing it from ever reaching the atmosphere. In CCS, waste CO_2 is compressed and transported directly from its source of production into feasible subsurface sites of storage, i.e., storage formations and reservoirs, saline aquifers, and previously exploited fields of hydrocarbons.

To remain a front-runner in reaching the Paris Agreement, Norway established an ambitious target to reduce its greenhouse gas emissions by 50-55% of 1990 levels by 2030 (Klimaloven, 2021). This target will not be achievable without CCS. Fortunately, Norway has exceptional experience with CCS as several prospects offshore of Norway already is being utilized; Sleipner, since 1996, in the North Sea (Furre et al., 2017), and Snøhvit, since 2008, in the Barents Sea (Eiken et al., 2011). These projects serve to prove CCS as a realistic and

economically valuable technology to Norway and the world. Despite these efforts, a considerable amount of new sequestration projects will be necessary to reach the climate goals.

In 2020 the Government of Norway issued a white paper to the Storting recommending the funding of a full-scale CCS project, aptly named Longskip (Norwegian Ministry of Petroleum Energy, 2020). The project was subsequently approved in 2021 (Regjeringen.no, 2021). Longskip aims to develop: i) carbon capture at the Norcem AS cement factory, ii) transport to a suitable onshore storage facility at Øygarden, and iii) the subsequent sub-surface injection into the storage prospect under the name Aurora Exploitation License (EL001), in the Aurora area. While the capture part of the project is handled by Norcem AS, the remaining transport and storage components will be handled by the Northern Lights project, a consortium between Equinor, Shell and TotalEnergies. To further aid the realization of the Longskip project the Research Council of Norway is supported by the Centre for Environmental-Friendly Energy Research and the Norwegian CCS Research Centre (NCCS). This international research cooperation aims to fast-track CCS deployment through industry-driven, science-based innovation by investigating all major obstacles to full-scale CCS projects and ultimately ensuring the safety of CO2 storage (NCCS, 2020).

A recent blossoming of NCCS-approved spin-offs has prompted the forming of the FRISK project (NGI, 2021). FRISK focuses on the risks related to faults interacting with reservoirs under consideration for CO2 storage, intending to reduce uncertainties in fault-related leakage risk. Furthermore, FRISK seeks to characterize and quantify fault complexities and develop an improved fault derisking framework that includes dynamic pressure changes and along-fault fluid migration. To cover additional difficulties entailed in a full-scale CCS endeavour, NCCS was divided into task forces with specific assignments. Especially, the Structural Derisking (Task 9) in which UiO is a major contributor, aims to reduce risks related to injecting and storing CO2 by investigating faults and improving models for fault reactivation (NCCS, 2021). NCCS' Task 9 feeds its data into FRISK, and so the projects are solidly integrated.

2 Geological Setting

This chapter describes the geographical placement and geological history of the region in which the study area resides – the northern North Sea (Figure 2.1). The regional structure and timeline of events that developed the basin and the inherent sedimentary successions are presented.

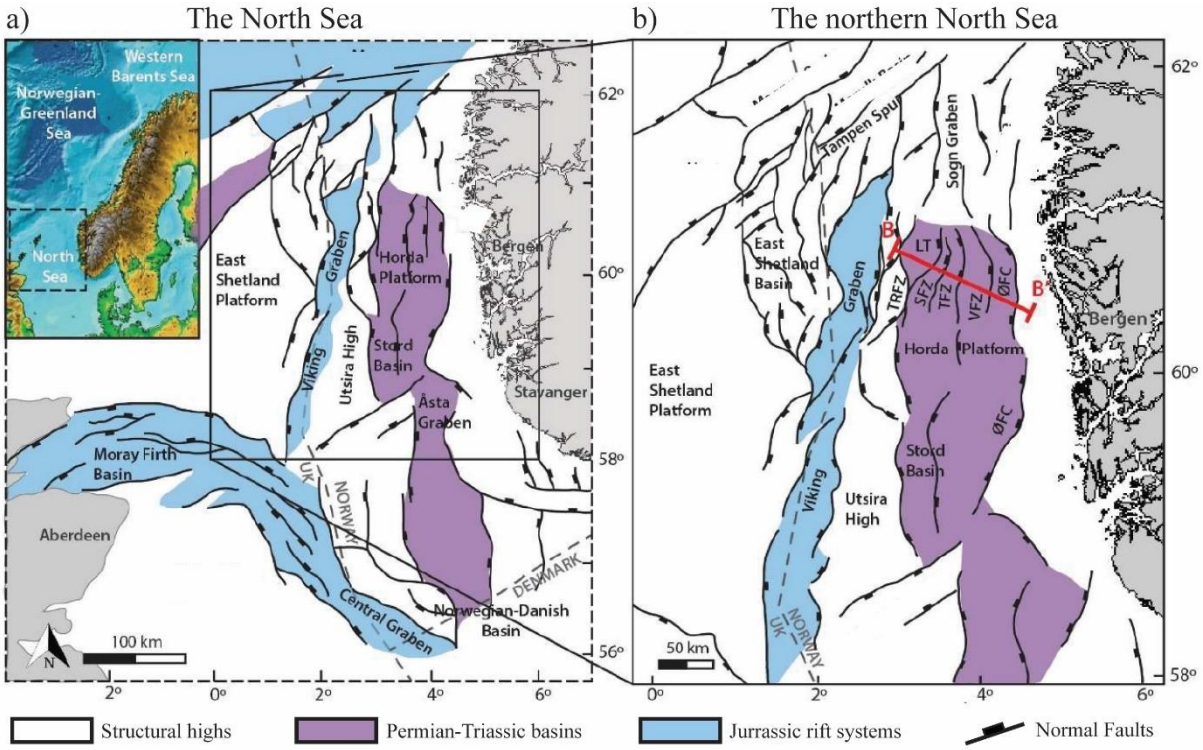

Figure 2.1: Structural element maps of the North Sea, showcasing main structural highs, basins and rift systems: a) the entire North Sea, b) insert of the northern North Sea. Modified from: Færseth (1996), Whipp et al. (2014), Faleide et al. (2015) and Holden (2021). Crossline B-B' is displayed in Figure 2.2. Abbreviations: ØFC = Øygarden Fault Complex, VFZ = Vette Fault Zone, TFZ = Tusse Fault Zone, SFZ = Svartalv Fault Zone, LT = Lomre Terrace, TRFZ = Troll Fault Zone.

2.1 Regional Structure

The Norwegian Continental Shelf (NCS) comprises the Western Barents Sea to the far north, the Norwegian-Greenland Sea to the northeast and the North Sea to the southwest. The North Sea is a 250 km wide intracratonic basin overlying the Caledonian continental crust (Faleide et al., 2015; Ziegler, 1992). Its predominant structural style is that of a rift basin, containing three major rift zones: the Moray Firth Basin, the Central Graben and the Viking Graben, arranged

in a trilete rift system that represents a failed arm of the Arctic-North Atlantic rift system (Figure 2.1, Davies et al., 2001; Whipp et al., 2014; Ziegler, 1992). In the northern North Sea, the main structure is the Viking Graben, with an eastern flank that hosts several significant structures: the Sogn Graben, Tampen Spur, Lomre Terrace East Shetland Basin and the easternmost Horda Platform (Figure 2.1b, Faleide et al., 2015). Located approximately 50 km west of Bergen, the Horda Platform forms a north-south elongated structurally high platform approximately 300 km long and 100 km wide. The platform consists of multiple tilted fault blocks: Troll West Oil Province, Troll West Gas Province, Troll East and Smeaheia (Whipp et al., 2014; Wu et al., 2021). These fault blocks formed during three main extensional rifting events. Firstly in the Devonian, secondly in the Permian-Triassic, and thirdly by reactivation in the Middle Jurassic to Early Cretaceous (Badley et al., 1988).

Mesozoic extension activated by the Pangean breakup, with rift axis situated underneath the Horda Platform, governed the structural development of the northern North Sea (Whipp et al., 2014). Crustal extension which lasted close to 175 M.yr. peaked during the Late Jurassic-Early Cretaceous stage, abated subsequentially and terminated completely during the Paleocene (Ziegler, 1992). The fault pattern within the Horda Platform is dominated by five major west-dipping, north-south striking, thick-skinned faults zones (Færseth, 1996). From east to west, they are the Øygarden Fault Complex (ØFC) and the Vette (VFZ), Tusse (TFZ), Svartalv and Troll (TRFZ) Fault Zones, displayed in Figures 2.1b and 2.2 (Duffy et al., 2015; NPD, 2021). The ØFC represent the boundary of the Mesozoic rift in the northern North Sea (Whipp et al., 2014). The master faults in these zones may reach over 100 km in length along strike, with a vertical extent cutting the entire brittle upper crust (12-14 km), exhibiting up to 3-5 km displacement (Whipp et al., 2014). Accompanying these master faults is a population of thin-skinned, syn- and antithetic faults (i.e., not basement-involved, with both S-W and N-E dip direction) of generally N-S to NW-SE striking faults. This population of faults are shorter, have lower throw ranges and are more closely spaced than the N-S striking master faults. Many of these subordinate faults only intersect the Upper Triassic to Cretaceous strata (Holden, 2021; Mulrooney et al., 2020; Whipp et al., 2014). Polygonal, non-tectonic faults have been described affecting the Upper Eocene-Middle Miocene strata, and a high density of pockmarks have been reported and mapped on the seafloor of the Horda Platform (Mulrooney et al., 2020 and references therein).

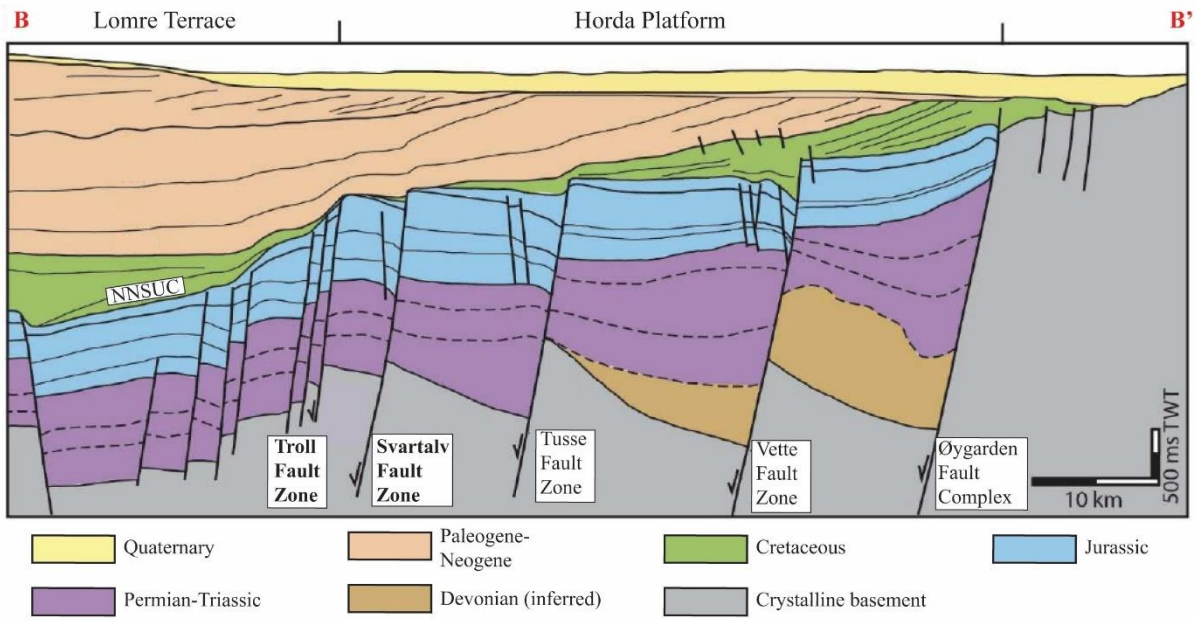

Figure 2.2: Crossline from figure 2.1b, showing the fault major fault pattern within the Horda Platform as well as the general sedimentary packages, divided by depositional time period. Modified from Whipp et al. (2014) and Holden (2021). Abbreviation: NNSUC = Northern North Sea Unconformity Complex.

Depth to the crystalline basement on the platform reaches 3-5 km (Bell et al., 2014), above which the deeper parts in the form of half grabens accommodate up to 3 km of pre-Jurassic syn-rift sediments. These deep basins are covered by ca. 1 km thick deposits prior to another ca. 0.5 km thick package of Late-Jurassic syn-rift strata (Whipp et al., 2014). A thin package of Quaternary sediments makes up the near-seafloor assemblage. These sedimentary packages contain several potential CO2 storage options currently being evaluated with estimated capabilities ranging from millions (Mt) to thousand million tonnes (Gt) of CO_2. The storage prospects are as follows: 1) the Aurora structure (120-293 Mt), south-east of the Troll Gas Field; 2) the Alpha structure (40-50 Mt), northern Smeaheia area; 3) Gamma structure (0.15-3 Gt), southern Smeaheia area and 4) the Troll Field (3-5 Gt) after the termination of gas production (Eigestad et al., 2009; Lothe et al., 2019; Nazarian et al., 2018; Sundal et al., 2015). Recently identified formations in shallow Early Mesozoic rocks provide potential fault-bounds storage prospects for CO_2 injection within the Aurora and Smeaheia area (Mulrooney et al., 2018; Osmond et al., 2022). The area includes parts of the Troll East and Troll West hydrocarbon fields as well as suitable CO2 storage prospects as addressed by Osmond et al. (2022).

2.2 Geological Evolution

This section will highlight the tectonic events and depositional history that led to the current state of the northern North Sea. When listed, formations and groups are ordered from oldest to youngest, as shown in the stratigraphic column in Figure 2.3. Special emphasis is made on the formations that are mapped and analysed in the study area, indicated as reservoir and cap rock intervals in Figure 2.3. As previously mentioned, the North Sea has been subjected to periods of stretching/thinning and subsidence during late Carboniferous, Permian-Early Triassic, and Late Jurassic times. Each rift phase was followed by a thermal cooling stage, characterized by regional subsidence in the basin areas (Faleide et al., 2015).

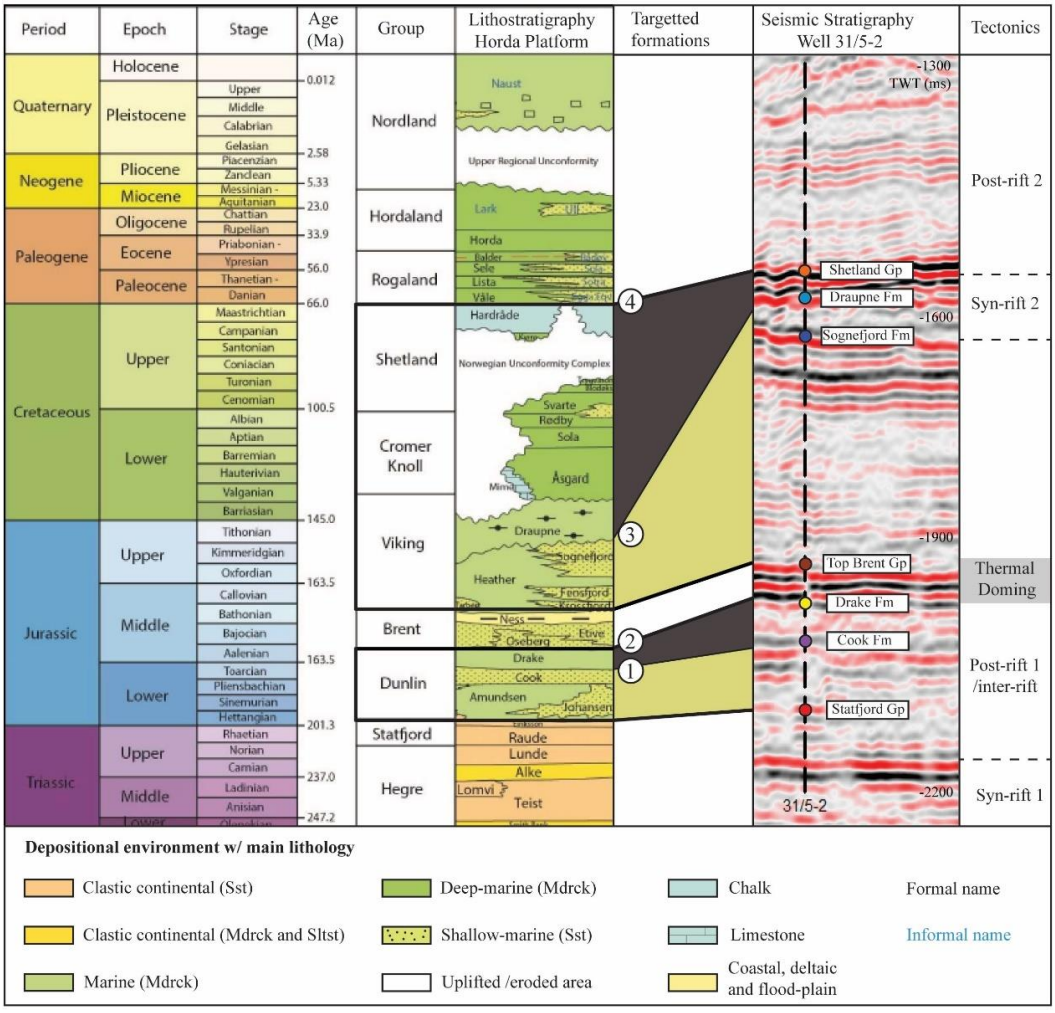

Figure 2.3: Stratigraphic chart of sedimentary deposits in the Horda Platform, from Triassic to Quaternary. 1: top of the Dunlin Group reservoir interval, 2: top of the Dunlin Group cap rock interval, 3: top of the Viking Group reservoir interval, 4: top of the tertiary sealing units of the Shetland Group, as described by Osmond et al. (2022). Modified from Halland et al. (2014), with tectonic events based on TFZ activity described by Whipp et al. (2014). Abbreviations: Sst = Sandstone, Mdrck = Mudrock, Sltst = Siltstone.

2.2.1 Silurian-Devonian Caledonian Orogeny and Collapse

The Caledonian orogeny ensued after the closing of the Iapetus Ocean by the oblique convergence of the palaeocontinents Baltica-Avalonia and Laurentia in Ordovician to Devonian times (Andersen & Jamtveit, 1990; Corfu et al., 2014; Fossen, 2010; Roberts, 2003). Subduction as the plates collided in the final (Scandian) phase of the orogeny is dated as approximately 430 Ma (Corfu et al., 2014; Gee et al., 2008; Kirkland et al., 2006). Extreme crustal thickening caused the collapse of the orogen at ca. 405-400 Ma and is seen as extensional tectonics manifested by major extensional detachments cutting the Caledonian nappe stack (Andersen & Jamtveit, 1990; Fossen & Dunlap, 1998; Gee et al., 2010; Norton, 1986). Extensional mylonite zones, best described in West Norway, underlie a series of Devonian basins, with basin formation spanning the Devonian and possibly the Early Carboniferous (Andersen & Jamtveit, 1990). The assemblage of Caledonian thrust sheets, extensional detachments and Devonian basins are found beneath the North Sea basins, creating a structural fabric that in many cases controlled the evolution of tilted fault blocks, including the Tusse, Svartalv and Vette fault zones. For instance, the VFZ was developed by reactivation of a deep, former shear zone (Mulrooney et al., 2018).

2.2.2 Permian to Triassic Rift Phase 1 and Post-rift Evolution

The architecture of the Horda Platform's rift blocks primarily developed during the Late Permian to Early Triassic in an E-W extensional phase, often termed Rift Phase 1 (Mulrooney et al., 2020; Würtzen et al., 2021; Ziegler, 1990, 1992). With tectonic forces inherited from the break-up of Pangea, the main structural elements were produced in the form of four westerly tilted fault blocks producing faults such as the Øygarden Fault Complex, Vette Fault Zone, Tusse Fault Zone and Svartalv Fault Zone, with throws reaching up to 4-5 km (Duffy et al., 2015; Færseth, 1996; Ziegler, 1982). The dominance of north-south striking faults in the area strongly supports an east-west extension, albeit local strike deviations might represent reactivation of basement lineaments and pre-existing shear zones running diagonally (NE-SW) across the basin (Bartholomew et al., 1993; Færseth, 1996; Mulrooney et al., 2018).

During the majority of the Triassic period, the northern North Sea accumulated continental deposition from the subsiding rift system. Continued extension caused movement and rotation on the larger faults, creating accommodation space in the hanging wall sides and erosion of the

uplifted footwalls, thus creating localized sediment source areas (Bartholomew et al., 1993; Færseth, 1996). It is estimated that up to 3 km of syn-rift sedimentary deposits is associated with Permo-Triassic rifting. Late Triassic times saw the deposition of the Hegre Group, consisting of intervals of interbedded sandstones, claystones and shales (Vollset, 1984).

Post-rift Phase 1 is concluded in Early to Middle Jurassic times with a 70 M.yr. period of relative tectonic quiescence. Middle Jurassic times saw a volcanic up-doming (central North Sea dome) centred in the U.K. sections of the northern North Sea, whose collapse procured thermal subsidence and rising sea levels, where a widespread transgression from north to south brought an end to continental deposition and heralded a transition into prevailing marine to shallow-marine environments (Bartholomew et al., 1993; Deegan, 1977; Mulrooney et al., 2018; Vollset, 1984; Ziegler, 1992). Through to the Middle Jurassic, these environments saw the deposition of the Statfjord, Dunlin and Brent groups (Figure 2.3). Statfjord Group represents a transition from semi-arid, alluvial planes to fluvial sandstones to marine-influenced sandstones, with a sharp, conformable upper boundary towards the Dunlin Group (Deegan, 1977; Halland et al., 2014; Vollset, 1984). The mudstones of the Dunlin Group mark the return of fully marine environments. The group is subdivided into five formations: Amundsen, Johansen, Burton, Cook and Drake (Figure 2.3). These formations represent a major marine transgressive sequence, where Amundsen, Burton and Drake formations are silt and marine mudstones, and Johansen and Cook formations are marine sandstones (Vollset, 1984). The entirety of the Dunlin Group has a thickness of up to 600 m in parts of the Horda Platform (Halland et al., 2014; Vollset, 1984).

The Cook Formation is described as having a white to greyish brown colour, with very fine to fine grains of sand, and is dominated by four sandstone tongues that interfinger with Drake Formation's mudstones (Marjanac & Steel, 1997). These tongues of sand are characterised by coarsening-upwards, bottom shoreface sand and siltstones, and an upper erosional surface of thin tidal flat and thick deltaic sands (Halland et al., 2014; Marjanac & Steel, 1997; Vollset, 1984). The gently basinward dipping formation is of Pliensbachian to Toarcian age and hosts important hydrocarbon reservoirs in the Statfjord, Gullfaks, Oseberg and Veslefrikk fields (Marjanac & Steel, 1997, and references therein; NPD, 2022). In the 31/5-7 (Eos) well, situated in the southern parts of the Aurora field, the formation is measured as 57 m thick (Thompson et al., 2022)

The Drake Formation is mostly composed of laminated silty shale, described as having grey, slightly sandy, calcareous claystone in the lower parts, whereas the upper parts are dark grey to black, micaceous shales (Halland et al., 2014; Marjanac & Steel, 1997; Vollset, 1984). Several layers exhibit exceptionally high natural radioactivity, interpreted as clean shales from either offshore or shelf deposits (Marjanac & Steel, 1997). The formation interfingers, as previously stated, with the underlying Cook Formation, but its youngest parts extend beyond the northern North Sea towards the basin margins (Marjanac & Steel, 1997). Drake Formation is of Toarcian to Bajocian age, with a thickness of 127 m in the previously mentioned 31/5-7 well (NPD, 2022; Thompson et al., 2022; Vollset, 1984). The upper boundary of the Drake Formation and the Dunlin Group is characterised by truncations by deep incisions, marking the transition to the sand-dominated sediments at the base of the deltaic Brent Group that overlies Dunlin conformably (Halland et al., 2014; Vollset, 1984).

Erosion of the central North Sea dome and the uplifted basin flanks supplied large volumes of sediments for the prograding Brent Group deltaic systems (Figure 14; Fjellanger et al., 1996). The group consists of five formations on the Horda Platform: Oseberg, Rannoch, Etive, Ness and Tarbert (Deegan, 1977; Fjellanger et al., 1996; Vollset, 1984). The earliest of which (Oseberg) represent a lateral basin infilling of sandstone, while the rest represent a large-scale regressive-transgressive wedge (Helland-Hansen et al., 1992). The Oseberg Formation was deposited on a shallow ramp-type basin as a large delta that prograded northwards while thinning towards the East Shetland Platform (Fjellanger et al., 1996; Helland-Hansen et al., 1992). Upper Brent, consisting of mixed sandstones, mudstones with coal layers, and clean sandstone on the very top is interpreted as a transition to a transgressive circumstance (Fjellanger et al., 1996). Tectonic rifting terminated the deposition of the Brent Group (Fjellanger et al., 1996; Helland-Hansen et al., 1992).

2.2.3 Jurassic to Cretaceous Rift Phase 2 and Post-rift Evolution

In the Late Jurassic to Early Cretaceous periods, the entire North Sea underwent a period of revived rifting, termed Rift Phase 2 (Bell et al., 2014; Duffy et al., 2015). The initiation and termination of Rift Phase 2 is interpreted to be diachronous through the entire northern North Sea, and likely linked with the collapse of the central North Sea dome and North Atlantic rifting (Bell et al., 2014; Færseth, 1996; Phillips et al., 2019). Crustal thinning, thermal subsidence and sediment loading ultimately led to the trilete rift system we acknowledge today as the

Viking Graben, Central Graben and Moray Firth Basin, including significant structural features like the Horda Platform (Figure 1; Davies et al., 2001; Faleide et al., 2015; Nottved et al., 2008; Whipp et al., 2014). Reactivation of north-south Permo-Triassic faults led to rapid propagation of throw up-section (Deng et al., 2017; Mulrooney et al., 2020). Simultaneously, in response to strain that pre-existing structures were not preferentially oriented for, a new population of 2-10 km long, NW-SE striking faults evolved. These faults show closer spacing, are thin-skinned only (i.e. not basement-involved/intersecting), only affect Upper Triassic strata and exhibit throws of less than 100 m (Mulrooney et al., 2020).

Accommodation created by rifting was filled with syn-rift sections of the fully marine Viking Group (Figure 2.3, Steel, 1993; Vollset, 1984). The Viking Groups' lower boundary is conformable and offers a prominent contrast between its fine-grained sediments and the sands of the Brent Group (Vollset, 1984). On the Horda Platform, the group consists of three shallow-marine clastic formations, stacked as follows: Krossfjord, Fensfjord, and Sognefjord, that interfinger basinward with the shelfal deposit of the Heather Formation and is overlain by the open marine mudstones of Draupne Formation (Steel, 1993; Vollset, 1984). The clastic sequences are of Norwegian mainland provenance and are mostly restricted to the Horda Platform (Steel, 1993; Vollset, 1984).

The Sognefjord Formation is described as consisting of grey-brown sandstones and sand of medium to coarse grains that are mostly well-sorted and sectionally unconsolidated (Steel, 1993; Vollset, 1984). The formation marks an upwards-coarsening regressive trend, forming a series of sand bodies in a stacking pattern (Steel, 1993). Argillaceous and carbonaceous beds with occasional calcite cement occur locally through the formation (Vollset, 1984). The deposition is restricted to the Late Jurassic, specifically Callovian to Kimmeridgian, in a coastal-shallow marine environment (Steel, 1993; Vollset, 1984). Sognefjord Formation is rarely thicker than 200 m and is the major reservoir interval in the Troll Field (Steel, 1993; Vollset, 1984). The uppermost units of the formation are commonly very thin, is where peak regression occurs and is conformably overlain by the base of the Draupne Formation (Steel, 1993).

The Draupne Formation is the uppermost member of the Viking Group and is the result of marine flooding in the North Sea basin after the deposition of the Sognefjord Formation (Mulrooney et al., 2020; Vollset, 1984). The Draupne Formation is an organic-rich shale and mudstone that was deposited in open-marine environments with restricted bottom circulations

(Rahman et al., 2020; Vollset, 1984). The Draupne Formation is the primary seal of the Viking Group on the Horda Platform (Rahman et al., 2020).

Above the Viking Group, a boundary called The Northern North Sea Unconformity Complex (NNSUC), or more informally the Base Cretaceous unconformity (BCU), divides sedimentary sequences that are deposited syn- and post-rift (Figure 2.2, Harris, 2019; Kyrkjebø et al., 2004). The unconformity marks a major tectonic and sedimentary break – signalling the post-Rift Phase 2. A period of thermal subsidence followed (Deegan, 1977; Nottvedt et al., 1995). The boundary is recognizable across the entire North Sea basin, and functions as an important marker horizon in the area (Kyrkjebø et al., 2004). Above the prominent boundary resides the Upper Cretaceous, deep marine clastic and carbonate stratigraphy of the Cromer Knoll and Shetland groups (Deegan, 1977; Lepercq & Gaulier, 1996). The Cromer Knoll Group is a calcareous mudstone whose upper contact with the Shetland Group is not always clear (Deegan, 1977).

The Shetland Group is described as a monotonous sequence of light to dark grey or reddish-brown calcareous mudstones and occasionally grading into grey shale (Deegan, 1977). It is similar to the Cromer Knoll, but contains significantly more calcareous material, manifesting as sequences of chalk and/or marl (Deegan, 1977; Halland et al., 2014). The mudstone has local bands of sandy limestone, fine-grained and sometimes dolomitic. The upper unit of the group is a very fine-grained, dense, white, chalky limestone (Deegan, 1977). The Shetland Group is aged from Cenomanian to Danian in the North Sea, but the siliciclastic phase is limited to the Late Cretaceous (Figure 2.3, Deegan, 1977; NPD, 2022). The group ranges between 1000-2000 m thickness in the North Sea, showing substantial thinning towards and on the platform areas (NPD, 2022). On the Horda Platform, it is 80 m thick in well 31/5-7 (NPD, 2022). The upper Cretaceous Cromer Knoll and Shetland groups act as a secondary and tertiary seal in areas encompassing the Troll oil and gas fields, especially where the Draupne Formation has eroded and is missing from the stratigraphy (Bolle, 1992; Osmond, 2021; Spencer & Larsen, 1990).

2.2.4 Paleogene to Recent evolution

By the end of the Cretaceous, most of the post-Rift Phase 2 tectonic activity and thermal subsidence had ceased, and the northern North Sea basin had evolved into an extended region of deposition characterized by widening and smoothing (Faleide et al., 2002; Gabrielsen et al.,

2001). Throughout the Cenozoic, two significant episodes of uplift occurred. In the early Paleocene uplift was driven by rifting, magmatism and the break-up of the Atlantic, while in the late Neogene, isostatic response to glacial erosion was responsible, causing considerable tilting of the entire Tertiary package (Faleide et al., 2002). Cenozoic sedimentary structure and hiatuses are consequently influenced by an uplift of the surrounding region, with depositions generally overstepping the basin margins and development of a prograding coastal wedge along the present-day Norwegian coast (Faleide et al., 2002; Lepercq & Gaulier, 1996). Continued uplift shaped an enlarged Viking Graben depocenter containing up to ca. 2500 m of sediments, shallowing the basin (Faleide et al., 2002; Gabrielsen et al., 2001). On the Horda Platform, these sediments constitute the Rogaland Group of Paleocene-Eocene age, the Hordaland Group of late Eocene to Miocene, and the Nordland Group of late Miocene to Holocene age. Subsidence and sea level lowering through the Paleogene resulted in sedimentary successions of the Rogaland Group, characterised by sandstones grading into shales, interrupted at the end of Palaeocene by ash-falls deposits of the Balder Formation (Isaksen & Tonstad, 1989). The Palaeocene-Eocene transition coincides with extreme global warming when the North Sea became a narrow stagnant water body (Anell et al., 2012). Further subsidence into Miocene caused a major transgression, covering the ash beds with the marine muds and small deltaic complexes of the Hordaland Group (Isaksen & Tonstad, 1989; Lepercq & Gaulier, 1996). From the late Miocene, the Nordland Group succession was dominated by fine-grained marine clastics, grading into clays, moraines and outwash sands in the Quaternary, deposited in front of oscillating ice sheets (Isaksen & Tonstad, 1989). These glacial deposits are in turn overlain by sheets of unconsolidated sands and gravel, produced by the reworking of present-day currents, the extent of which is marked by a NW-SE topographic depression (the Norwegian Trench), that is still the main feature of present-day bathymetry (Isaksen & Tonstad, 1989; Lepercq & Gaulier, 1996).

3 Theory of Fault Reactivation

This chapter will present the theory related to this study. Classic concepts such as fault characteristics and morphology, failure mode, fault rocks, fault stability and reactivation potential will be succinctly explained. Additionally, the theory behind the analytical methods for assessing reactivation potential will be presented. A list of the important parameters and definitions used in this study is provided in Appendix A.

Although faults are bodies of rock, they are for the sake of simplicity modelled as nonvolumetric lines or surfaces, especially in seismic sections. This method serves to separate the hanging wall from the footwall and highlight the intersection of stratigraphic interfaces with fault cut-off lines. In this study, parameters such as fault strike, dip, displacement, syn- and antithetic will be used to describe fault morphology and characteristics.

3.1 Principal Stresses and Parameters

The effective principal stresses ($\sigma'_1, \sigma'_2, \sigma'_3$), acting on a plane can be expressed as Equation 3.1, where $\sigma_1 > \sigma_2 > \sigma_3$ are the principal compressive stresses acting on a plane at an angle θ (a proxy for dip angle) to σ_1, and P is the present pore fluid pressure (Sibson, 1985).

$$\sigma'_1 = (\sigma_1 - P) \;>\; \sigma'_2 = (\sigma_2 - P) \;>\; \sigma'_3 = (\sigma_3 - P) \qquad \text{(Eq. 3.1)}$$

In 1905, Ernest Anderson described the three Andersonian fault classes based on the orientation of the stresses and the relationship between the footwall and the hanging wall (Anderson, 1905):

a) Reverse faults, where the hanging wall is upthrown relative to the footwall, originate when the maximum principal stress (σ_1) is horizontal and the least (σ_3) vertical.

b) Normal faults, where the hanging wall is downthrown relative to the footwall, originate when σ_1 is vertical and σ_3 horizontal.

c) Strike-slip faults, where the relative movement is lateral in the horizontal plane, originate when σ_1 and σ_3 are both horizontal.

In a normal faulting regime, the maximal principal stress (σ_1) is vertical, produced by the weight of the overburden and affecting the faults at a 90° angle from above, and can in this case be called σ_v. The intermediate (σ_2) and the minimal (σ_3), principal stresses act horizontally and can be called σ_H and $\sigma_{h,}$ respectively. The relationship of the principal stresses can thus be written as: $\sigma_V > \sigma_H > \sigma_h$. The magnitude of these stresses in the study area will be synthesized from literature in subchapter 4.5. The difference between the maximum and minimum principal stresses (σ_1-σ_3), is the differential stress (σ_d). Stresses impacting a surface from a perpendicular angle is called the normal stress (σ_n), while stresses impacting from a parallel angle is called shear stress (τ). Pore pressure (P) is the pressure of a fluid in pore spaces in a rock. Pore pressure reduces the effective stress acting on a plane (see Equation 3.1), increases with depth and is usually described as hydrostatic or depleted. This study considers the principal in-situ stresses, meaning the original stress status of an area before perturbations, as well as fault rock properties such as the coefficient of friction (μ), angle of internal friction (φ), cohesion (C) and tensile strength (T).

The coefficient of friction (μ) can generally be considered to be in the ranges of 0.6 - 0.85 for intact crustal rocks (Byerlee, 1978). However, more recent studies have shown that the value for μ can vary significantly when considering fault rocks and fault gouges, or fault zones enriched with clay minerals such as smectite (Ferrill et al., 2017). The coefficient of friction of fault gouges, illite or other phyllosilicates might range between 0.2-0.4 and indeed fall below 0.2 for smectite-bearing rocks, while sandstones and some fault gouges remain at $\mu \approx 0.6$ (Ferrill et al., 2017; Saffer & Marone, 2003). The angle of internal friction (φ) is the angle between σ_1 and the plane of the failure that occurs in response to shear stress (τ), and its relationship with the coefficient of friction (μ) is tan $\varphi = \mu$.

Cohesion (C) is the inherent shear strength of a rock, as opposed to the inherent tensile strength (T). The more lithified a rock is, the more cohesion. In classical geomechanical fault seal analyses, it is common to assume that fault rocks are cohesionless since they are in essence a plane poised for slip (e.g. Zoback, 2010). However, this assumption fails to consider that post-deformational cementation, compaction and cataclasis processes and increased post-kinematic burial depth might cause fault rocks to regain or exhibit enhanced cohesive strength and increased coefficient of internal friction, often referred to as fault healing (e.g. Underhill & Woodcock, 1987; Van den Ende & Niemeijer, 2019; Weiss et al., 2016).

3.2 Principal Modes of Failure

Nucleation and evolution of fault growth are highly dependent on the mechanical stratigraphy of the rock (Ferrill & Morris, 2008; Ferrill et al., 2017). Mechanical stratigraphy is defined by Ferrill et. al. (2017) and encompasses the rock's mechanical properties, the frictional properties of layer boundaries and layer thickness and is governed by the rock's mineralogy and texture (Ferrill et al., 2017). Mechanical stratigraphy often causes normal faults in stratified rocks to exhibit variations in dip angle, caused by differential compaction of layers, active fault deformation style (tensile or shear), linkage of originally vertical fault segments or simply because angles during fault initiation were controlled by rock properties or effective stresses at the time of failure, that has since changes (Ferrill et al., 2017).

Since the strength of a fractured rock is much less than that of an intact, massive formation, it is recognized as highly probable that deformation is accommodated by reactivation of pre-existing features and discontinuities, rather than the generation of new faults, even if unfavourably oriented (McKenzie, 1972; Sibson, 1985; Sykes, 1978). Reactivation of faults depends on the effective principal stresses, the orientation of the pre-existing weaknesses to the present-day stress field, the presence of pore fluids and most importantly the geomechanical properties of the fault, such as cohesion and angle of internal friction. Research from outcrops demonstrates that mechanical stratigraphy also influences the faults mode of failure, fault dip and displacement (Childs et al., 1996; Peacock & Sanderson, 1992), fault zone width and the amount of stress that a rock can support, and where strain is localized (e.g. Smart et al., 2009). The effects of mechanical stratigraphy on the predominant failure mode of the fault are of severe importance while considering the probability of fault reactivation, and the implications following such an event. Shear fractures have historically been considered the prime failure mode in normal faulting. There is, however, substantial evidence that faults might develop or reactivate by failure of all modes, governed entirely by the rock's mechanical stratigraphy, the in-situ stress conditions and the deformation history (Ferrill et al., 2017).

The failure modes principally considered in geology are visually presented by a Mohr diagram in Figure 3.1 and listed from least to greatest normal stress:

I. **Tensile failure**, also known as opening-mode or extension fracture, involves volume gain and form perpendicular to the minimum principal stress, σ_3, and at an angle of 0° to σ_1. Tensile failure is characterized by a sense of displacement in the form of

opening and volume gain normal to the fault plane, with zero displacement parallel to the plane (Fossen, 2016). Tensile failure occurs with increased pore pressure, P, at relatively low differential stresses and often where existing faults become severely misoriented for shear failure and often when the faults have regained some cohesion (Mildren et al., 2005). Tensile failures create Mode I fractures.

II. **Hybrid failure**, also known as transition-tensile fractures, is defined as the transition between tensile and shear failure. It involves both volume gain and shear displacement. In nature, it occurs commonly as a product of induced hydraulic fracturing (Smart et al., 2014). Hybrid failures create a combination of Mode I and II fractures.

III. **Shear failures** occur at an acute angle to σ_1, parallel to σ_2 (the plane of the fracture), and at an obtuse angle to σ_3. Shear failure is considered volume neutral and is the primary mechanism associated with fault formation, often recognized by slip lineations in outcrop studies (Ferrill et al., 2020). Shear fracturing occurs at relatively high differential stresses (σ_1-σ_3) when the diameter of the Mohr circle is large compared to the tensile or cohesive strengths of the rock (Mildren et al., 2005). If the cohesive strength, C, of a reactive fault zone is zero, shear failure is the only possible mode of failure, regardless of the differential stress (Mildren et al., 2005). Shear failures create Mode II and III fractures.

IV. **Compactive shear failures** are hybrid failures expected at angles between that of shear failure and compactive failures, with respect to σ_1 (Ferrill et al., 2017; Ferrill et al., 2020). As a result, compactive shear failure involves both volume loss and shear (volume neutral) components and occurs when σ_3 is compressive. Compressive shear failures create a combination of Mode II, III and IV fractures

V. **Compactive failures** form perpendicular to σ_1 and remain neutral in the σ_2 and σ_3 directions, with σ_3 being compressive (Ferrill et al., 2017; Ferrill et al., 2020). The compactive nature of the fracture involves volume loss, with displacement perpendicular to the failure surface. Compactive failures create Mode IV fractures.

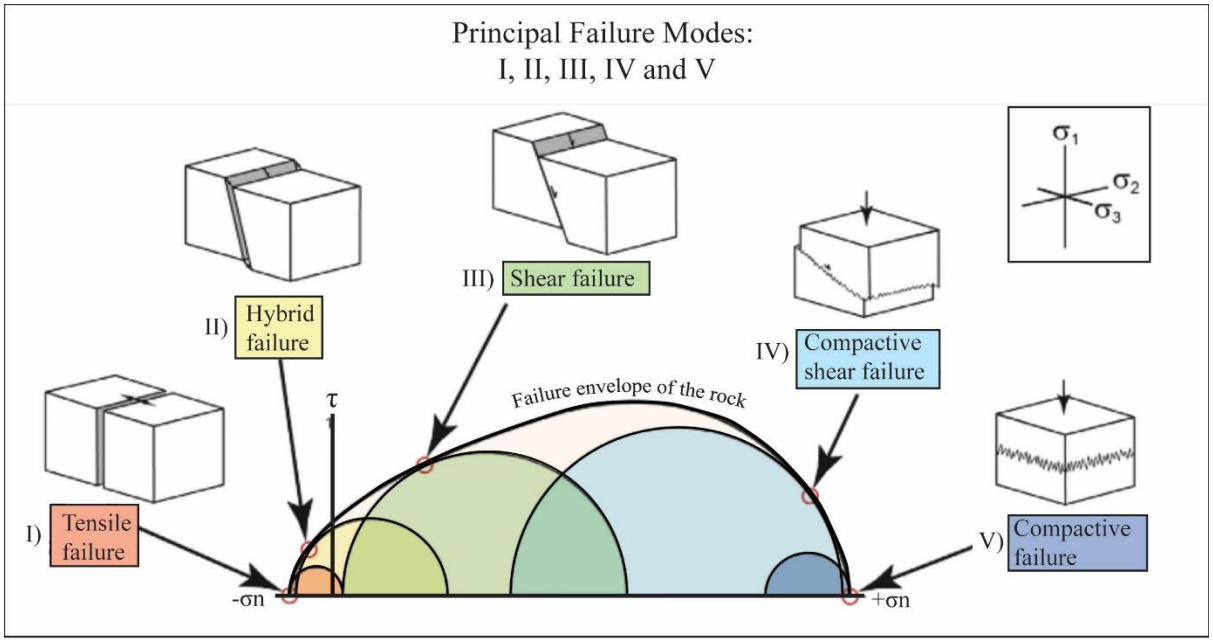

Figure 3.1: Failure modes principally considered in geology and their relationship with the Mohr circle, stress conditions, both tensile, compressive as well as shearing. The model in the top right corner displays the orientations of the stress tensors. τ denotes the shear strength of the rock, while $-\sigma_n$ and $+\sigma_n$ denote decreasing and increasing magnitude of effective normal stress, respectively. Modified from Ferrill et al. (2017).

3.3 Fault Rock Properties and Classification

With the initiation of fault activity, the original host rock within the damage zone is altered, turning it into brittle fault rocks or fault gouges (Fossen, 2016). While it is impossible to adequately image or deduce fault rock attributes through seismic methods, it is possible to infer the composition of the fault rocks from the host rocks' lithology, burial depth and core samples (e.g. Dewhurst & Jones, 2002; Mulrooney et al., 2022; Sperrevik et al., 2002). The characteristics of the resultant fault rocks are determined by cohesive strength, processes of brittle deformation, fault rock constituents, level of cementation (temperature) and fluid pressure (Fossen, 2016; Sibson, 1977). Typical incohesive fault rocks found in the northern North Sea include fault breccias, clay smears, gouges and phyllosilicate framework fault-rocks (PFFRs), while cohesive fault rocks include pseudotachylytes, disaggregation zones and cataclasites (Figure 3.2, Fisher & Knipe, 1998).

Laboratory studies have shown that the fluid content and mineralogy of fault rocks and gouges dominate the control of the geomechanical properties of the fault, especially considering fault stability, frictional, tensile and cohesive strengths (e.g. Ikari et al., 2011; Morrow et al., 2000; Shimamoto & Logan, 1981). The aforementioned studies agree that fault rocks or gouges that

are rich in phyllosilicates are significantly weaker than those rich in quartzofeldspathic minerals. Phyllosilicates that particularly contribute to the decrease in frictional strengths include illite, smectite, chlorite and mixed compositions of the same (e.g. Haines et al., 2014; Tembe et al., 2009). Since exact mineralogy and more importantly clay content is very hard to define, except through core samples that do not represent an entire sequence of sediments, a proxy for clay content is often used: Shale Gouge Ratio (SGR) (see: Yielding, 2009; Yielding et al., 1997). SGR sums up the thickness of shale beds of the stratigraphy that has passed a point of a fault and then calculates the percentage of clay or shale in the displaced interval by dividing by the fault throw (Yielding et al., 1997).

In the classification scheme presented in Figure 3.2 by Fisher & Knipe (1998), fault rocks can be classified within three main series: 1) clay-smears, 2) phyllosilicate frameworks (PFFRs) or 3) quartz-rich lithologies, meaning aggregation bands or cataclasites (Figure 3.2, Fisher & Knipe, 1998; Pei et al., 2015; Yielding et al., 1997).

Fisher & Knipe's (1998) method of fault rock classification was developed for fault rocks encountered in the North Sea, especially for clean sandstones/silts, impure sandstones/silts, claystones and shales. It predicts the fault rocks by deriving their host rock's state of lithification, fragmentation and percentage of clay minerals or SGR. In subchapter 4.5, Fisher & Knipe's (1998) fault rock classification will be used to define fault rock lithologies in the study area as either clay smears, PFFRs, disaggregation zones or cataclasis, or cemented versions of these.

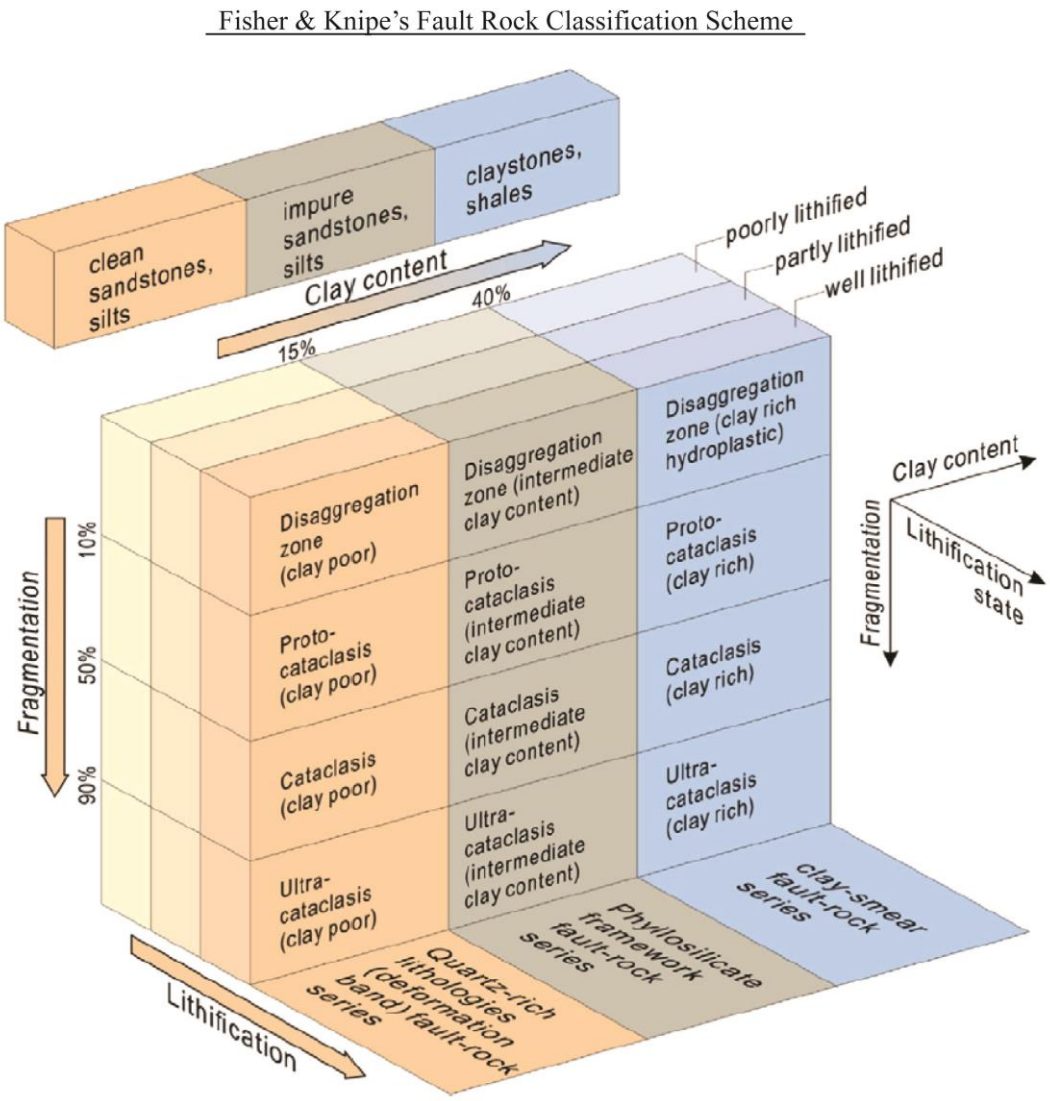

Figure 3.2: Fisher & Knipe's (1998) classification scheme for types of fault rocks commonly developed in the North Sea and their relationship to the composition of the host rock and the degree of fragmentation and post-deformation lithification the host rock has experienced. Modified from Pei et al. (2015).

3.4 Fault Reactivation Potential

Reactivation of fault segments poses a significant threat to all subsurface exploitation endeavours. Reactivation might be caused by three factors: i) regional increase in the compressional stress, ii) localized increase of pore pressure, or iii) present-day stress fields optimally aligned with the orientation of the fault segment (Wiprut & Zoback, 2000). In 1973, Charles Augustin de Coulomb found a criterion that could predict the state of stress where rocks under compression are found to be critically stressed. For a pre-existing fault or fracture

plane to reactivate, the shear stress (τ) applied to the plane must exceed the cohesive strength (C) of the rock, the frictional resistance to sliding represented by the coefficient of internal friction (μ) and the resolved effective normal stress (σ_n) acting on the plane (Coulomb, 1773). The relationship between these factors is expressed by the Mohr-Coulomb failure criterion (Equation 3.2) and can be readily displayed in the famous Mohr diagram, especially concerning the stability of a single fault segment (Figure 3.4).

$$\tau = C + \mu\,\sigma_n \qquad \text{(Eq. 3.2)}$$

The Mohr diagram is an essential tool to evaluate the stress state in a fault or rock body by representing the shear strength of a rock as a line called the failure envelope, and the in-situ stresses as Mohr circles (e.g. Fossen, 2016). In a Mohr diagram, the minimum stress required for reactivation is visualized as stress states where the Mohr circle touches the frictional failure envelope (Figure 3.1). In other words: any fault is considered critically stressed if the resolved shear stress exceeds the shear strength of the material.

Sibson (1985), using a commonly accepted value of μ=0.75 for rocks and with a proxy for fault dip θ, presented how a minimum stress ratio for reactivation to occur is achieved at a dip angle of θ= 26.5°, and how angles at 2θ = 53° require σ_3 to act in a tensile manner (Byerlee's Law; Byerlee, 1978; Sibson, 1985). However, the coefficient of friction for rocks and especially fault rocks can vary greatly from 0.75, thus allowing faults to reactivate at significantly higher dip angles than 26.5° and 53°.

Failure envelopes for fault rocks can be determined through tri-axial laboratory testing, wherein parameters such as cohesion and angle and coefficient of internal friction can be resolved (e.g. Dewhurst & Hennig, 2003; Dewhurst & Jones, 2002, 2003; Meng et al., 2006). Data from the studies presented in this sub-chapter will be synthesized in chapter 4.

3.5 Assessing Reactivation Potential

Several feasible analytical methods have been recently designed to efficiently assess and intuitively present a faults risk of reactivation. This study utilizes four different but complimentary methods that aim to determine the likely mode of failure (e.g. shear vs dilation), and the critical perturbation pressure required for the faults to reactivate. Since the lithologies of fault rocks might change along the fault trace, especially affecting parameters such as

cohesion, and thus altering the faults failure envelope, a sensitivity analysis testing different values of these parameters is often recommended (e.g. Mildren et al., 2005) The methods utilized in this study are presented in Table 3.2 and the following subchapters.

Table 3.2: The four analytical methods of calculating reactivation potential used in this study, as well as their symbols and functions. Abbreviations: τ – shear strength, σ_n – normal stress, σ_1 – maximum stress, σ_3 – minimum stress, P – pore pressure, C – Cohesion, CPP – Critical Perturbation Pressure.

Symbol	Description	Function	Comment
T_s	Slip tendency	$T_s = \tau / \sigma_n$	Ratio from 0 to 1.
T_d	Dilation tendency	$T_d = (\sigma_1 - \sigma_n)/(\sigma_1 - \sigma_3)$	Ratio from 0 to 1.
S_s	Slip stability	$S_s = \sigma_n - P$	Used to calculate CPP with friction but without cohesion
F_s	Fracture stability/ FAST	Tensile failure = $\sigma_3 + C/2$ Shear/tensile = $\sigma_n + (C^2 - \tau^2)/2C$ Shear failure = $\sigma_n + (C - \tau)/ P$	Used to calculate CCP with friction and cohesion

3.5.1 Slip and Dilation Tendency

Slip tendency (T_s) was defined by Morris et al. in 1996 as "the tendency of a surface to undergo slip in a given stress field", or in other words the ratio of resolved shear stresses (τ) and normal stresses (σ_n) acting on a surface. The analysis is dependent on the ratio of shear to normal stress acting on that surface and the surface's orientation within the stress field (Morris et al., 1996). Slip tendency is given by the equation presented in Table 3.1 and is a ratio ranging between 0 and 1, where slip is likely to occur when the resolved shear stress exceeds the frictional resistance to sliding or the coefficient of friction (μ). Faults that exhibit slip tendency values that are equal to or exceed the coefficient of friction ($T_s \geq \mu$) of the inherent fault rock are considered to be critically stressed or about to reactivate by slip (e.g. Zoback, 2010).

Dilation tendency (T_d) was defined by Ferrill et al. in 1999 as the equation in Table 3.2. The addition of this tendency was necessary because the magnitude and direction of the resolved normal stress (σ_n) acting upon a fracture or fault, as a function of lithostatic or tectonic stresses and fluid pressure, can cause failure by dilation (e.g. Ferrill et al., 2017; Mulrooney et al., 2022). Dilation tendency is also a ratio ranging between 0 and 1, with a higher value meaning more likelihood of reactivation by dilation/tensile failure (Figure 3.3b).

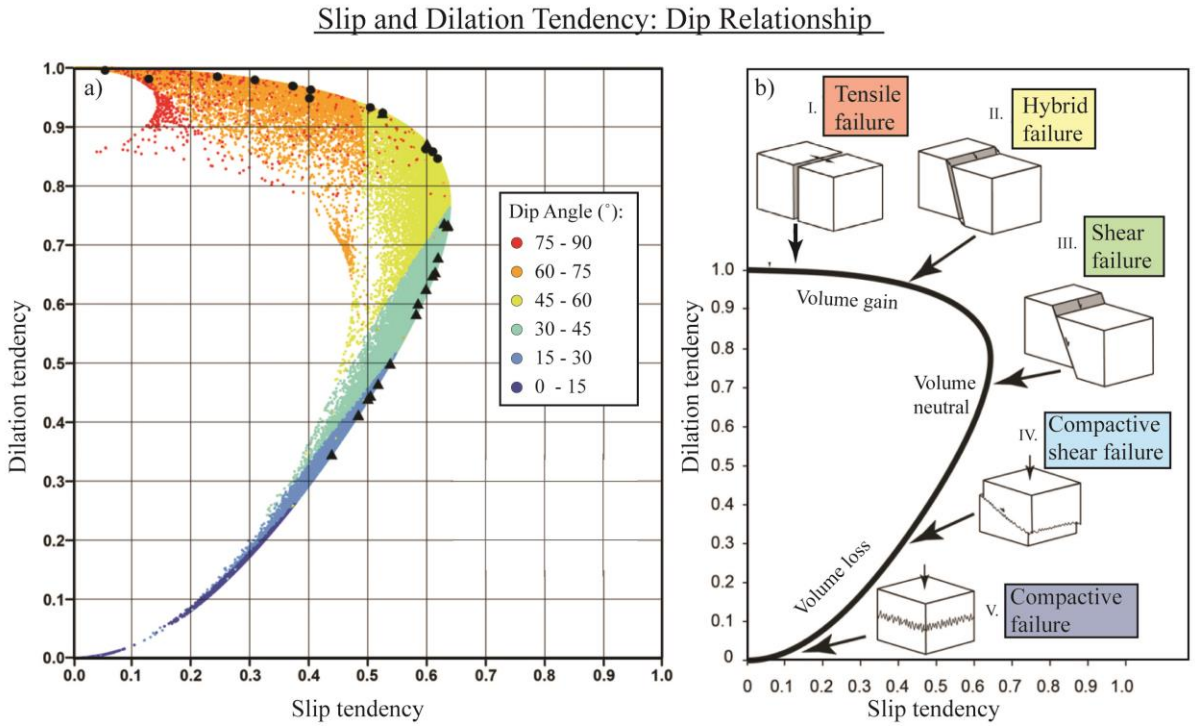

Figure 3.3: Slip tendency (T_s) and Dilation tendency (T_d) and their relationship with fault dip angle. a) T_s plotted vs. T_d, their relationship is coloured draped by dip angle values, b) T_s plotted vs. T_d and their relationship with the five principal failure modes. Modified from Ferrill et al. (2020). Note that shear failure occurs at high values of both slip and dilation tendency. Roman numerals I-V denotes modes of failure, see Figure 3.1.

Any value of dilation tendency that exceeds 0.80 passes the criteria for failure by dilation (Ferrill et al., 2020). Results by Ferril et al. (2020) show that vertical faults in a normal faulting regime that strike parallel to the maximum horizontal stress have the highest dilation tendencies, whereas faults with strong normal stresses acting upon them are more expected to be closed, in comparison with faults with weak normal stresses.

Considering slip and dilation tendency in terms of failure mode and reactivation mode, Ferril et al. (2020) demonstrate how the transitions from tensile to hybrid, shear, compactive shear and compactive failure (Mode I-V) correspond with the progression in dilation tendencies of 1 to 0 (Figure 3.3b). Conversely, high slip tendencies correspond to shear failure, while hybrids and tensile failure correspond with a reduction in slip tendency down to zero, owing to no resolved shear stress on a surface with purely tensile/compactive stresses acting on it (Figure 3.3b). In this instance, the dilation tendency is 1. The interconnected and individual relationship between slip and dilation tendency and fault dip is presented in Figure 3.3a. Note that if dilation tendency T_d=1 and slip tendency T_s=0, then the mode of failure is purely tensile (Mode I),

whereas the mode of failure is purely compressive (Mode V) when dilation tendency and slip tendency are $T_d=T_s=0$ (Figure 3.3, Figure 3.4).

An advantage to slip and dilation tendency is that it is independent of the rock's geomechanical properties, by only relying on the orientation of impact from the local stress field (Ferrill et al., 2020). Even so, whether or not a fault will actually slip or dilate highly depends on the fault's cohesive and tensile strength and the angle of internal friction exhibited in the fault rocks.

3.5.2 Slip and Fracture Stability

The previously described Mohr-Coulomb failure criterion can be used with Mohr diagrams to express the Critical perturbation pressure (CPP). The CPP predict the extra pore pressure (ΔP in MPa) required to put a fault or fracture into shear failure, visualized as the horizontal distance between a given point in the Mohr circle and the failure envelope of the fault (Figure 3.4). Consequently, if a small amount of extra pore pressure (low CPP) is needed for a fault's failure to intersect the Mohr circle, then the supposed risk of failure is very high. Note that within this study the term "fault tolerance" is used to describe a fault's ability to resist pressure increases, meaning a fault with high tolerance exhibits high values of CPP.

The critical perturbation pressure can be used for faults that are considered cohesionless, in this case, the method is called slip stability (S_s), or for faults with cohesion, now called fracture stability (F_s) or FAST (Mildren et al., 2005). Because of its ability to consider both tensile and shear failure as well as the cohesive strength of the fault rock, fracture stability (F_s) is one of the most effective tools to assess the response of a fault when subjected to an increase of pressure due to CO^2-injection. It is important to note that the fracture stability method always assumes that reactivation occurs in the in-situ stress field, as determined by wellbore data, and that the method can only be applied to interpreted fault surfaces, not to subseismic or otherwise unmapped faults.

Their respective equations are presented in Table 3.2, note that slip stability only considers shear failure, whereas fracture stability can consider tensile and shear and both at the same time (Mildren et al., 2005; e.g. Sibson, 2003). A typical result from the fracture stability analysis can be generated by the Petex Move software and is presented in Figure 3.4b. In this case, data points of dip values for the fault in question are displayed as black dots, effectively showing if the overall fault orientation lies posed to reactivate, this can also readily be done for strike values. In the case of Figure 3.4b, the majority of dip data points, and thus the overall fault surface exhibit low CPP and as such a further increase of pore pressure due to CO_2 injection might put the fault into a critically stressed state. Critical perturbation pressure, slip stability and fracture stability are all measured in MPa where the lower the pressure the higher the risk of failure by reactivation (Figure 3.4a).

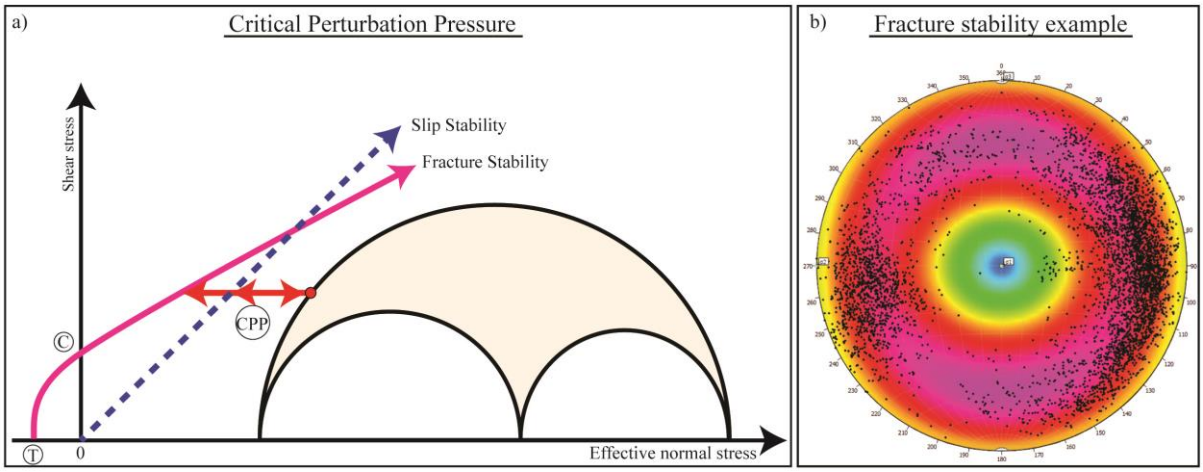

Figure 3.4: Critical perturbation pressure (CPP) and: a) the difference between slip stability (S_s) and fracture stability (F_s) highlighted by their intersection of the Mohr circle, b) example of what the results from a fracture stability (F_s) analysis might look like. Black dots represent dip angle data points, purple-red-coloured areas represent areas of low, and orange-green-blue-coloured areas represent areas of high CPP. Abbreviations: C = Cohesive strength, T = Tensile strength, CPP = critical perturbation pressure (ΔP), implying the amount of extra pressure needed to put a fault into a critically stressed state.

4 Datasets of the Study

This section presents the data utilized in this study. A detailed description of the 3D seismic data, well data and velocity model will be given as well as the limitations of seismic data. Additionally, data concerning the in-situ stress conditions in the study area will be presented, and the considered intervals will be assigned lithological properties. A summary of concepts and terms applied in the thesis, and their definitions, is provided in Appendix A.

4.1 3D Seismic Data

The essence of seismic reflection surveying is to measure the time it takes for a seismic wave to travel from a source and propagate into the subsurface, where it is then reflected back up. The time measured is the two-way-time (TWT) in milliseconds (ms). The strength of the reflected signal is governed by the contrast in acoustic impedance (AI), the compressional wave velocity (v) and the bulk density of each rock layer (Brown, 2011; Mondol, 2010; Reynolds, 2011). Since velocity and density vary as a function of petrophysical properties (mineralogy, porosity and pore fluids), and depth of the interface, acoustic impedance can be correlated to variations in lithologies of the subsurface (Bjørlykke, 2010; Brown, 2011).

In this study, data from the GN10M1 3D survey was utilized for all interpretations and model creations. The GN10M1 survey was made by Gassnova in 2010 as a pre-stack merge of three other surveys; NPD-TW-08-4D-TROLLCO2, GN1001 and NH0301 (Table 4.1, Gassnova, 2012). The survey is in the ED50-UTM31 coordinate reference system, covering an area of 1370 km^2 with a penetration depth of 4000 ms. It covers areas within the Norwegian quadrants 31/1-31/9, encompassing north-eastern parts of Troll East and the entirety of Troll West, as well as the northern parts of the Aurora Licence (EL001), see Figure 1.2. The study area covers approximately 730 km^2 of the southern parts of the survey (Figure 1.2). GN10M1 has E-W trending inlines, N-S trending crosslines and is considered as having good to very good imaging quality (Gassnova, 2012). The survey has an inline and crossline spacing of 25 m and 12.5 m, respectively, and a depth penetration into Lower Jurassic sediments and the crystalline basement. In the GN10M1, both the seabed and a well-documented flat spot situated in the Troll West Field can be examined for the determination of polarity and phase (Bolle, 1992). In the survey, they are both displayed as a downward increase in acoustic impedance and

represented as a single symmetrical wavelet with a high amplitude. Thus the GN10M1 is interpreted as having zero-phase quality and follows the convention of normal polarity.

4.2 Wellbore Data

For this study, the NPD Diskos archive was perused for wells within the Norwegian quadrant 31. Targeting Troll West and East fields, 78 wells were gathered and made available for assessment. Of these, 8 wells were used for further study, as follows: 31/5-2, 31/5-3, 31/5-7, 31/8-1, 31/3-1, 31/2-5, 31/6-1, 31/6-8 (Table 4.2). These wells were utilized to correlate well data with seismic data and are presented in Table 4.2, with the intent of highlighting their intersection with the formations mapped and analysed in this study. Of these, the first four are to be found within the study area, where only 31/5-2 and 31/5-7 intersect all four formations. However, the four wells outside of the study area also intersect all four formations and have been extensively utilized, given their proximity to the study area.

The wells in the study area include the newly drilled and now famous 31/5-7 (EOS) well. Drilled to test the Northern Lights storage prospect, the well is the first purely CCS well on the Norwegian Continental Shelf. The well targeted the Dunlin Group and was made to investigate the sealing potential of the Drake Formation, the reservoir quality and scale of the Cook and Johansen formations and to collect in-situ stress measurements (NPD, 2022; Thompson et al., 2022). The well confirmed both storage resources and integrity within the Dunlin Group and proved the area of the Aurora License as that of a relaxed/normal-stress tectonic character (Thompson et al., 2022).

Table 4.1: The four seismic surveys merged into the GN10M1 survey, with their respective production year, spatial extent, quality and orientation. Company and survey information is sourced from NPD Diskos archive.

3D Cube	Company	Year	Area (km^2)	Quality	Inline dir.
NH0301	Norsk Hydro Produksjon AS	2003	718	Good/very good	NE-SW
NPD-TW-08-4D-TROLLCO2	StatoilHydro AS	2008	293	Good	E-W
GN1001	Gassnova SF	2010	503	Excellent	E-W
GN10M1	Gassnova SF	2010	1370	Good/very good	E-W

Table 4.2: Data for the eight wells utilized in this study, showing their production date, depth and at what depth (in meters) they intersected with the formations mapped in this study. Data was collected from the NPD fact pages (NPD, 2022).

Well	Finished	Within study area?	Depth (m)	Intersect: Shetland	Intersect: Sognefjord	Intersect: Drake	Intersect: Cook
31/5-2	1983	Yes	2200	1432	1521	2036	2176
31/5-3	1984	Yes	2100	-	1555	2103	-
31/5-7	2020	Yes	2610	1698	1957	2510	2638
31/8-1	2011	Yes	2410	1483	2123	-	-
31/3-1	1983	No	2374	1235	1352	1844	1945
31/2-5	1980	No	2532	1533	1536	2070	2201
31/6-1	1983	No	4070	1232	1352	1835	1962
31/6-8	1985	No	2138	1256	1507	2008	2025

4.3 Velocity Model

A velocity model is used to achieve a more realistic interpretation and analysis of the subsurface by converting data from the time domain (ms TWT) to the depth domain (m), the effect of which can be observed in Figure 4.1. Depth converted data present structural features, such as the dip of faults and horizons, more realistically, and so prompts a more precise evaluation of such features (Etris et al., 2001; Lyon et al., 2004). The NCCS team at UiO created the Northern Horda Platform velocity model in 2021, based on well-data and quality-controlled time-depth curves from 15 wells from the Troll and Smeaheia areas, including the 31/5-7 EOS well (Michie et al., 2021).

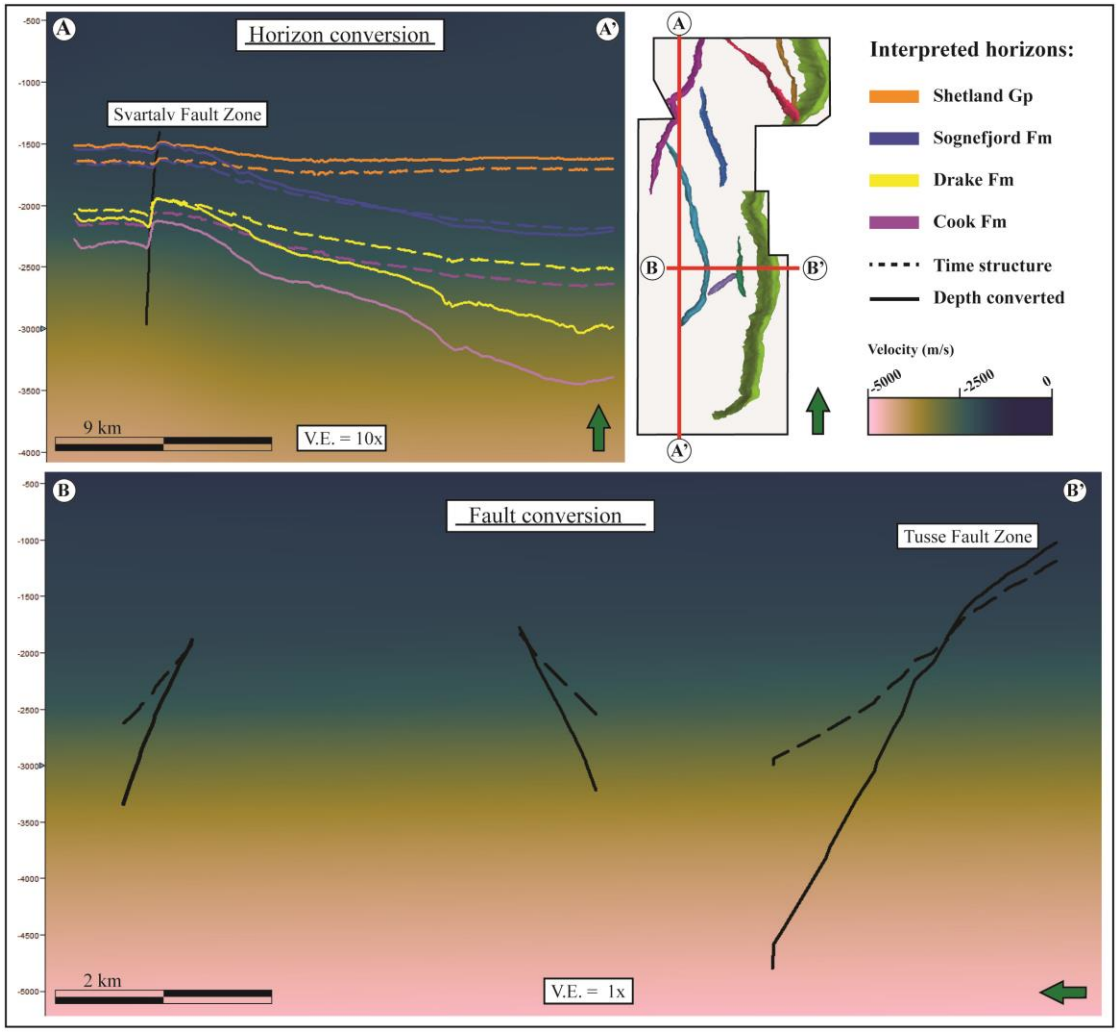

Figure 4.1: Crosslines A-A' and B-B' showcasing the effect of the velocity model on faults and horizon surfaces within the study area. Non-converted surfaces are shown as stippled lines, converted ones as solid lines. Note the vast difference in vertical exaggeration (V.E.) and between the two crosslines.

After the model is applied and the horizon and fault surfaces are converted to metres, a comparison can be made to highlight the effects of the model (Figure 4.1). There is a discernible effect on all mapped layers and faults. Especially, the three deepest layers are positioned progressively deeper through the area, while the topmost layer is surprisingly positioned at a shallower depth. In the southern part of the study area where the layers are deepest, there is a significant change of position (crossline A-A' in Figure 4.1). This is true for the mapped faults as well; they are considerably deeper than what they appeared to be in the time domain. Another change is steeper dip angles and more planar shapes with depth, as opposed to gentler dipping and corrugated in the time domain. Conversion to depth in meters was essential to accurately image fault and horizon surfaces, and to perform rational fault analysis, in the case of this study: slip- and dilation tendency and slip- and fracture stability. In the absence of a velocity model, any reactivation potential analysis would be nonsensical.

4.4 Seismic Limitations

Although 3D seismic surveying is an outstanding method of imaging the subsurface, there exist several weaknesses and limitations to data acquisition, processing, and seismic resolution. It is crucial to know about these limitations and reflect upon them as the interpreter works. Paramount of these concerns is the vertical and horizontal resolution, defined as 1) the minimum distance between two features (in space or time) so that they can be identified separately, and 2) the ability to distinguish separate features involving a single interface (Mondol, 2010; Sheriff, 1977; Sheriff & Geldart, 1995).

The vertical resolution principally depends on three factors, wavelength (λ), seismic velocity (v) and dominant frequency (f_d). Seismic velocity increases with depth as a consequence of age and compaction, while frequencies decreases as greater frequencies are attenuated more readily, thus wavelength generally increases with depth (Brown, 2011; Sheriff, 1977). The limit of vertical resolution is essentially the bed thickness corresponding to the closest separation of two wavelets and is about 1/8 – 1/4 wavelengths (Brown, 2011).

The vertical resolution can be readily calculated on a seismic survey, in this case, the GN10M1, by measuring the time difference over a sequence of reflectors of the same signal, that is, peak-to-peak or trough-to-trough. Measuring a sequence of ten peaks in the survey at 2500-2700 depth, the time difference is 0.293 seconds, meaning the average time between peaks is 0.0293

seconds, giving a dominant frequency of 1/0.0293 s = 34 Hz. Using the previously described Northern Horda Platform velocity model, the velocity at -2500 m is approximately 2250 ms^{-1}. The dominant wavelength can then be calculated using Equation 4.1:

$$f_d = \frac{1}{0.0293\ s} \approx 34\ Hz \quad \rightarrow \quad \lambda = \frac{v}{f_d} = \frac{2250\ ms^{-1}}{34\ Hz} \approx 66\ m \qquad \text{(Eq. 4.1)}$$

The vertical resolution of GN10M1 is then between 1/8 – 1/4 of the dominant wavelength, namely between 8.25 – 16.5 m.

The horizontal resolution of a seismic survey is expressed by the Fresnel zone, a circular zone where the radius is determined by the dominant wavelength, velocity of the seismic wave and depth to the target surface, which helps in controlling the minimum sized feature that can be seen in seismic sections (Denham & Sheriff, 1981; Mondol, 2010). By recording seismic data with a sufficiently small spatial sampling (bin spacing) and performing migration on the data the Fresnel zone can potentially be reduced, thus improving the horizontal resolution (Denham & Sheriff, 1981). For the GN10M1 seismic survey, the horizontal resolution is approximately the same as the inline and crossline (bin) spacing, 12.5 and 25 m, respectively.

4.5 Stress Data and Fault Rock Properties

When performing fault and fault reactivation analysis it is important to define stress conditions and lithology of the host and fault rocks. In this study, the fault models were divided into intervals of reservoir and cap rocks based on the sedimentary successions the faults intersect. As stated in the introductory chapters, the study focuses on the lithological sequences within the Aurora license (EL001) that are identified as suitable cap and reservoir rocks. Namely the Cook and Sognefjord formations as reservoir rocks and the Drake (primary) and Shetland (tertiary) formations as cap rocks (Osmond et al., 2022). In this study, these intervals are referred to as the *Cook*, *Drake*, *Sognefjord* and *Shetland intervals* and the stratigraphy in between the intervals of these sequences has been simplified and assigned attributes matching that of their namesakes. Note that the Cook interval includes the Amundsen and Johansen formations, the Drake interval includes only the Drake Formation, the Sognefjord interval includes the Brent Group and the Krossfjord and Fensfjord formations, and the Shetland

interval is everything between the top of the Sognefjord Formation and the top Shetland Group including the Draupne Formation, Åsgard Formation and others (see Figure 2.3).

The analytical methods used in this study heavily rely on parameters such as in-situ stress conditions and orientations, pore pressure, depth, rock cohesion, angle of internal friction and fault dip and strike. While some parameters can be estimated from literature, assumptions are inevitably made for others. In this, previous studies made on fault reactivation (e.g. Ferrill et al., 2020; Morris et al., 1996; Mulrooney et al., 2022; Sibson, 1977; Smart et al., 2014), geomechanical properties of reservoir, cap, and fault rocks (e.g. Dewhurst & Jones, 2002, 2003; Lothe et al., 2002), as well as reports on licenced areas and drilled wells (e.g. Andrews et al., 2016; Gassnova, 2011, 2012; Osmond, 2021; Skurtveit et al., 2018; Thompson et al., 2022; Wu et al., 2021), are of immense assistance.

4.5.1 In-situ Stress Conditions

Previous research by Thompson et al. (2022) determines that the northern North Sea is of a relaxed normal faulting regime in a state of tectonic quiescence. The in-situ stresses acting around well 31/5-7 are resolved and extrapolated to encompass the entire study area, creating a setting where the magnitude of the principal stresses is related as such $\sigma_V > \sigma_H > \sigma_h$ (Figure 4.2). The maximum horizontal stress (σ_H) impacts the fault surfaces from 90°N and the minimal (σ_V) from 180°N (Thompson et al., 2022). The data presented in research by Thompson et al. (2022), which is as far as the author knows the most recent, most detailed and thus deemed most relevant pressure data for this study, was extracted and presented in Figure 4.2. Some features are necessary to clarify before using these data in the analysis:

- The data does not cover higher elevations than ~70 m above the Draupne Formation, meaning important information for the Shetland interval is omitted.
    - A proxy for the Shetland interval is therefore applied by using the uppermost available pressure information (see Figure 4.2).
- Pressure curves for pore pressure show significant depletion below the Draupne Formation, whereas lesser changes below are possibly due to semi-permeable layers.
    - This has implications for the difference in pressure between the Shetland interval (proxy) and the seemingly less pressured top Sognefjord interval.

- σ_h increases with depth but with great inner fluctuations, thus it is necessary to extrapolate a mean value for the top of the intervals.

Thompson et al.'s (2022) data in conjunction with data from the NPD Factpages allowed the in-situ stresses around well 31/5-7 to be determined for the depth of the four chosen intervals (Table 4.3, NPD, 2022). The pressure data is presented in Table 4.3 and include σ_V, σ_h, and pore pressure (P), whereas σ_H was calculated using a 1.05 ratio between σ_h and σ_H, a typical value for the northern North Sea, as well as the azimuthal orientation of σ_H (Andrews et al., 2016; Thompson et al., 2022). Note that the pressure data for the Shetland is not strictly for the Shetland Formation, but a proxy is used by extracting the data for the shallowest depth presented in Thompson et al. (2022), at approximately 70 m above the base of the Draupne Formation. Note too that specific stress values for the Drake Formation are presented within Thompson et al. (2022), and so there was no need for estimation, see Table 4.3. The pressures were applied to the top of each interval, at the depth they are identified in from well 31/5-7 (Table 4.3, NPD, 2022).

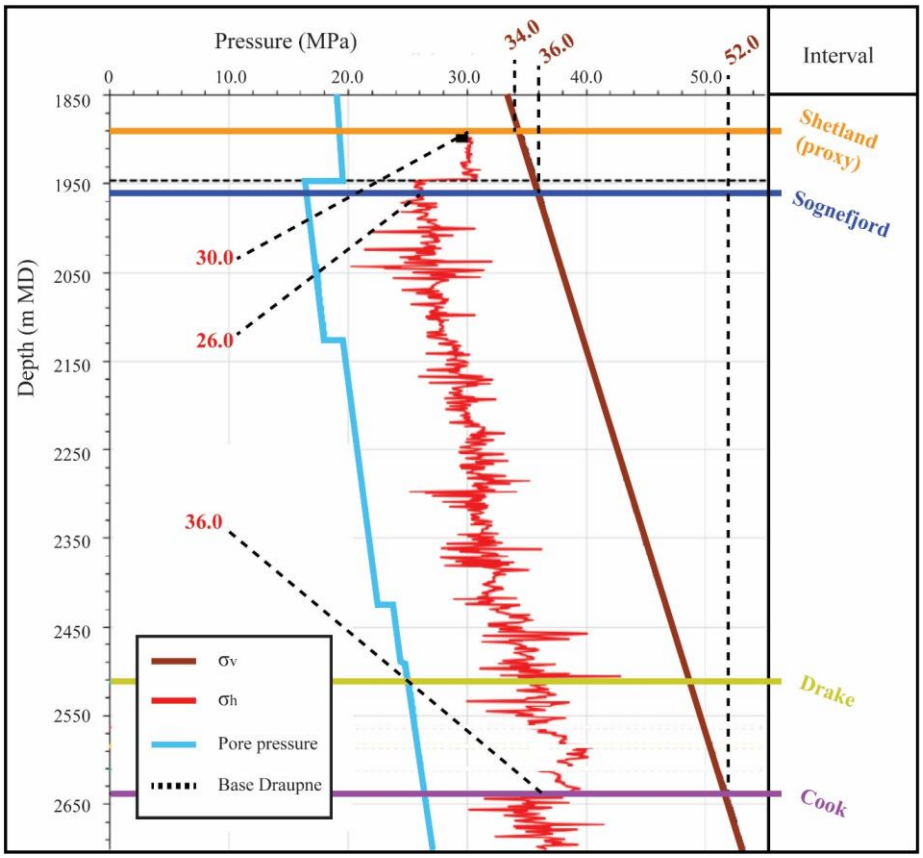

Figure 4.2: Pressure data extracted from Thompson et al. (2022), showing how σ_V, σ_h and pore pressure were determined for the intervals in the study area (Table 4.3). Note that a proxy is used for the Shetland interval, and that pore pressure was measured the same way as σ_V and σ_h. Modified from Thompson et al. (2022**).**

4.5.2 Lithology and Fault Rock Properties

A simplified lithology was synthesized for the four intervals in this study based on their mineralogy and constituents described in subchapter 2.2 and presented in Table 4.3. The theory behind fault rocks is explained in subchapter 3.3, wherein is presented Fisher & Knipe's (1998) method for fault rock classification. This method, along with previously mentioned works on geomechanical properties of reservoir, cap, and fault rocks, and reports on well logs, make it possible to postulate the predominant fault rocks within fault segments intersecting the four intervals in this study (Table 4.4). For example, within the Drake Formation, Thompson et al. (2022) report mineralogic constituents as ~70% clay (of which ~6% is smectite), ~16% quartz, ~2% carbonates and minor constituents of chlorite, muscovite, pyrite and calcite. These factors might affect cohesion and the angle of internal friction in a significant way. Additionally, published works establishing SGR in fault rocks intersecting individual formations and reservoir/cap-rock intervals in the northern North Sea allow determination of SGR for fault rocks within the intervals mapped in this study, and is presented in Table 4.4 (e.g. Osmond, 2021; Wu et al., 2021).

As previously explained in subchapter 3.1, classical geomechanical fault seal analysis considers faults as cohesionless. However, post-deformational processes and burial can cause fault rocks to regain cohesive strength. There are sufficient indicators to assume that this has happened to faults in the study area, given how previous studies have determined their ages of latest seismic activity, their burial depth and indeed reported cementation and cataclasis from i.e. the Sognefjord Formation (e.g. Lothe et al., 2002; Mulrooney et al., 2020). Parameters such as coefficient of friction, angle of internal friction and cohesion are inferred from previous studies on fault rocks by Dewhurst & Jones (2002, 2003), Dewhurst & Hennig (2003) and Mulrooney et al. (2022), see Table 4.4.

It is important to clarify that assumptions are inevitable since actual proof of fault rock composition and physical properties are exceedingly difficult and expensive to provide. Assumptions made are as follows:

I. Sufficient fault healing has occurred for faults to regain some cohesive strength (e.g. Dewhurst & Jones, 2002).
II. The carbonate cementation reported by Lothe et al. (2002) in the Sognefjord Formation causes significant cohesion throughout the formation (Mulrooney et al., 2022).

III. The fault rocks from the mudstone interval of the Shetland interval have more cohesive strength than the shales of the Drake interval, as mudstone host rocks have more cohesive strength than silts and shales (Meng et al., 2006).

IV. The Drake Formation exhibit some cohesion despite the substantial amount of clay minerals, especially smectite, reported throughout the formation (Thompson et al., 2022).

V. Cemented cataclasites exhibit significantly higher cohesion than uncemented, and so despite a low clay content, cataclasites and a deeper burial depth, the sandstones in the Cook Formation do not have the same amount of cohesion as the Sognefjord Formation. There is also some silt in the Cook Formation, which exhibit significantly lower cohesive strength than sand (Meng et al., 2006).

Table 4.3: Parameters attributed the formations mapped in this study. Data for age, depth and thickness of the formation is obtained from the NPD Fact Pages (well 31/5-7), data from stresses and pore pressures are given in MPa and derived from Thompson et al. (2022). *σ_h stress orientation is 180°N. **σ_H is calculated using a 1.05 aspect ratio to σ_h, a typical value for the NCS (Andrews et al., 2016; Thompson et al., 2022). Abbreviations: **σ_v –** vertical stress, **σ_h –** minimum horizontal stress, **σ_H –** maximum horizontal stress, **PP** – pore pressure.

Formation	Group	Age (Myr)	Type	Lithology	Depth (m)	Thickness (m)	σ_v	σ_h*	σ_H**	σ_H azimuth	PP
Shetland	Viking	100 - 61	Cap rock	Mudstone	1698 - 1778	80	34.0	30.0	31.5	90°N	19.5
Sognefjord	Viking	163 - 152	Reservoir	Sandstone	1957 - 2104	147	36.0	26.0	27.3	90°N	19.0
Drake	Dunlin	174 - 168	Cap rock	Shale/clay	2510 - 2638	128	51.2	36.2	38.0	90°N	25.0
Cook	Dunlin	190 - 174	Reservoir	Sandstone	2638 - 2695	57	52.0	36.0	37.8	90°N	26.5

Table 4.4: Parameters attributed to the fault rocks found in faults mapped in this study, the nature of which is postulated using Fisher & Knipe's (1998) classification scheme (see subchapter 3.3),. Abbreviations: **SGR** – Shale Gouge Ratio, **μ** - coefficient of friction, **φ –** the angle of internal friction, **C** – cohesion.

Formation	Type	SGR (%)	Fault Rock	μ	φ (°)	C (MPa)	Comment
Shetland	Cap rock	20-40	Clay Smear	0.45	24	2.0	SGR: see Figure 12a in Wu et. al. (2021)
Sognefjord	Reservoir	20	Cemented Cataclasite	0.80	39	10.0	Carbonate cement and cataclasites reported by Lothe et. al. (2002)
Drake	Cap rock	40+	Clay Smear	0.45	24	1.0	Clay content of ~70% reported by Thompson et. al. (2022)
Cook	Reservoir	>15	Cataclasite	0.6	31	5.0	Low SGR reported by Wu et. al. (2021)

5 Methods of Geomodelling

This chapter presents the workflow, software and analytical methods employed in this study to reach the goals described in subchapter 1.1. The workflow consists of four major stages, where each stage has the be completed prior to advancement into the next stage. The major stages are as follows: 1) literature study, exploring data and mastering the software, 2) creating detailed fault- and seismic horizon interpretation, 3) fault modelling and 4) fault reactivation analysis.

The software Schlumberger's Petrel (v.2021.1) and PETEX Move (v.2020.1) was utilized to complete the study. Exploration of data, seismic interpretation and the products thereof was made and graphically visualized in Petrel. Move was used to produce fault models, perform fault analysis and calculate reactivation potential.

5.1 Horizon Interpretation

It is important to focus one's effort on interpreting seismic data in high detail to create a detailed structural model and so establish the most accurate insight into the subsurface. The interpretation of faults, horizons and other structures will have a significant impact on every part of the structural analysis, especially concerning fault interactions and eventually calculations on fault reactivation potential. Nevertheless, some inaccuracies or inconsistencies inevitably occur that might result in uncertainties in the fault- and horizon products, and so choosing the right strategy to minimize information loss is paramount.

For example, Michie et al. (2021) demonstrate on the same GN10M1 3D survey as used in this study, how choosing a too narrow line spacing adds unnecessary detail to the model that creates more rugose surfaces and amplifies human error without affecting any analysis, as well as being excessively time-consuming. Contrarily, a wider line spacing may underestimate fault segmentation, inaccurately predict fault location, omit subtle variations in fault dip and strike and ultimately predict an overall more stable fault. To minimize the impacts made by such inaccuracies Michie et al. (2021) present an optimum picking strategy of choosing line spacing at 100 m while emphasizing that line-spacing choices hinge on data quality. This strategy identifies all significant fault segments, accurately depicts subtle fault variations, and smooths the effects of human error all the while reducing time spent on the interpretation. It is worth

noting that for detailed seal analysis, a particularly narrow line spacing may be necessary to capture all characteristics of a fault segment (Michie et al., 2021). This study endeavoured to follow the optimum interpretation strategy outlined by Michie et al. (2021).

The interpreted horizons herein are as follows: top Shetland Group, top Sognefjord Formation, top Drake Formation and top Cook Formation. Horizon- and fault-interpretations are depending on each other and are often performed simultaneously or alongside each other. As previously stated, this study focuses on the lithological units within the Aurora License that are targeted for CO_2 storage, and so these four horizons were chosen to represent four intervals of two cap rocks and two storage formations units in succession. The interpretations were assisted by the use of wells, providing data with exceptional vertical resolution when compared to seismic data, alas without horizontal resolution (Figure 5.1).

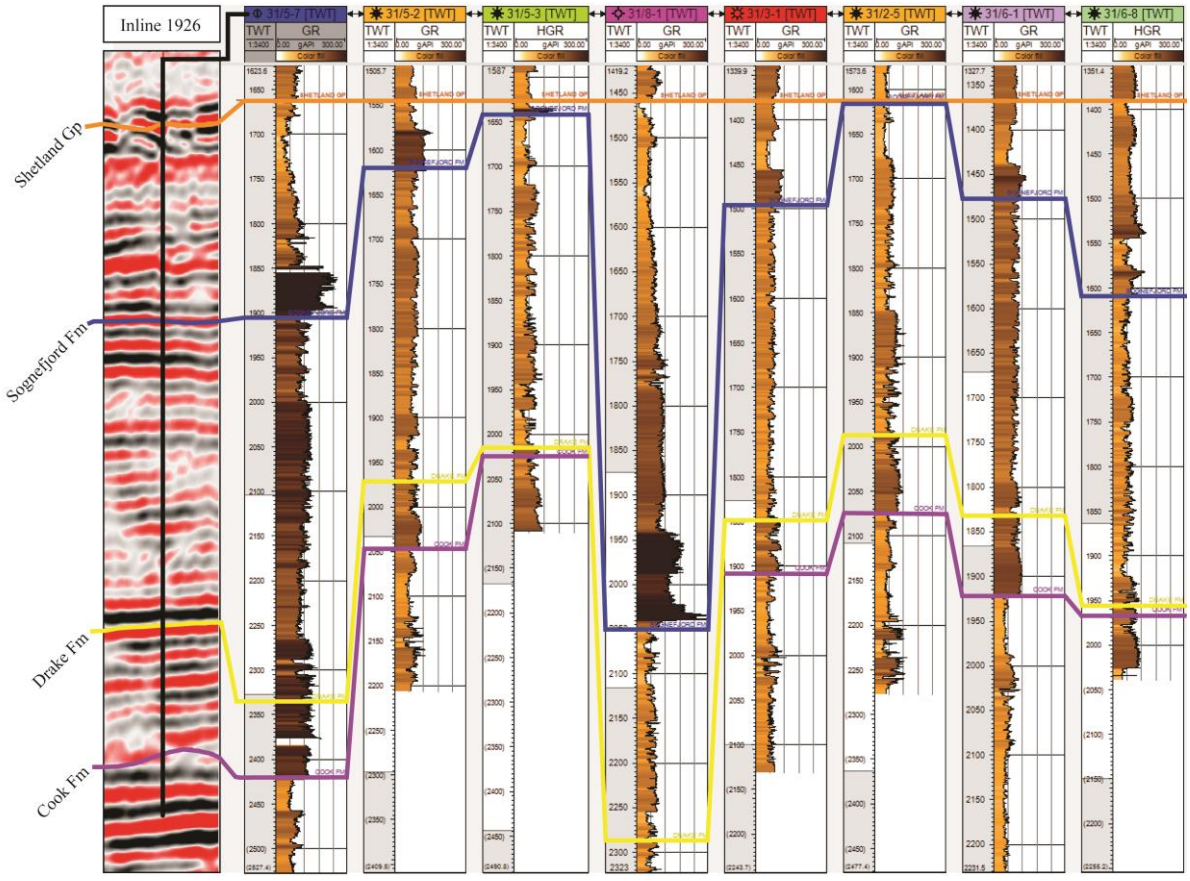

Figure 5.1: Well section for the eight wells utilized in this study, with overlain lines connecting the four horizons between each well section. Gamma-ray logs are shown adjacent to penetration depth in light brown to brown curves. The gamma-ray scale is set from 0-300 gAPI for all wells. Inline 1926 was chosen since it runs through well 31/5-7 from E-W. Note that the well section is flattened for the Shetland Group.

The study makes use of 8 wells, 4 of which are located within the study area (see subchapter 4.2). The wells were chosen for their proximity as well as their depth penetration and level of information (Figure 5.1, Table 4.2). Thus, the wells represent areas where it is possible to interpret horizons with high certainty, and so their use is crucial for areas where the seismic imaging is of faltering quality. Gamma-ray logs incorporated into the well data were utilized to some extent, allowing for simultaneous quality control (Figure 5.1).

The first stage of the workflow for horizon picking was to identify areas where the seismic quality was excellent while simultaneously being in close proximity to a well with sufficient information about the horizon that was being picked (Figure 5.2a). The horizon was then interpreted by using the *Create arbitrary composite section* tool in Petrel to connect several wells. This resulted in a very secure method of identifying the same horizon across the entire study area. In stage two, the horizon was then interpreted systematically every 8th inline and every 4th to create a raw geomodel with 100x100 m grid resolution, following Michie's (2021) strategy (Figure 5.2b).

The 100x100 m grid of interpreted inlines and crosslines creates a basic network of the pending horizon surface. In stage three, Petrel's Autotrack tool was utilized with an 80% confidence rate, the network is then completed into a surface by automatically filling in the empty squares between the lines (Figure 5.2c). The horizon surface was then revised and quality controlled to ensure a model with a high level of geological credibility. Where obvious interpretation errors or irrational deviations in the interpretation occurred, the interpreted grid was revisited and adjusted before being autotracked repeatedly until a satisfactory result was achieved. The autotracked horizon interpretations were then converted to a surface with a 25x25 m grid increment spacing and displayed as time-structure maps. Lowering the grid increment spacing would slightly increase the accuracy of the surface model, but this was chosen to alleviate the pressure of big data handling since the surface models are of nominal importance to this study.

The fourth step of the process is to depth convert the time-structure surfaces using the previously described Northern Horda Platform velocity model, whereupon a more geologically accurate is produced in a more intuitive scale, metres (Figure 5.2d). This was done using Petrel's *General domain conversion* tool with standard settings. In this stage, the horizon surfaces are also smoothed using Petrel's *Surface Smoothing* tool with two iterations and a filter width of two with the *combo smooth* averaging method. This operation flattens irregularities in the surface, usually located in areas of poor seismic quality, allowing for a

more easily comprehendible surface where small irregularities are reduced but significant features are kept. Afterwards, the surface was again quality controlled to ensure depth conversion and smoothing had not removed important geological features or compromised the geological credibility. Indeed, this stage was performed on copies of the surfaces, to guarantee that nothing was lost.

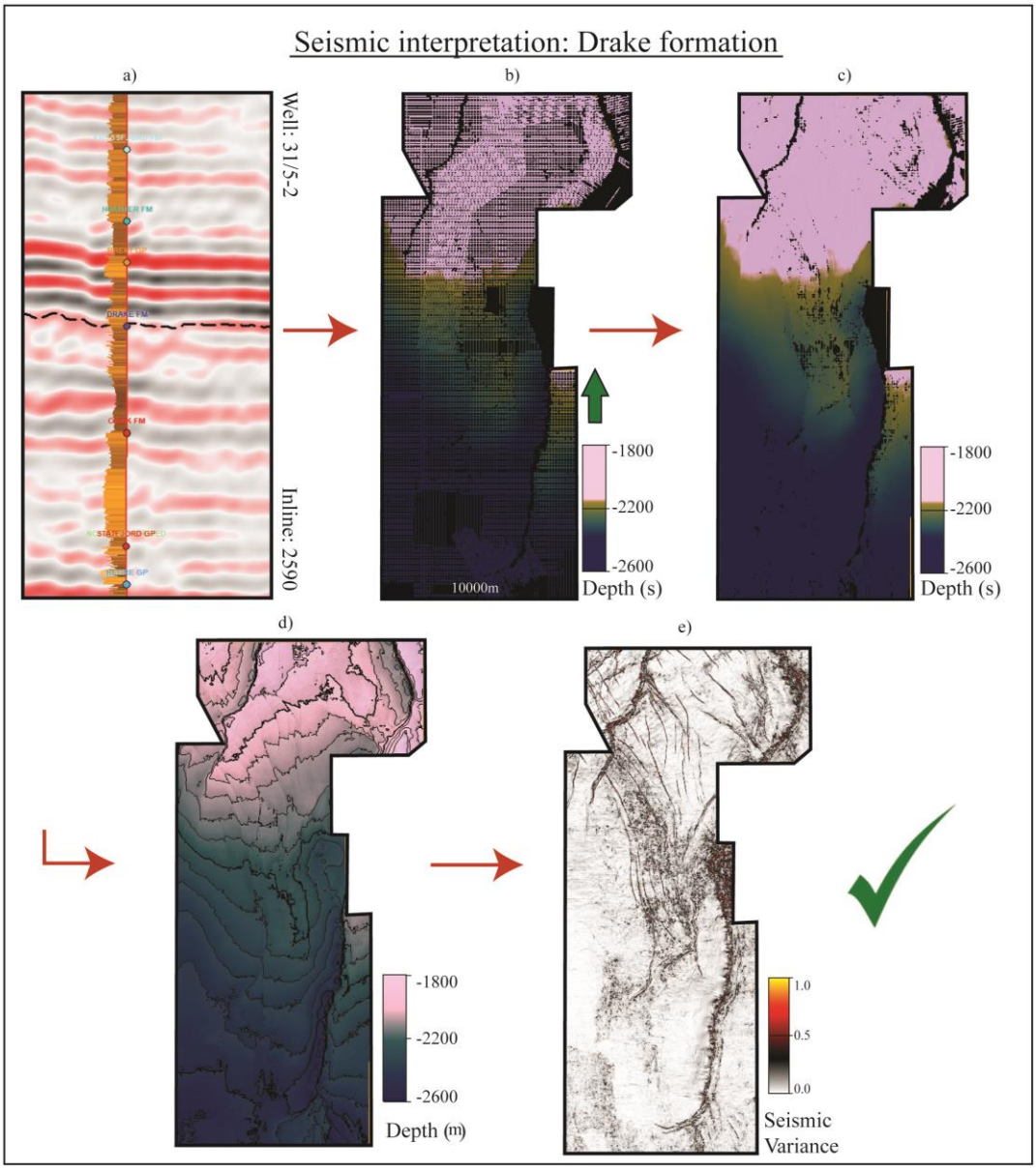

Figure 5.2: The five stages of horizon interpretation and surface creation. a) careful selection of wells to ensure that the reflection being picked is in fact the horizon being sought, in this case, the Drake Formation, b) interpretation grid, c) autotracked grid, d) depth-structure horizon surface, e) seismic variance map. Note change from time to depth from c)-d).

The final step involves creating maps of seismic attributes, as derived from basic seismic

information of time, amplitude, frequency and attenuation (Brown, 2011). Mapping seismic attributes is an exceptional way of visualizing aspects of the subsurface that are not evident in conventional seismic images. One such seismic attribute is the Seismic Variance (edge method), which estimates trace-to-trace variances in the seismic signal, thus revealing discontinuities in the seismic data related to structural features (i.e. faults) or stratigraphic terminations (Petrel E&P Software Platform, 2015). Seismic variance can be created for a single slice or surface as in this case (Figure 5.2f), or for an entire seismic cube as will be used in the mapping of faults (subchapter 5.2).

All six steps outlined in this chapter were executed for all four intervals.

5.2 Fault Interpretation

Calculating the reactivation potential of faults within the Aurora Area is the ultimate goal of this study. To properly discern any risk of reactivation, it is crucial that the fault interpretations must represent the actual faults as accurately as possible. Fractures and faults influence the strategy of exploration and production wells, can serve as important barriers or conduits for fluid flow and pressure communications and are more often than not the defining elements of structural traps.

Several authors have previously explored how the method of interpretation impacts the fault models morphology, vertical displacement and fault length (e.g. Badley et al., 1991; Cunningham et al., 2021; Faleide et al., 2021; Lothe et al., 2018; Michie et al., 2021). These factors depend on how the person that does the interpretation can accurately capture the properties of the fault and ultimately affects several possible fault analyses such as fault seal evaluation, estimates of storage volumes, pressure propagation models and fault reactivation potential. All aforementioned authors agree that the denser the interpretation spacing, the more detailed and realistic fault models are assembled. Therefore a substantial amount of time and effort was allotted to interpreting faults. In total, four thick-skinned and six thin-skinned faults (three of which are antithetic and three synthetic), were mapped in this study. Their given names and attributes are listed in Table 5.1 and presented in Figure 5.3. Note that although several fault segments are well-known basement-involved faults, they are very seldom mapped below -4000 TWT to save time, as fault surfaces far below the chosen intervals do not affect the subsequent fault reactivation analyses.

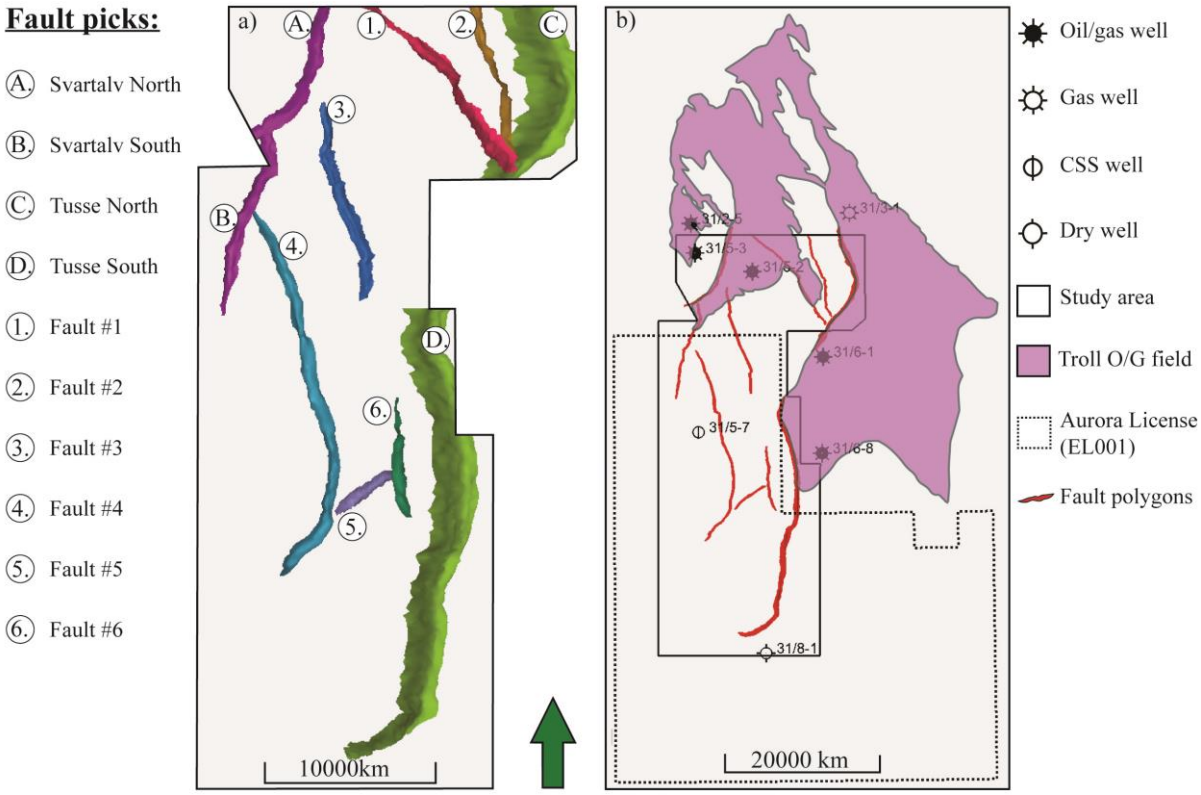

Figure 5.3: Map view of the ten faults picked within the study area. a) naming system for the 10 faults, Tusse and Svartalv are named by the NPD and here parted into two segments, the rest are given arbitrary names. b) fault polygons for the Drake interval for the mapped faults and their spatial relationship to the study area, nearby wells, the Aurora Exploitation License and the Troll oil and gas field.

The interpretation was conducted manually, utilizing Michie et al.'s (2011) strategy of 100 m increment spacing, on seismic reflection data in the time domain. The interpretation was performed by creating fault sticks on vertical cross-sections within the study area, which were then used to generate fault surfaces. To achieve the most accurate interpretation, a fault is best picked when the seismic sections being evaluated are oriented orthogonal to the fault's strike. In the study area fault strikes often deviate from the orientation of the inlines (E-W) and crosslines (N-S) in the GN10M1 survey. When the inlines and crosslines were unfavourably oriented manually constructed composite sections were used to view the fault from an orthogonal angle. Seismic variance applied to the 3D cube was used in map view to navigate and help interpret the fault trace, as it is very often better seen therein. In areas where faults could be hard- or soft-linked, linked by relay ramps or otherwise interfering with each other, the converging faults were interpreted as closely as possible, with the use of even denser increment spacing if necessary. The fault surfaces were then continuously quality controlled

and areas where the fault model exhibited unreasonable or jagged features were revisited in the reflection data. These errors were then corrected by granting the area more attention or interpreting with even denser spacing, down to the limits of the survey (12.5 m for inlines, 25 m for crosslines).

Table 5.1: All ten faults mapped in this study. Thick-skinned means that displacement is basement-involving. The six thin-skinned faults are listed as either synthetic or antithetic to the four master faults.

Fault name	Thick-skinned?	Synthetic?	Entire fault trace?	Comment
Tusse North	Thick	-	No	Northern part is outside the study area
Tusse South	Thick	-	No	Middle part is outside the survey area
Svartalv North	Thick	-	No	Northern part is outside the study area
Svartalv South	Thick	-	Yes	Splaying out from Svartalv North
Fault 1	Thin	Anti	Yes	Hard-linked with Tusse North
Fault 2	Thin	Syn	Yes	Synthetic to Tusse North
Fault 3	Thin	Anti	Yes	Antithetic to Svartalv South
Fault 4	Thin	Syn	Yes	Larger splay south of Svartalv
Fault 5	Thin	Syn	Yes	The only ~NE-SW trending fault
Fault 6	Thin	Anti	Yes	Hard-linked with Fault 5

Additional quality control was achieved using the previously described variance attribute maps as multilevel time-slices, especially when considering the upper extent of the faults. Unfortunately, the quality of the seismic data degrades with depth. Since seismic attributes draw from the information of the regular seismic, the variance maps tend to become exponentially poorer in the deeper parts of the subsurface, and accordingly become next to useless when assessing the lower extent of faults. The fault's vertical extent was to a minor degree constrained by 2D seismic data, but primarily fault-mapping was performed in conventional 3D reflection seismic data.

5.3 Fault and Horizon Modelling

When the fault models were adjusted to a satisfactory state, fault heave polygons were created to illustrate where faults intersect with each horizon surface (see Figure 5.3b). Completed fault models were then depth converted using the Northern Horda Platform velocity model with the same tool as the horizon surfaces. The application of the model affected the faults more

eminently than observed for the horizon interpretations by increasing their depth to a higher degree. A prominent change in dip and strike is also noted, where the dips appear to be much gentler and the faults become less corrugated compared to the time domain.

After both fault and horizon models were completed with satisfaction the next step in the study was to export the data in preparation to perform analyses in the PETEX Move software. Horizons were exported as *Zmap+grid* ASCII data (points) and faults as *Charisma fault sticks* (2D fault sticks), also ASCII data.

All fault sticks were then imported into PETEX Move and modelled into fault surfaces using the *Delaunay Triangulation* method. The fault surfaces were then reviewed to make sure they matched in Move and Petrel in case data was lost or the fault surfaces were altered in any way. Erroneous triangles were then corrected or removed. Horizon surfaces were imported as grid meshes and subsequently made into surfaces by the same triangulation method. The horizon surfaces were quality controlled and assigned to a stratigraphic column where they were given a token colour and attributed ages, thicknesses and an oversimplified lithology (Table 5.2). The data is gathered from well logs from the 31/5-7 well (NPD, 2022).

Table 5.2: Token age, thickness, colour and oversimplified lithology for each interval. The amount of data points, or vertex attributes (V.A), for all fault surfaces within each interval is provided.

Formation	V.A.	Age (Ma)	Thickness (m)	Lithology	Colour
Shetland	13638	61	80	Shale	Orange
Sognefjord	24017	152	147	Sandstone	Blue
Drake	24666	168	128	Shale	Yellow
Cook	13416	174	57	Sandstone	Purple

As explained in chapter 4, the study area is divided into four intervals of cap- and reservoir rocks, the Shetland, Sognefjord, Drake and Cook intervals. This was done to create a fault reactivation analysis that could check conditions between each storage unit (Dunlin and Viking) and highlight where the risk of fault reactivation is the highest. Additionally, the intervals were designated several properties such as in-situ pressure, pore pressure, SGR%, coefficient of friction, angle of internal friction and cohesive strength (see subchapter 4.5). To apply these properties to the appropriate parts of the fault, the faults were horizontally split into four intervals. Since the hanging walls contain the storage units, the splits were made where the four horizon surface interval's hanging walls intersected the faults.

This was done in four stages, first by using Move's Fault Analysis tool where cut-off lines are created automatically for both the hanging wall and the footwall intersection between a given fault and a given horizon surface. The tool works well for very simple or smaller faults – in most cases where the surfaces intersect, they are relatively flat and without drag. In cases of larger, more corrugated faults (e.g. Tusse North, Tusse South and Svartalv North), a different approach was necessary. In these cases, cut-off lines were generated by creating a two-dimensional line connecting data points on the horizon surfaces that were in close proximity to the faults. The lines, on both footwall and hanging wall, were created to make as much geological sense and to include as many features as possible, while at the same time eliminating local errors or unnecessarily sizeable drag. The lines were then extrapolated horizontally into small surfaces that intersected the fault surfaces. Intersection lines were then created where these new surfaces intersected the fault surfaces, effectively representing where the original surfaces intersect the faults. This method is very effective when modelling truncated layers by omitting near-fault folding or smaller errors, thus disregarding lesser variations and noise in the actual fault offset. These intersection lines were then used as cut-off lines.

Regardless of how the cut-off lines were created, they were then used to create vertical displacement profiles with the Displacement Analysis tool in Move. Hanging wall cut-off lines were used to split the faults into intervals by using the Split tool in Move. The latter was successfully done for all ten faults, an example from the Tusse South fault surface is presented in Figure 5.4. The former was done for the four master faults, as very little displacement existed on the smaller faults. With all faults divided into intervals matching that of the surfaces, a total of 40 fault surfaces were primed for analysis.

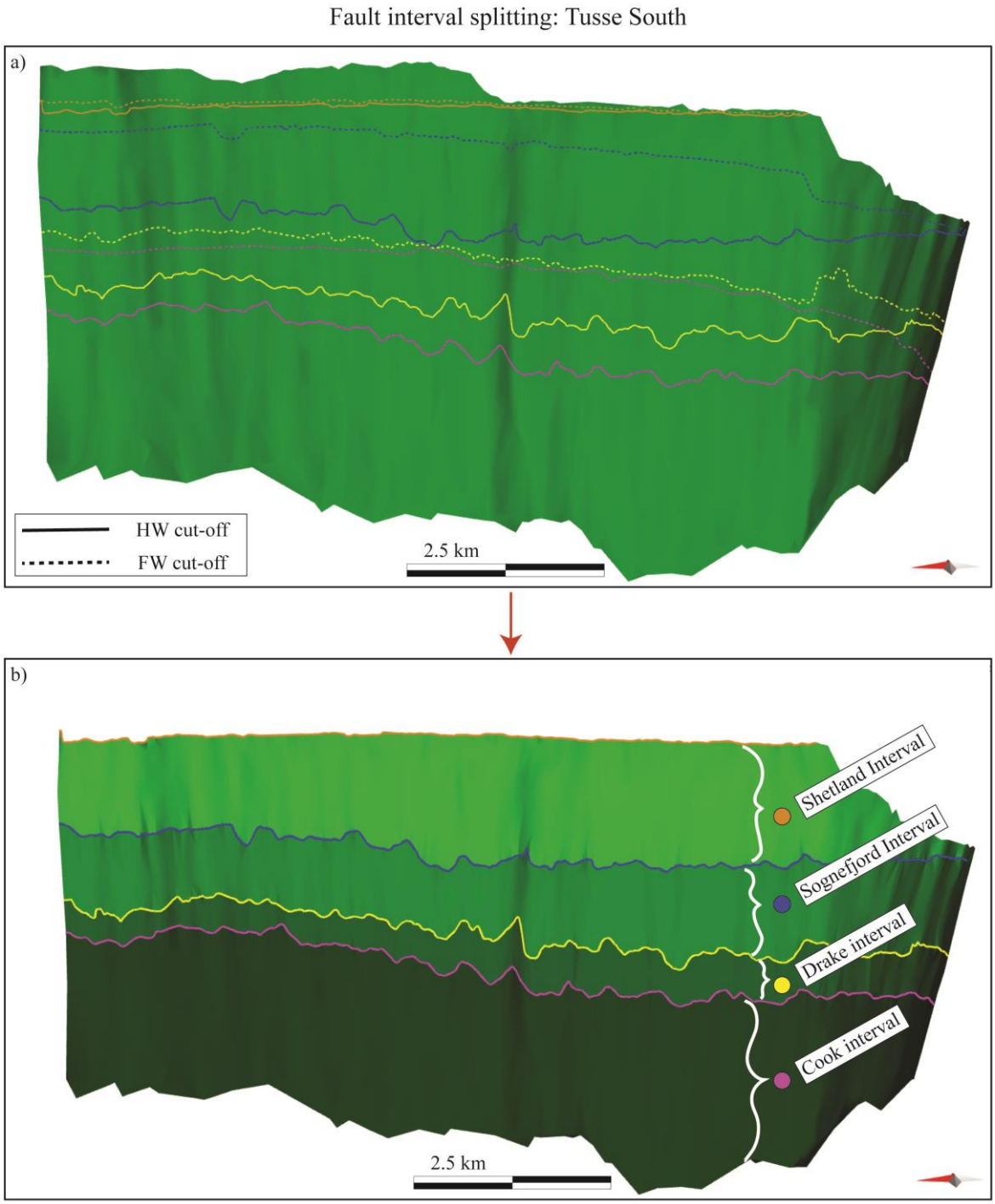

Figure 5.4: Tusse South fault is used as an example of how splitting faults sub-horizontally into intervals was achieved. a) the entire fault surface is shown with cut-off lines for the footwall (stippled lines) and hanging wall (solid lines), and b) the fault surface is split into four intervals based using the hanging wall cut-off lines. The lines are coloured by interval (Table 5.2). Abbreviations: HW = Hanging wall, FW = Footwall.

5.4 Analytical Stress Analysis

To correctly assess the stability and reactivation potential of a fault segment, several analytical methods are necessary. The methods applied in this study are complementary and are described in detail in chapter 3 but are listed here as a reminder: slip tendency, dilation tendency, slip stability and fracture stability. An overview of the methods, their symbols and equations are listed in Table 3.1.

The four analyses were performed on each fault interval by using the *Stress Analysis* tool in Move. This tool allows the user to adjust in-situ stress conditions and orientations, angle of internal friction and cohesion of each fault segment the analysis is performed on. The 40 fault surfaces were placed in groups for each interval, and the analysis was executed by assigning the properties from Table 4.3 and 4.4 (subchapter 4.5), to each fault surface, representing their respective interval.

When the Stress Analysis tool is executed, *vertex attributes* are created by the software for each triangle constructed by the Delaunay triangulation method. For example – the values generated for a faults dip are an accumulation of the dip angles for every triangle the fault surface consists of. The same is true for the four analytical methods, i.e. each triangle is given a single value of slip tendency and coloured according to this value, and the amassed set of data points results in the complete analysis. In this project, the number of data points, or vertex attributes, is given for all faults within each interval in Table 5.2, summing a total of 75737.

Move then presents the results in four different ways: numerically as *vertex attributes* for each triangle on the fault surface and visually as Mohr diagrams, polar diagrams and pressure profiles (e.g. Figure 6.14). The pressure profile is a good tool to see how the stress state at a given depth deviates from hydrostatic and lithostatic pressure, while the Mohr and polar diagrams provide an intuitive way of visualizing how close to a critically stressed state a fault is under the current conditions. By way of example, one can readily calculate how much extra pressure a fault can tolerate before reactivating by running the Stress Analysis tool for slip stability and observe which colour is assigned to different fault surfaces. In Move, the blue colour represents areas of low risk, increasing through green, yellow, red and purple. Note that the colour scheme and scale within the Stress Analysis tool are unchangeable, and so values that appear on figures in the upcoming chapter 6 might not always be of the same scale. They are made to be as consistent as the software allows.

6 Results

As previously stated, the main objective of this study is to calculate the reactivation potential and assess the Aurora field as a feasible site for CO_2 storage. This chapter aims to create the background for discussing how the Drake Formation cap rock will respond to an increase in pressure from the injection of CO_2. As previously stated, the Drake Formation is the intended cap rock for the Northern Lights project, and so the results presented in this chapter will be focused on that formation in particular, especially investigating the fracture stability analysis. Figures showing seismic and surfaces will be presented in depth unless explicitly stated.

The structural architecture and characterization of the faults and horizon surfaces created in this study are focused on and described to establish their spatial relationship to each other, wells and well-known areas like the Troll oil and gas field and the Aurora Exploration License (EL001).

Results from the Stress Analysis tool in Move are presented for all fault surfaces cumulatively, and for the Drake Formation particularly. The analysis generated a total of 75737 data points that are plotted as Kernel smoothing density (Ksd) plots by the MatLab software, to effectively showcase differences in dip, slip tendency, dilation tendency, slip stability and fracture stability alongside the figures generated by Move. Presented data from in-situ- and pore pressure and fault reactivation potential are calculated in MPa, but it is advised to pay close attention to scale and colour bars, as Move allows very limited adjustments to the automatically generated figures.

6.1 Horizon Models: Surfaces

Shetland, Sognefjord, Drake and Cook horizon surfaces are presented in this subchapter as depth-structures, and figures showcasing seismic attributes such as variance are provided. These surfaces are what define the chosen intervals of this study, and so it is important to note their relationship to each other, especially considering depth, basin tilt and interval thicknesses.

6.1.1 Depth-structure Surfaces

Figure 6.1 displays these surfaces in depth-structure maps, showcasing a part of the Horda Platform with a significant southward tilt. The uppermost horizon, the Shetland Group, is the only one that exhibits a tilt with an additional eastward component. The deepest parts of the underlying horizons are seen at intersections with the Tusse South fault, which causes significant increases in depth in the hanging walls (Figure 6.1b,c,d).

Based on the depth-structure maps it can be observed that the thickness between the Drake and Cook formations remains relatively constant at around 200 m throughout the study area (Figure 6.1c,d). An increase in thickness is seen between the Shetland and Sognefjord formations, where the difference is ~150 m in the north, increasing to ~650 m at the southern end of the study area wall (Figures 6.1a,b and 6.2). This is especially seen in parts of the Tusse South hanging wall.

The gaps are made apparent in an inline cross-section running across the study area, showcasing the horizon intervals' spatial association (Figure 6.2). Within the study area, the Sognefjord horizon range from about -1500 in the north to -3500 m in the south, at a distance of ~44 km (the length of the study area), this results in an average structural tilt of 2.60°. A significant thickness increase is observed in the Shetland interval south of the EOS 31/5-7 well (see insert in Figure 6.2). This increase is not recognized in the underlying intervals, which maintain their separation.

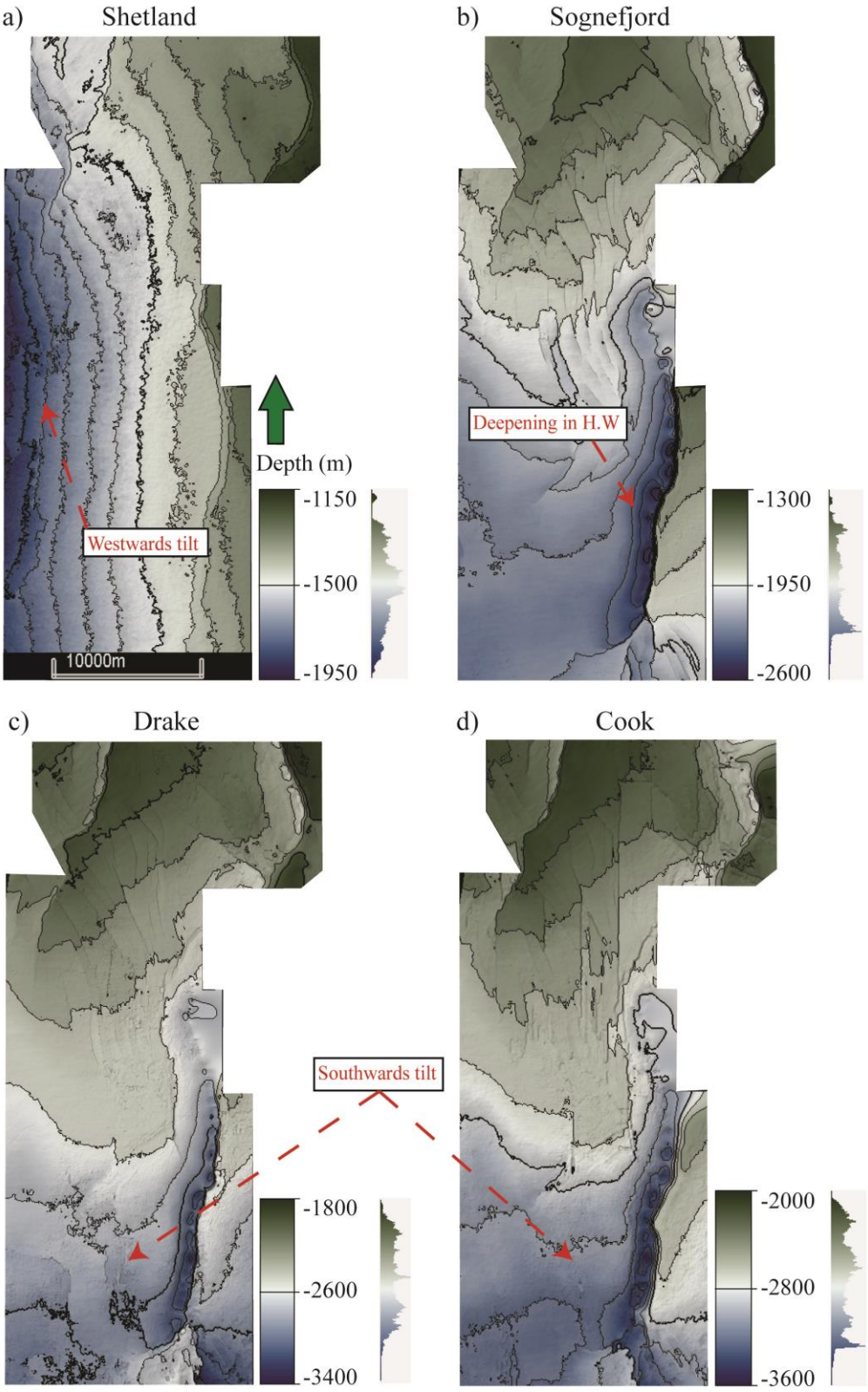

Figure 6.1: Depth maps of the four mapped horizons, colour draped by meters below the sea surface. a) Top of the Shetland Group, the tertiary sealing formation. b) Top of the Sognefjord Formation, the main reservoir unit of the Viking Group. c) Top of the Drake Formation, the primary seal and topmost formation of the Dunlin Group. d) Top of the Cook Formation, the uppermost reservoir formation within the Dunlin Group.

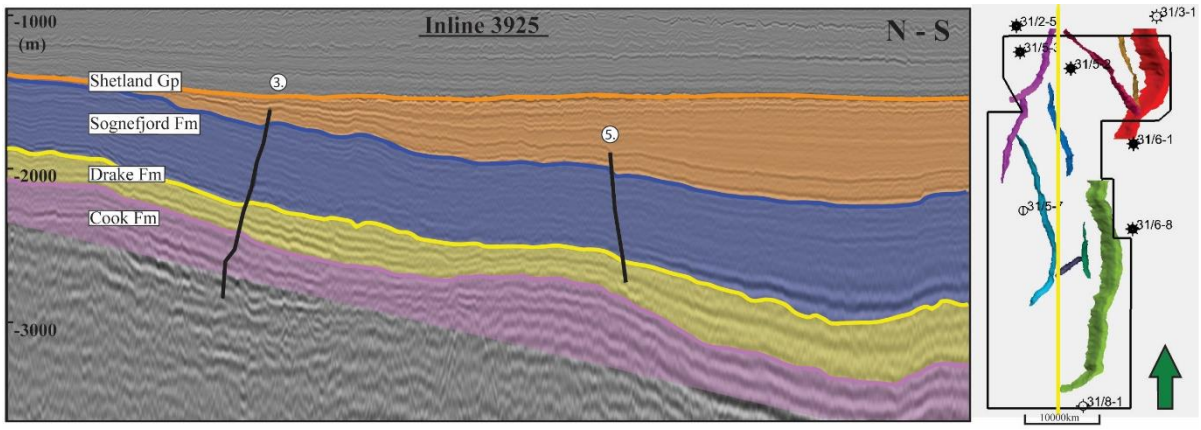

Figure 6.2: The four mapped horizons shown in a composite cross-section running through the study area, highlighting the increased difference in depth, deepening towards the south. Note that the lower extent of the Cook Formation is arbitrary in this figure. Insert on the right is from Figure 5.3a.

6.1.2 Seismic Variance Surfaces

Investigating the seismic variance maps it is apparent that the uppermost Shetland Group is a horizon of relatively quiescent seismic activity, except for some discontinuities at the intersection zones of Tusse South and North and Svartalv South and North (Figure 6.3a). Polygonal faulting is also apparent throughout the entire study area at the Shetland interval level (Figure 6.3a).

Past the depth of which the Drake Formation is located, the seismic variance somewhat loses focus, and incredible detail is difficult to achieve. However, the majority of the fault population seen in 6.3b is still quite recognizable through Drake Formation and down to the Cook Formation level (Figure 6.3c,d).

Further investigation into the seismic variance attribute maps reveals the abundance of faulting in the northern parts of the study area. The heaviest abundance of faults appears beneath the Troll oil and gas fields, but a population of SE-NW-striking faults possibly connecting the Svartalv fault to the west and the Tusse fault to the east is also apparent, especially in the Sognefjord variance map (Figure 6.3b). This population seems divided into at least two generations of faulting, as some parts have a more or less straight trace through i.e., Sognefjord and Drake formations, while another is more arcuate.

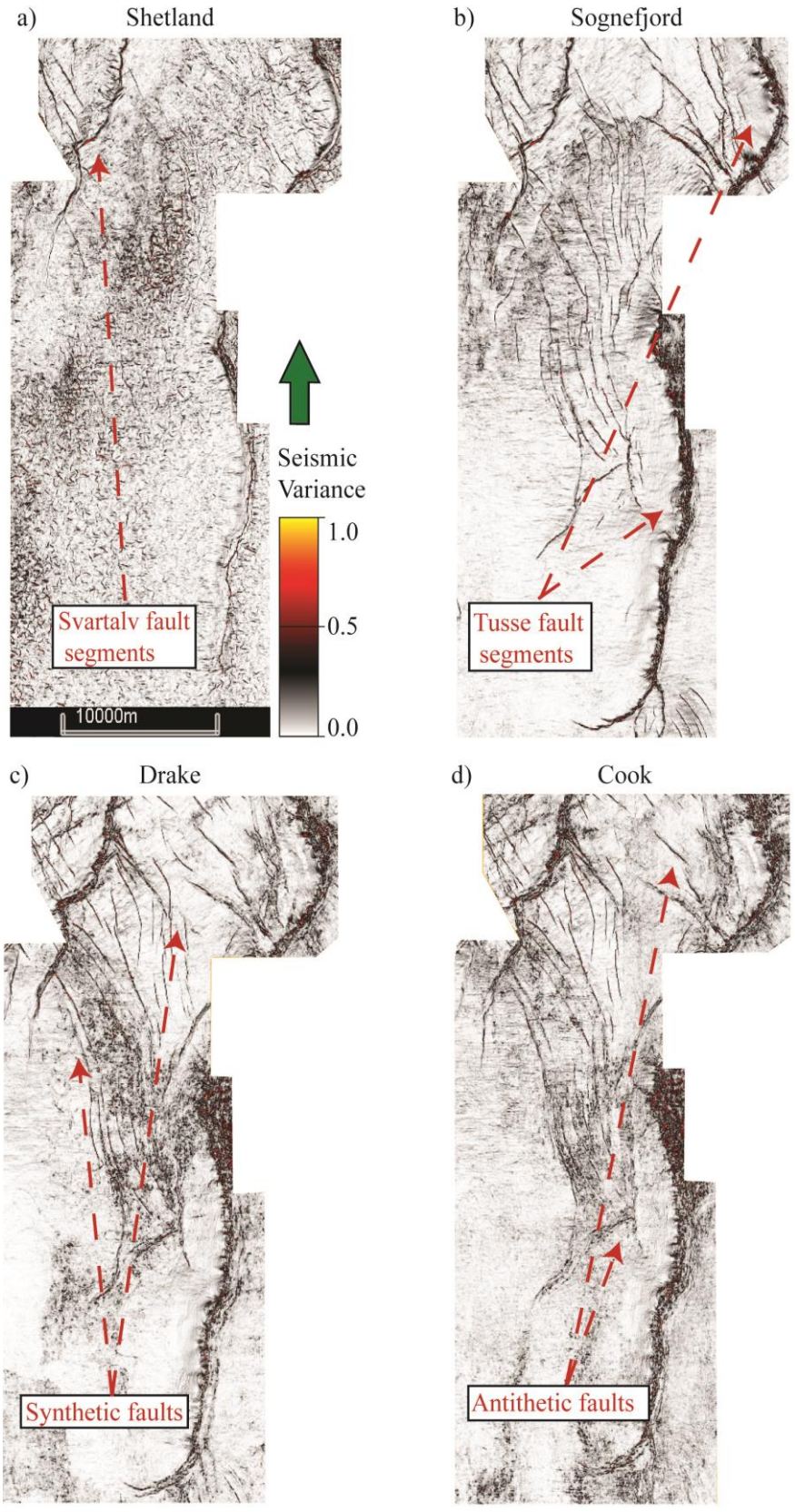

Figure 6.3: The four mapped horizons colour draped by their Seismic Variance attribute, highlighting discontinuities in the seismic signal, especially fault traces. Significant features of the study are pointed out. Note that the named features appear in both a, b, c and d), even if only appointed once.

6.2 Fault Models: Surfaces and Data

In this study, ten approximately N-S striking faults were mapped and modelled inside the study area (Figure 6.4). Unless previously named by the NPD are given arbitrary names loosely based on their spatial location, see Figure 5.3. The ten fault picks are presented in seismic cross-section, as numerical data and displayed as surfaces and polygons showcasing significant structural features such as dip and displacement. The faults are divided into two populations outlined below:

1) 1st-order/thick-skinned faults that penetrate and displace the basement-cover contact. This includes the Svartalv North and South as well as Tusse North and South.
2) 2nd-order/thin-skinned faults that have no basement involvement. This population includes faults #1-6.

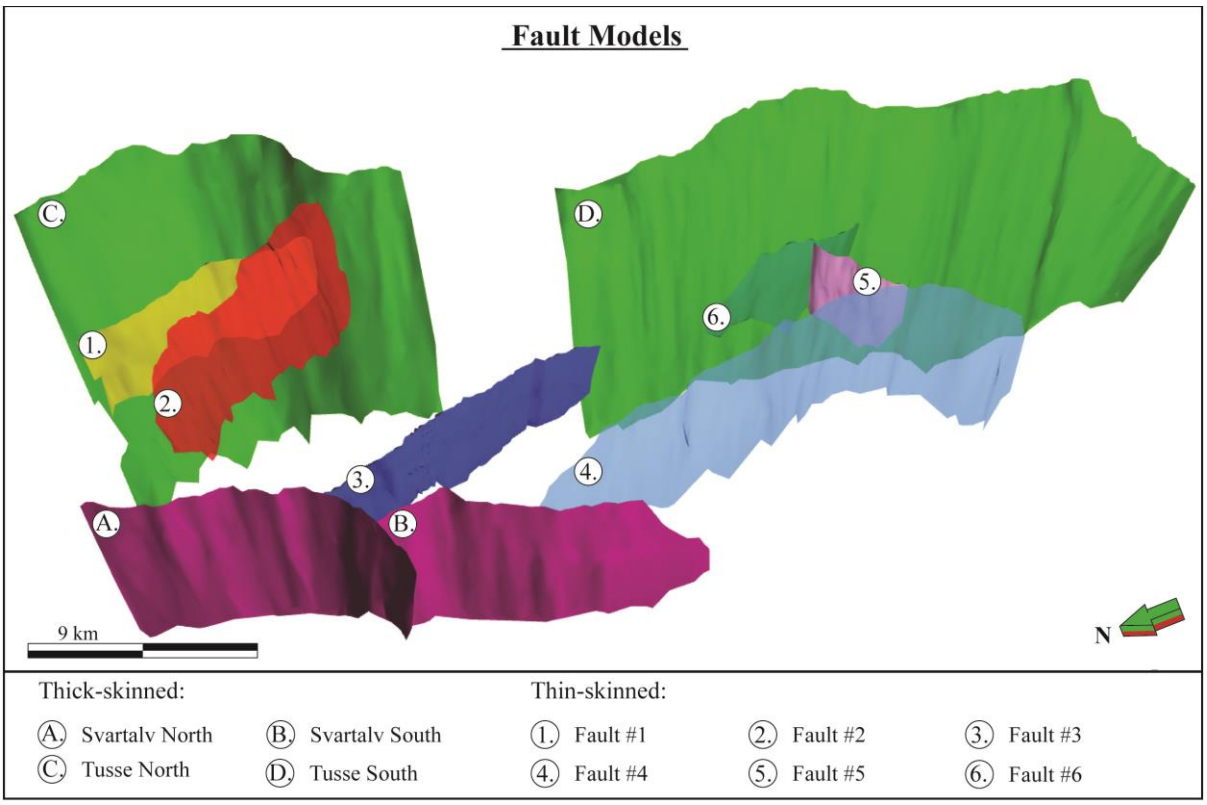

Figure 6.4: All fault models created in this study, including their given names. The nomenclature follows Figure 5.3. Note that thick- and thin-skinned correspond to 1st- and 2nd-order faults, respectively.

Figure 5.3b shows that four of them are entirely within the Aurora Exploitation License, two are partly inside and four are entirely outside. The northern part of the study area is beneath the Troll oil and gas field, where the Draupne-Shetland cap rock interval is known to be able to hold significant storage of oil and gas.

Figure 5.3b also presents fault heave polygons for the fault's intersection with the horizon surface of the top Drake Formation, aiming to establish their size difference in terms of spatial extent and displacement within the formation desired as the primary cap rock for CO_2 injection in the Aurora Exploration License (EL001).

Faults Tusse South and North as well as Svartalv South and North are thick-skinned master faults, deepening towards the west. Faults #1-6 are thin-skinned (of which faults #2, #3 and #6 are antithetic), and exhibit no trend of deepening. In terms of strike direction, the only fault that deviates from a general N-S trend is fault #5, exhibiting a mean strike angle of 56˚N. Nearly all faults are west-ward dipping (synthetic), while a few of the 2nd-order antithetic faults are east-ward dipping (Figure 6.4).

The size differences, general dip direction and angle of the fault population are made evident in the three provided seismic sections (Figure 6.5). These sections were constructed to showcase the depth of penetration (within the seismic resolution) and true dip angles, utilizing the Northern Horda Platform Velocity model and vertical exaggeration of x1 (see chapter 4). Figure 6.5 also shows how all the mapped faults intersect with the top Drake Formation, albeit with a vast difference in vertical displacement (see lower right corner).

As mentioned, there is an observable abundance of faults in the northern part of the study area, especially in the vicinity of the Troll oil and gas fields (Figure 5.3b & 6.6). However, the largest segments mapped, Tusse South and fault #4, both reach far into the south (Figure 6.4).

The thick-skinned faults in this population exhibit more or less share mean strike direction, excepting a fault segment in the southern parts connecting Tusse North and South. This is somewhat seen in Figure 5.3 as the southern parts of Tusse North where it jogs towards the east. Unfortunately, this part of the fault trace was outside the GN10M1 survey coverage, leaving the segment unmapped

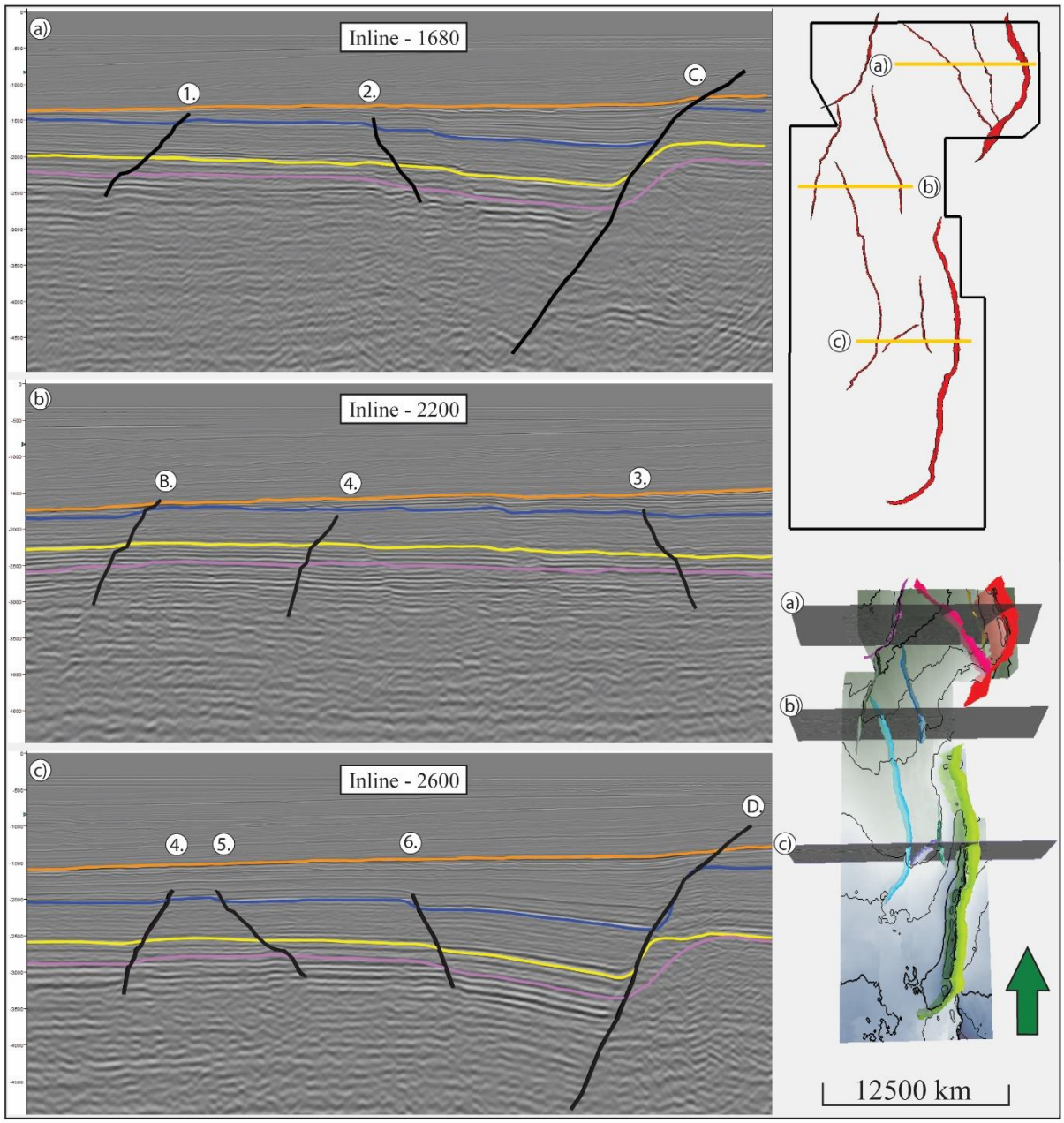

Figure 6.5: Picked faults in seismic showcasing depth and true dip, with a vertical exaggeration of x1. The four mapped horizons are also shown in orange-, blue-, yellow- and purple-coloured lines (Shetland Group, Sognefjord, Drake and Cook formations, respectively). The upper right corner shows how the faults intersect with the Drake Formation.

Svartalv North also has a jog towards its southern termination. The shift in strike direction coincides with the hard linking connecting point of Svartalv South, which possibly began as a smaller splay before being able to accommodate more strain and evolving into a thick-skinned segment of its own (A and B in Figure 6.4).

Figure 6.6 displays all six thin-skinned faults in their entirety, and their spatial relation to each other. No vertical displacement was calculated for the thin-skinned faults, as the displacement there is comparatively very low. Faults #1 and #2 (antithetic) are in close proximity to Tusse North, converging towards the south to hard link with the larger, thick-skinned fault. Unfortunately, the seismic resolution made this impossible to depict. Antithetic fault #3 and synthetic fault #4 splay off from Tusse North and South, respectively. It is unclear due to limited vertical seismic resolution whether they hard link to their respective parent fault segment.

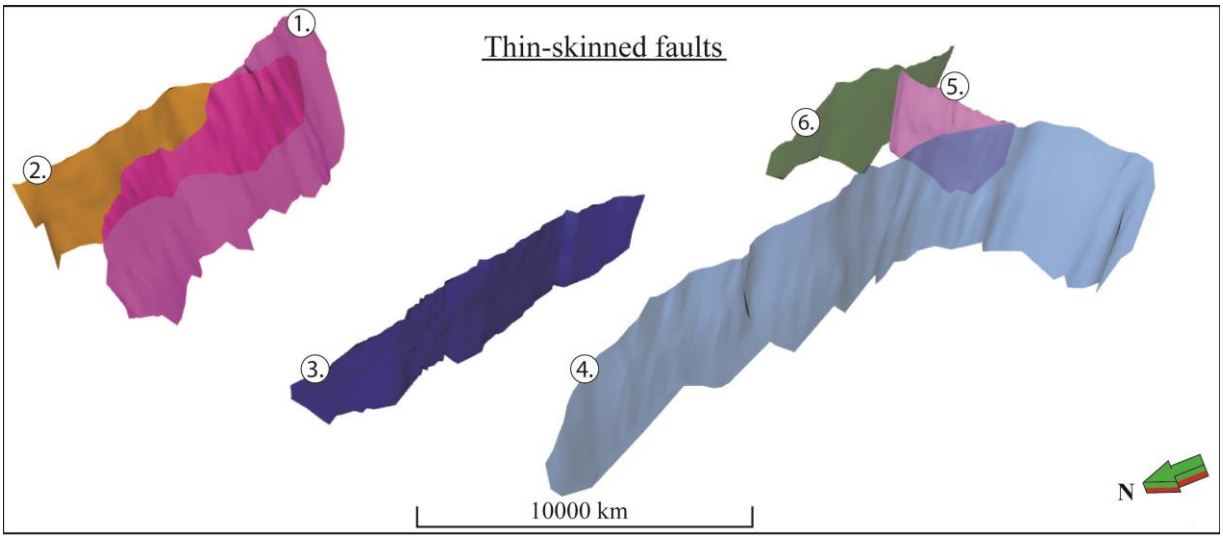

Figure 6.6: The six mapped thin-skinned faults, given an arbitrary colour. The fault surfaces in front are made transparent (20%) in order to see all faults. Numbers follow the naming system from Figure 5.3.

Fault #5 is seen in Figure 6.6 as the only fault that severely deviates from the strike direction of the fault population. Likely, fault #5 is hard-linked to faults #4 and #6, connecting to both other faults at a near-perpendicular angle. The largest fault in the think-skinned fault population, fault #4, has a slight shift in strike direction to the south of the impact point of fault #5 (Figure 6.6). From this point and towards the southern tip of the fault, the strike direction almost exactly matches that of fault #5.

Of the thin-skinned fault population, only fault #1 intersect with the mapped top Shetland Group, if ever so modestly. The rest of the population is confined to the lower parts, and none penetrate very far below the point of intersection with the top Cook Formation (Table 6.1).

6.2.1 Vertical Displacement

The differences in vertical displacement for the four thick-skinned faults are made apparent when colour draping the fault surfaces with displacement values, as is presented in Figure 6.7. For the Tusse North fault segment, it is observed how displacement is diffusely spread across a larger vertical extent, where the maximum displacement achieved is ~800 m. Two centres of maximal displacement are observed in the Tusse South fault segment within the Sognefjord and Drake intervals, where each centre exhibits a displacement of ~900 m.

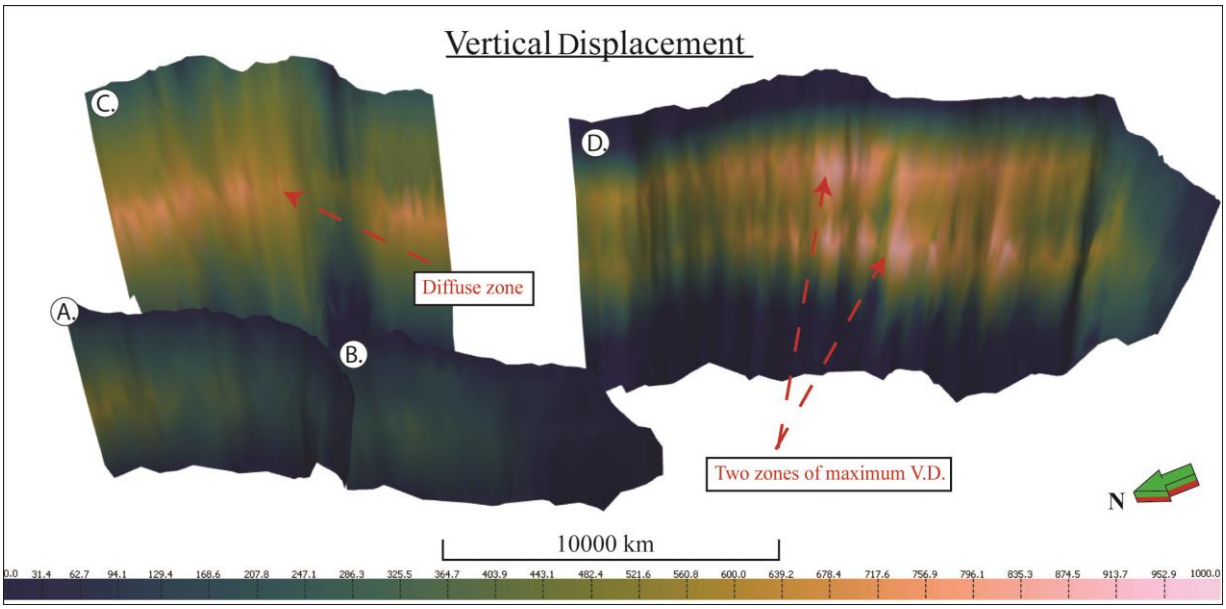

Figure 6.7: The four thick-skinned faults colour draped by their amount of vertical displacement (throw). The faults follow the nomenclature from Figure 5.3. The Colour scale is the same for all four. A vertical exaggeration of x3.5 is applied. Abbreviation: V.D – vertical displacement.

Lesser displacement is achieved in the Svartalv segments, with a slight increase towards the north, the maximum of which ranges around ~500 m. Svartalv South exhibit an overall displacement of less than 200 m.

All segments exhibit their displacement maxima as near-horizontal zones near their vertical centres (Figure 6.7).

6.2.2 Vertex Attributes

The data displayed in Table 6.1 show that the mapped part of the thick-skinned Tusse Fault is especially large and with a very high degree of vertical extent, from -789 to -5397 (North and South segments combined). This is significantly larger than the rest of the mapped fault population. The other thick-skinned fault, Svartalv, also exhibits values that exceed the thin-skinned population. The deepest 2nd-order fault is fault #4, which is also the largest in lateral extent by a substantial amount. It is noteworthy that only one single thin-skinned fault in the population intersects the top of the Shetland Group, namely fault #1 in the North, where the Shetland Group is at its shallowest level (well 31/5-2 intersects Shetland Gp at -1432 m, see Table 6.1).

Table 6.1: Vertex attribute data collected from the fault surfaces in Move, for all the faults mapped in this study. Note the severe strike deviation for fault #5. *****Vertical extent is calculated from the depth min/max values. **Lateral extent is measured for each fault at the Sognefjord Formation level.

Fault	Depth (m)		Extent (m)		Dip (°)			Strike (°N)		
	Min	Max	Vertical *	Lateral**	Min	Max	Mean	Min	Max	Mean
Svartalv North	-1296	-3284	1988	10300	4	82	61	161	267	209
Svartalv South	-1398	-3250	1852	8800	27	89	60	1	237	190
Tusse North	-789	-5183	4394	13900	6	75	50	112	248	189
Tusse South	-988	-5397	4409	29200	6	89	55	48	359	187
Fault #1	-1238	-3013	1775	9100	12	88	56	69	334	141
Fault #2	-1439	-2978	1539	8700	13	90	66	0	359	345
Fault #3	-1481	-3186	1705	8460	6	86	59	0	359	346
Fault #4	-1668	-3917	2249	18100	42	88	63	121	242	176
Fault #5	-1793	-3307	1514	3900	33	89	62	26	246	55
Fault #6	-1774	-3608	1834	4500	34	86	65	0	359	355

Rose diagrams of dip angle and strike directions for the entire fault population are presented in Figure 6.8. The fault population has some variance concerning dip angle, albeit most faults excepting Svartalv South and faults #4, 5 and 6 exhibit the entire range, 0-90° (Table 6.1). Despite this, the faults have a strong similarity of mean dip angles, where all faults range between 50-66° (Table 6.1, Figure 6.8a), and so is dominated by dip angles expected from a normal faulting regime (see chapter 3).

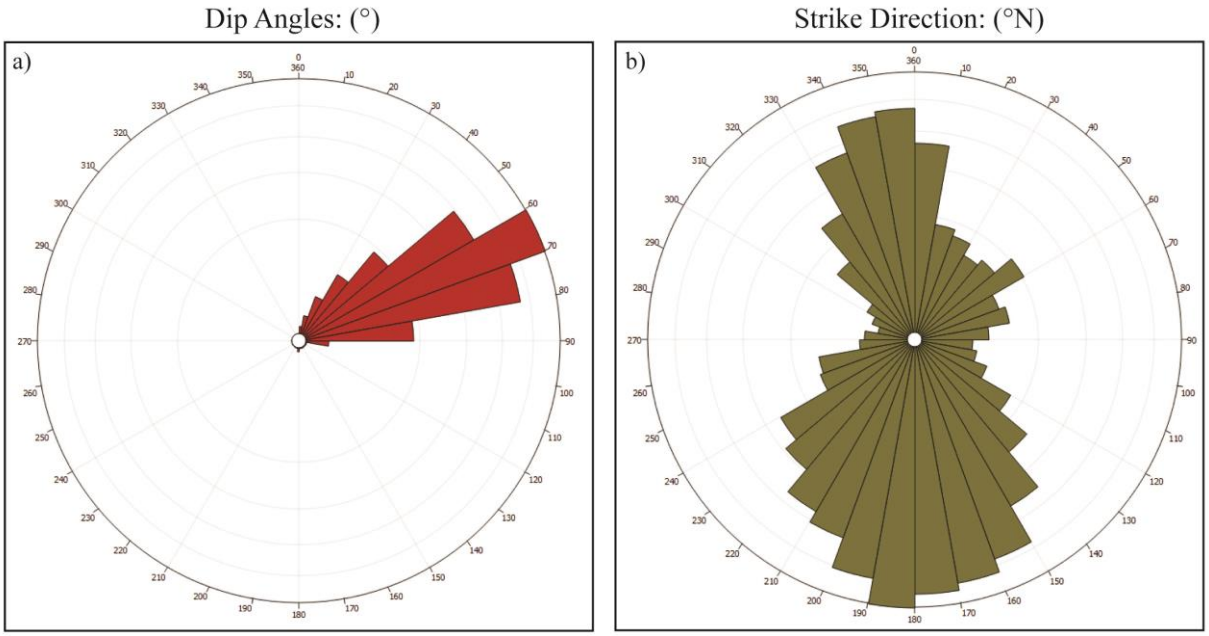

Figure 6.8: Rose diagrams of dip angles and strike directions for the entire fault populations. a) dip angles in degrees (0-90°), b) strike directions in azimuthal degrees. Note that the mean dip angle is presented as a black arrow.

In terms of strike direction, the fault population exhibit a more diverse range (Figure 6.8b). Nevertheless, the predominant strike direction is observed as N-S, with the population having a mean strike of ~220°N (Table 6.1). A pattern can be observed for the west- and east-dipping faults, where west-dipping faults averagely strike between ca. 180-200°N, and 345°N for the east-dipping, antithetic faults (Figure 6.8b). The only fault exhibiting a severe deviation in strike is fault #5, striking at 55°N and abutting into faults #4 and #6 at near-perpendicular angles (Table 6.1).

More vertex attributes from the analytical methods will be presented in the next subchapter.

6.3 Analytical Stress Results

Presented in the following subchapter are the results from the analytical methods employed in this study, as well as mappable vertex attributes such as dip angle. From the total of 75737 data points that were gathered, Kernel smoothing density (Ksd) plots were constructed for dip angle, slip tendency, dilation tendency, slip stability and fracture stability. Parameters used to perform the analyses are presented in subchapter 4.5. Analytical results from the slip tendency, dilation tendency and slip stability analysis for the Drake interval are presented in Appendix B. Table 6.2 presents a summary of dip values and the four analytical methods employed in this study. Note that all fault models have a maximum value of dip at 90°, which is unreasonably high. This is attributed to MOVE's Delaunay triangulation method, where an insignificant amount of triangles have been oriented with a 90° angle. However, this does not appear to have a pronounced effect on the mean dip angles, alas it has probably affected dilation tendency, in which both the minimum and maximum values are very low and high, respectively. While the mean values for dilation tendencies are rational, it is advised to inspect Figure 6.11 for a better representation of dilation tendencies.

Table 6.2: Summary of the vertex attributes generated when using the Stress Analysis tool in Move. The summary includes minimum, maximum and mean values for the five parameters. It is advised to view the minimum and maximum values in the case of dip and dilation tendency with some consideration.

Interval	Dip angle (°)			Slip Tendency			Dilation Tendency		
	Min	Max	Mean	Min	Max	Mean	Min	Max	Mean
Shetland	6.7	90.0	61.7	0.00	0.16	0.10	0.00	1.00	0.53
Sognefjord	16.3	90.0	63.5	0.00	0.46	0.33	0.00	1.00	0.70
Drake	10.0	90.0	64.7	0.00	0.44	0.31	0.00	0.99	0.72
Cook	3.8	90.0	67.6	0.00	0.51	0.36	0.00	0.99	0.76

Table 6.2: Continued. Slip and fracture stability values are given in MPa.

Interval	Slip Stability			Fracture Stability		
	Min	Max	Mean	Min	Max	Mean
Shetland	6.1	16.1	10.1	9.6	19.2	13.4
Sognefjord	4.5	28.8	8.4	12.6	33.8	18.0
Drake	0.2	28.5	4.5	2.5	29.0	6.8
Cook	1.8	39.7	5.3	10.1	46.3	13.1

6.3.1 Dip Angle Analysis

All mapped faults throughout the area are dominated by higher values of dip angle, as would be expected from a regime of normal faulting. Local variations of lower dip angles are seen in Figure 6.9a as bright beige spots that seem to concentrate in the uppermost parts of the faults, within the Shetland interval and above. From the Ksd plot in Figure 6.9b, this is visualized as the "leg" of lower dip values for Shetland in the lower-left part of the curve for Shetland.

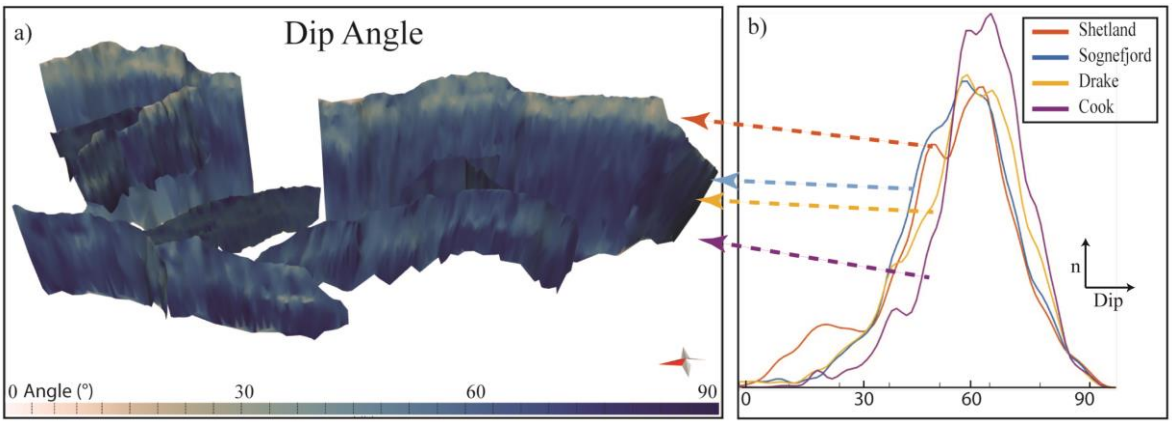

Figure 6.9: a) All faults colour draped with vertex attribute: dip angle. b) Kernel smoothing density plot of dip angle for the Shetland, Sognefjord, Drake and Cook intervals. n on the y-axis denotes the relative amount of data points.

Below the Shetland interval, a down-dip trend of slightly increasing dip angles is observed, down to the lowermost Cook interval, which exhibits both the lowest density of lower dip values and the highest density of high dip values, whereas the Drake and Sognefjord intervals fall somewhere in between. The Drake cap rock interval has dip angles that are strongly concentrated around 60-75º (Figure 6.9b).

It should be noted that dip angles ranging from 0-90º are present within all the intervals and almost all fault models (see Table 6.1). Since it is geologically unreasonable that a fault exhibits both vertical and horizontal faces, this feature is attributed to the Delaunay Triangulation method, where triangles along the fault models' edges sometimes appear warped or badly fitted together, especially at the bottom of the models.

6.3.2 Slip Tendency Analysis

To reiterate, the values of slip tendency (T_s) for a fault need to exceed the value of the coefficient of friction (μ) that the fault rocks exhibit for there to be any chance of reactivation by shear failure (see subchapter 3.4.1). The results from the slip tendency analysis is presented in Figure 6.10.

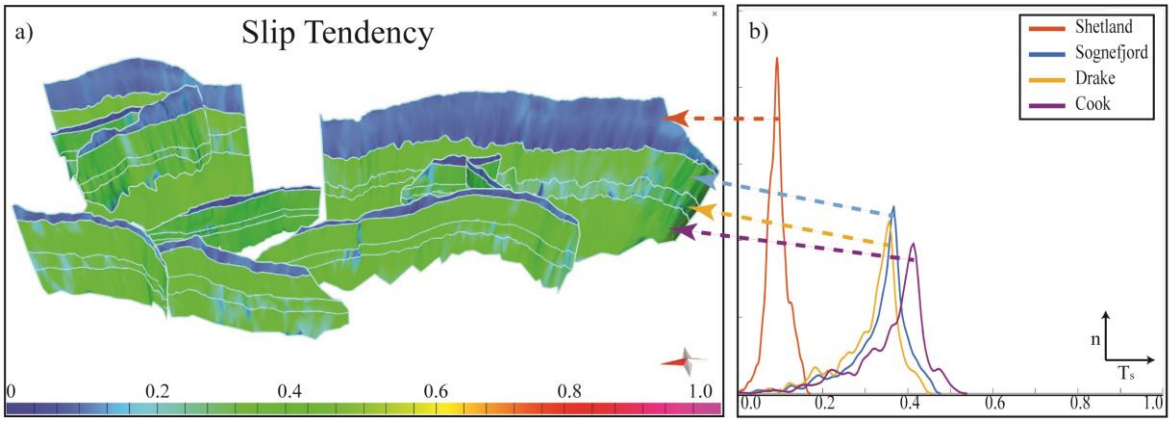

Figure 6.10: a) All faults colour draped with vertex attribute: slip tendency ratio. b) Kernel smoothing density of slip tendency values for the Shetland, Sognefjord, Drake and Cook intervals. n on the y-axis denotes the relative amount of data points.

Slip tendency fiercely follows the trend of dip angles in figure 6.9a, where the interval of lowest dip angles, Shetland, also exhibits the lowest and safest values of slip tendency (Figure 6.10). This is also manifested in the Ksd plot where the slip tendency values are seen to be strongly concentrated around 0.1 slip tendency (Figure 6.10b). Conversely, the other three intervals are very similar in exhibiting a slightly higher values, which are concentrated around 0.35-0.40. These values are still considered safe, as μ for all intervals exceed 0.45 (see Table 4.4). The only interval whose risk is within a ±0.10 range of slip tendency is the Drake cap rock interval, whose designated coefficient of friction is exactly 0.45.

The slip tendency analysis for the Drake interval shows that the interval is very monotonous across the entire study area. A vast abundance of slip tendency values ranging from 0.2-0.4 is observed as green colours in Figure 6.10a. No pronounced north/south, east/west or depth difference are present (Figure 6.10a). Very localized instances of reduced slip tendency, seen as blue areas, can be noted at some fault bends.

6.3.3 Dilation Tendency Analysis

To reiterate, any value of dilation tendency (T_d) that exceeds 0.8 passes the criteria for tensile failure, where a fault exhibiting $T_d = 1$ might fail with pure dilation (Ferrill et al., 2020). As with slip tendency, dilation tendency strongly follows the trend of dip angles in Figure 6.9. As expected, the more vertical fault segments exhibit the highest levels of dilation tendency. Hence, the Cook interval, having the highest values of dip, also has the highest values of dilation tendency (Figure 6.11). Conversely, the Shetland interval exhibits the lowest and safest values of dilation tendency. The Sognefjord and Drake intervals exhibit high values but are not as concentrated as that of the Cook interval (Figure 6.11b).

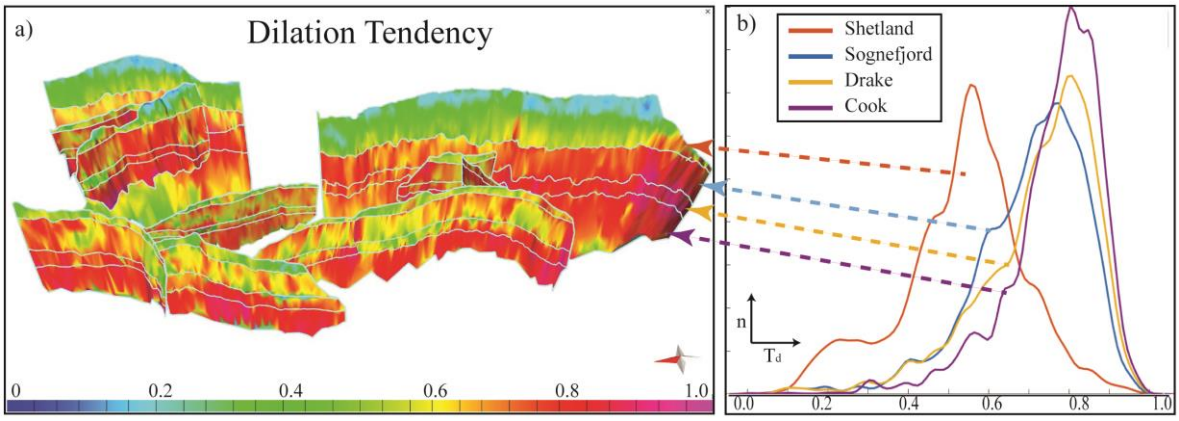

Figure 6.11: a) All faults colour draped with vertex attribute: dilation tendency ratio. b) Kernel smoothing density of dilation tendency values for the Shetland, Sognefjord, Drake and Cook intervals. n on the y-axis denotes the relative amount of data points.

In contrast to slip tendency, there is for the dilation tendency analysis several discernible disparities within the Drake interval. The highest values of dilation tendency (red-purple) are found at the fault tips of the southernmost faults, while the lowest values (blue-green) are concentrated towards the middle of the study area (Figure 6.11a). Faults exhibiting the largest areas of low dilation tendency are the ones in the centre, faults #3 and #4 (Figure 6.11a). By definition, values of $T_d \geq 0.8$ pass the criteria for tensile failure (Ferrill et al., 2020). Although almost the entire colour scale is represented within the Drake interval (Figure 6.11b), an abundance of values concentrates around 0.8±0.1, suggesting that the majority of the Drake interval fault segments pass the criteria for tensile failure.

6.3.4 Slip Stability Analysis

To reiterate, slip stability calculates the critical perturbation pressure (CPP), expressed as the amount of extra pore pressure (ΔP in MPa) needed to push a cohesionless fault into a critically stressed state. A fault segment exhibiting low slip stability is at a high risk of reactivation. Results from the slip stability analysis is presented in Figure 6.12.

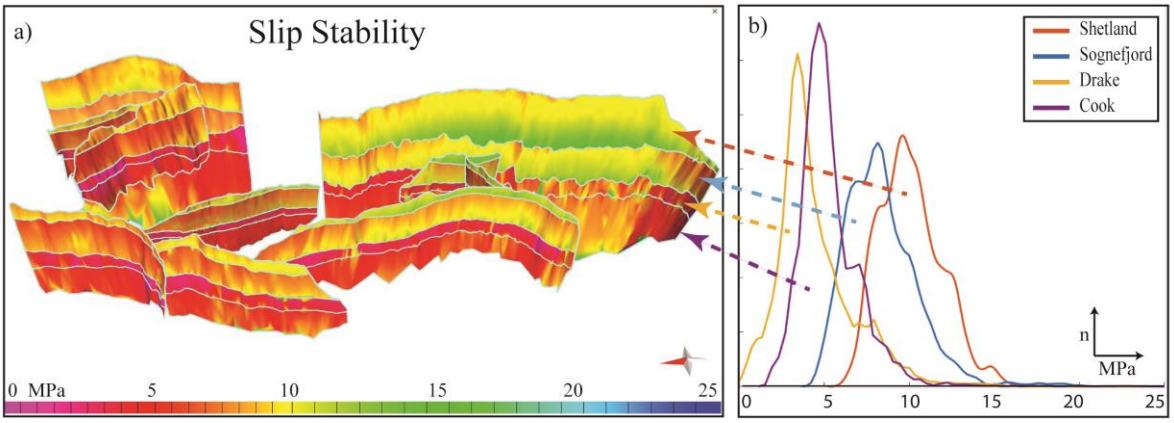

Figure 6.12: a) All faults colour draped with vertex attribute: slip stability. b) Kernel smoothing density of slip stability values for the Shetland, Sognefjord, Drake and Cook intervals. n on the y-axis denotes the relative amount of data points.

An abrupt shift from yellow-green on top to orange-red-purple colours between the Shetland and Sognefjord intervals and the deeper Dunlin Group is observed in Figure 6.12a. A N-S trend is also recognizable, where the northern fault segments exhibit a significantly higher risk of reactivation than the southern parts.

The lowest values of slip stability are encountered in the Drake cap rock interval, where local segments approach a critically stressed state (CPP = 0). The majority of faults in the Drake interval exhibit values of CPP ranging from 0.0-8.0 (purple-red), with an overweight towards the lower values. A north/south pattern is discernible where the southern part of the Tusse fault exhibit CPP >8.0, seen as yellow, orange, and green colours in Figure 6.12a. These areas slightly coincide with areas exhibiting higher values of dip, seen as darkest blue areas in Figure 6.9a, and areas where slip tendency is lowest in Figure 6.10a. The slip stability analysis reveals that considering the Drake fault segments as classic cohesionless faults denotes many fault segments as already being in or approaching a critically stressed state (Figure 6.12).

6.3.5 Fracture Stability Analysis

To reiterate, fracture stability only differs from slip stability by one factor: it allows consideration of faults with cohesion. The analysis was performed using the respective intervals' designated value for cohesion and angle of internal friction (see subchapter 4.5). Results from the fracture stability analysis is presented in Figure 6.13.

A more detailed fracture stability analysis specifically for the Drake interval is presented in the forthcoming Subchapter 6.4

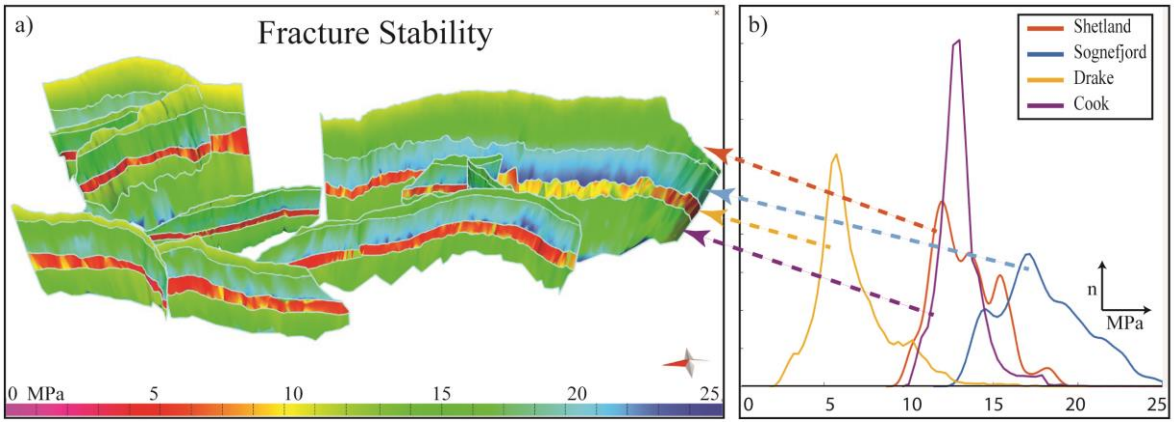

Figure 6.13: a) All faults colour draped with vertex attribute: fracture stability. b) Kernel smoothing density of fracture stability values for the Shetland, Sognefjord, Drake and Cook intervals. n on the y-axis denotes the relative amount of data points.

Any fault segment exhibiting values of fracture stability approaching zero is within risk of reactivation. When cohesion is considered, calculated CPP is changed significantly. The uppermost Shetland interval, having the lowest in-situ pore pressure and some cohesion, exhibits concentrated and safe values of fracture stability (Figure 6.13).

The more competent Cook and Sognefjord reservoir intervals also exhibit considerably higher and safer values of fracture stability compared to slip stability (Figure 6.13). Values of fracture stability for the deeper and weaker Drake cap rock interval are perilously low, being concentrated around 5 MPa (see chapter 4). This means that an increase of an additional 5 MPa pressure from CO_2 injection might push the fault segments within the Drake interval into a critical state.

6.4 Drake Interval: Stress Analysis

As previously stated, the intended scenario CO_2-injection of the Northern Lights project is to utilize Johansen and Cook as storage formations and Drake as the sealing cap rock formation (Gassnova, 2012; Thompson et al., 2022). Considering this, the following section focuses on the potential risk for fault reactivation in Drake Formation. Thus, far more time and emphasis have been allotted to the analysis of the Drake interval. More elaborate use of the fracture stability method in the Stress Analysis tool is presented in this subchapter. The Drake interval results from the slip tendency, dilation tendency and slip stability analyses are provided in Appendix B.

Considering the focus of this study, it is appropriate to repeat some of the Drake Formation's most significant lithological features:

- The Drake Formation is age-dated as between 174-168 Ma and has a thickness of 128 m in well 31/5-7 (Table 4.3).
- The Drake Formation has a significant south-ward dip (~2.6°), with an elevation ranging from -1800 m to -3400 m across the study area (Figure 6.1).
- All faults mapped in the study intersect the Drake Formation.
- Fault- and fault rock properties: SGR = +40%, μ = 0.45, φ = 24°, cohesion = 1.0 MPa, fault rock = clay smear (Table 4.4).
- In-situ stresses (in MPa): Pore pressure, PP = 25.0, σ_v = 51.2, σ_H =38.0, σ_h = 36.2 (Table 4.3, Thompson et al., 2022)
- Within the Drake formation, Thompson et al. (2022) report mineralogic constituents as ~70% clay (of which ~6% is smectite), ~16% quartz, ~2% carbonates and minor constituents of chlorite, muscovite, pyrite and calcite (see subchapter 4.5).
- 24666 vertex attribute data points were generated by the Move software for the Drake interval (Table 5.2).

6.4.1 Drake interval: Fracture Stability

Fracture stability analysis for the Drake interval is presented in Figure 6.14. Fracture stability differs from slip stability by allowing faults to have cohesive strength, and so this analysis was completed using the Drake interval's designated value of cohesion (C = 1.0 MPa) as described in chapter 4. A significant portion of the fault segments exhibit values of fracture stability that are approaching a critical condition, seen as purple and red colors in Figure 6.14. The lowest values are found underneath the Troll oil and gas fields, in the southernmost part of the Tusse North fault segment, northern tip of fault #4 and the entire fault #5.

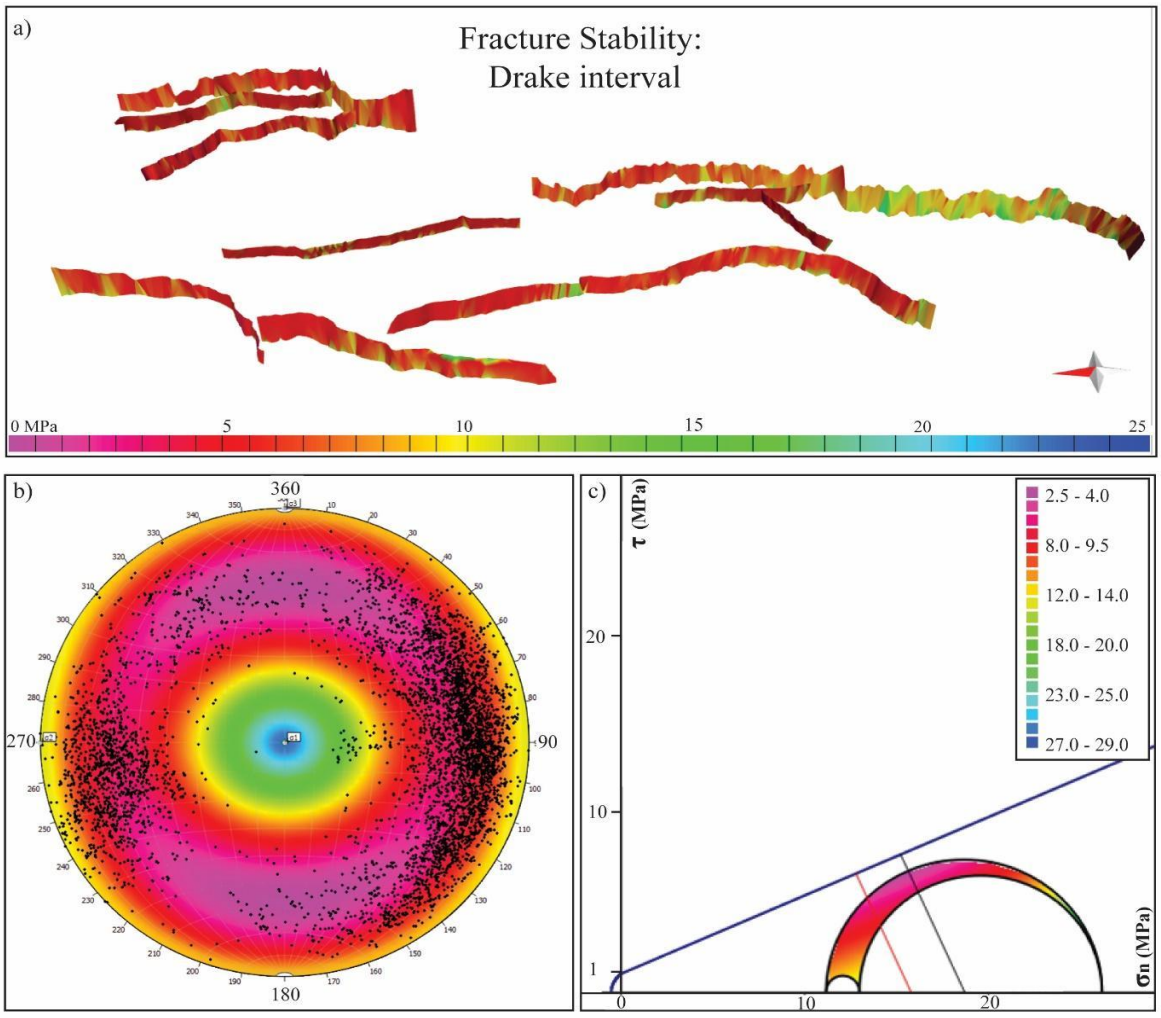

Figure 6.14: Fracture stability analysis of the Drake interval showcasing: a) all Drake interval fault segments, b) polar diagram of S_f with dip orientations displayed as black dots, c) Mohr-Coulomb diagram of the in-situ stresses acting on the fault surfaces. Note that the colour scale is different in a) than in b) and c) due to limitations in Move's Stress Analysis tool.

Very few dip values are within a CPP range between 12-20 MPa, most of which are found in the southern parts of Tusse South, seen as yellow and green areas in Figure 6.14a) and b). A few local variations of higher values are also observed as areas of yellow and green, possibly correlating with fault bends or corrugations in the fault model. The Mohr diagram in Figure 6.14c) reveals how close some of the more exposed segments are to being in a critically stressed state, even when considering the fault rocks having some cohesive strength.

6.4.2 Drake interval: Sensitivity Analysis

A sensitivity analysis was engaged to compensate for the risk of fault plane heterogeneity and to challenge the assumptions made in this study with regard to fault rock properties (see subchapter 4.5.2). As previously stated, the most significant analysis for this study is the fracture stability, which heavily relies on the cohesion parameter. As such, the fracture stability analysis was performed with a range of different cohesions: 0.0, 0.5, 1.0 (the initial value), 1.5, 2.0 and 4.0 MPa. The results are presented in Table 6.3 and Figure 6.15. Note that a fracture stability analysis with C = 0.0 MPa is identical to the slip stability analysis (see Appendix B.3).

Table 6.3: Mean and standard deviation dip values and critical perturbation pressure, with min/max, for the four intervals. For all fracture stability experiments with cohesion (C) in the Drake interval, the values dip matches that of the initial Drake interval. Note that "Drake C= 1.0" is the same as the initial Drake but reiterated to display decreasing values of fracture stability.

Formation	Dip (°)		Critical perturbation pressure, CPP (MPa)			
	Mean	Std.	Mean	Std.	Min	Max
Shetland	61.71	13.07	13.36	1.89	9.61	19.24
Sognefjord	63.52	11.16	18.03	2.77	12.60	33.81
Drake	64.68	11.57	6.75	2.28	2.48	28.97
Cook	67.57	9.77	13.09	1.65	10.08	46.31
Entire fault population	64.37	11.39	12.81	2.15	8.69	32.08
Drake C= 0.0			4.51	2.30	0.24	28.47
Drake C= 0.5			5.63	2.29	1.36	28.72
Drake C= 1.0			6.75	2.28	2.48	28.97
Drake C= 1.5			7.87	2.25	3.61	29.22
Drake C= 2.0			8.97	2.21	4.73	29.47
Drake C= 4.0			13.10	1.80	9.20	30.50

The sensitivity analysis in Figure 6.15 reveals a pattern with an easily observed effect: adding cohesion significantly adds to the fault tolerance (Table 6.3, Figure 6.15). Interestingly, for every 0.5 MPa of added cohesion, the calculated CPP increases by approximately 1.12 MPa. This is manifested as a progressive removal of purple-red colours in favour of orange-yellow-green colouration in Figures 6.15a-e, as well as the increasing distance between the failure envelope and the Mohr circle. Note that the initial condition is not included in Figure 6.15. It is made apparent that a small variation in cohesion results in very different results in terms of fracture stability.

There is an observable difference between the north and the south, best seen if comparing Figures 6.15b and 6.15c, where fault segments in the south are exhibiting an increased effect of the added cohesion. Especially, the Tusse South fault segment exhibit values ranging between 10-15 MPa CPP when faults are considered with 1.5 MPa cohesion, compared to the much lower range of 5-15 MPa CPP when considered with 0.5 MPa cohesion. In this case, the highest values only appear very locally, seemingly in fault bends or corrugations.

Note that when faults are considered with 2.0 MPa, and especially with 4.0 MPa cohesion, very few areas remain that exhibit a tolerance below 5.0 and 10.0 MPa CPP, respectively (Table 6.3, Figures 6.15d,e). Indeed, when considering faults with 2.0 and 4.0 MPa cohesion the mean CPP is remarkably high, at ~9.0 MPa and ~13.0 MPa, respectively (Table 6.3).

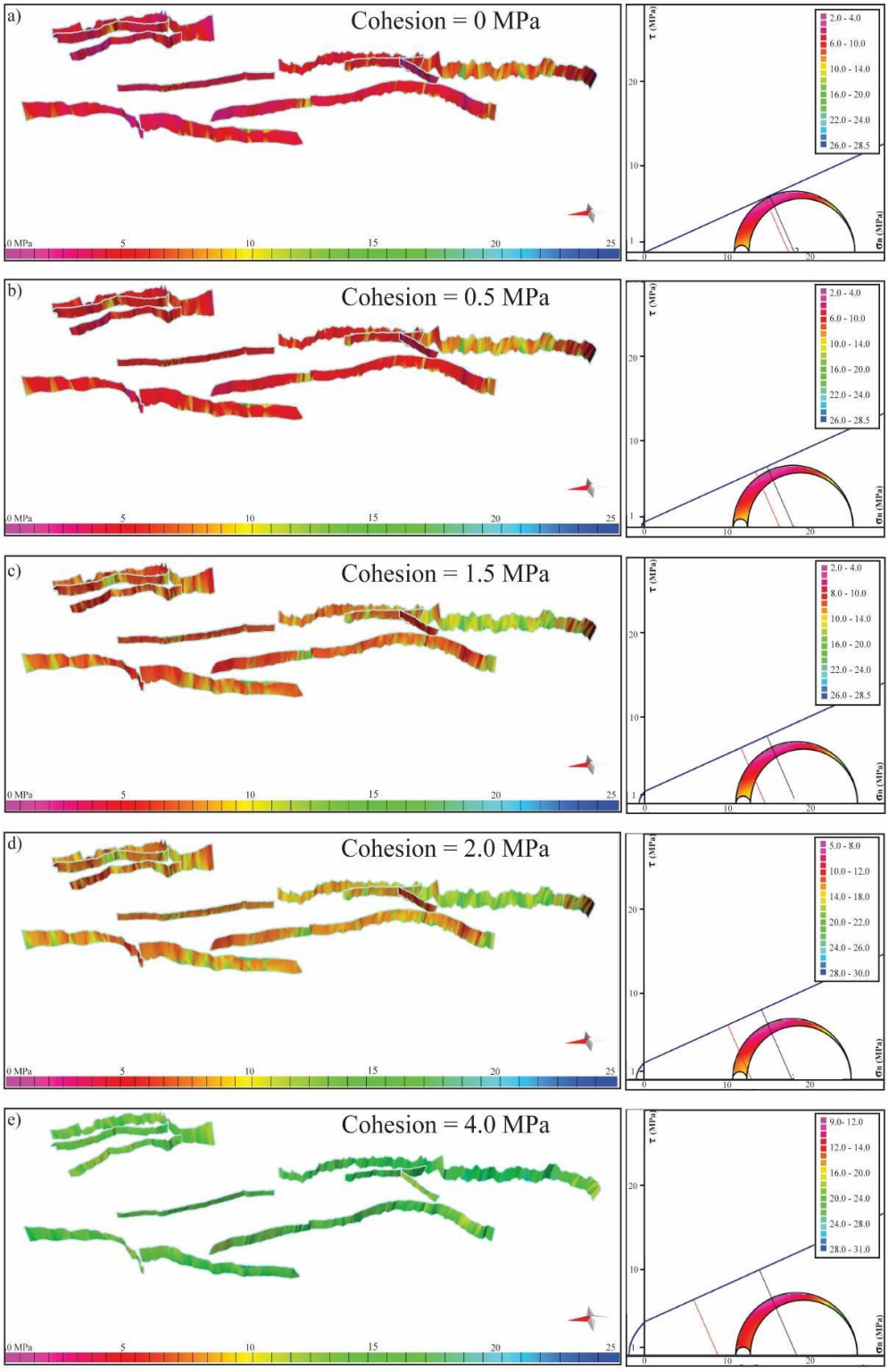

Figure 6.15: Fracture stability analysis using five additional values for cohesion (in MPa): a) 0, b) 0.5, c) 1.5, d) 2.0 and e) 4.0 (the initial 1.0 MPa condition is exempted from this figure). The figure display fault surfaces colour draped with fracture stability values and Mohr circles of the stresses acting on the fault planes. Note that the colour scale is the same for all the fault surfaces, but different for all the Mohr circles due to limitations within the Move Stress Analysis tool. Also, note that the difference in the failure envelope is because of increasing cohesive strength.

7 Discussion

In the previous chapter, the structural characterization and morphology of faults and surfaces were presented, as well as results from the analytical analyses. Due to the Drake formation being the targeted cap rock for CO_2 injection, the focus of the results and analyses was centred on the Drake interval. In this chapter, these results are used to discuss the likelihood of faults within the Aurora Area to be reactivated by an increase in pressure, which is an implication that is crucial to assess when engaging in CO_2 storage. Links between critical perturbation pressure, failure mode, fault rock composition, fault dip angle, strike orientation, and in-situ pressures are investigated. Areas of high risk of reactivation are detected, highlighted and discussed with regard to previously suggested storage complexes by Holden (2021).

To the author's knowledge, no fault reactivation potential has previously been investigated or calculated in areas within the Aurora Exploration License (EL001). However, the neighbouring Smeaheia area, accommodating the potential Alpha, Beta and Gamma CO_2-storage sites, was investigated by Mulrooney et al. (2022) using the same techniques as applied in this study, thus allowing for comparison of results.

7.1 The Faults Within the Aurora Area

In this study, ten fault segments were mapped and subjected to analytical methods to determine their likelihood of reactivation and likely mode of failure (see Figure 6.4). The size and vertical extent of the faults investigated in this study allow for a separation into two fault populations (see subchapter 6.2), as previously determined by several authors: i) a population comprising N-S striking, thick-skinned faults, termed as 1st-order, ii) a second population comprising NW-SW striking, thin-skinned faults, termed as 2nd-order (Duffy et al., 2015; Holden, 2021; Whipp et al., 2014). It is shown herein that there is an abundance of faults in the northern part of the study area compared to the southern parts (Figure 5.3b). However, some of the largest faults are found in the south, i.e., Tusse South and fault #4.

The fault interaction styles between these non-colinear fault populations are determined to vary, but the majority of the 2nd-order faults are said to be isolated or abutted against 1st-order faults (Duffy et al., 2015). In this study, the faults are mapped as close together as possible, but

none were considered hard-linked during the modelling phase of the workflow. However, previous studies exploring fault interaction styles have mapped hard linkage of for example fault #4 abutting into the Svartalv fault (e.g. Duffy et al., 2015; Holden, 2021). The fault models made in this study promote that fault #5 is hard-linked to faults #4 and #6 since it connects to both other faults at a near-perpendicular angle. The largest fault in the think-skinned fault population, fault #4, has a slight shift in strike direction to the south of the branch line of fault #5 (Figure 5.3b and Figure 6.6). From this point and towards the southern tip of the fault, the strike direction almost exactly matches that of fault #5, indicating fault interaction by a transfer of local strain that altered the strike.

Fault growth can be determined by analysing vertical displacement, herein produced for the thick-skinned faults only. Cut-off lines for the thin-skinned faults were created exclusively in order to split them into intervals, as very little vertical displacement existed. Modelling of the Tusse South fault segment display two horizontal zones of maximum displacement (D. in Figure 6.2). These zones are positioned within the Drake and Sognefjord intervals and, despite not signifying nucleation timing, the zones nevertheless indicate a time of heightened fault activity during the Early Jurassic and Late Jurassic, respectively. In a mechanically layered section such as in this study, the strength of a throughgoing fault in terms of coefficient of friction and cohesion varies greatly in response to the host rock. Fault strength is greatest where competent layers are juxtaposed, and as displacement increases the result is a progressive juxtaposition of competent rocks against mechanically weaker rocks (Ferrill et al., 2017). Within such sections, reactivation by fault slip would inevitably localize in the weaker sequences. As displacement continues the intervening weak layers become smeared and form a weak core between previously juxtaposed competent layers in a process that Ferrill et al. (2017) argues tend to weaken the overall fault strength. Thus a scenario is viable for the Tusse South fault segment, where the competent Sognefjord interval sandstones in the hanging wall are progressively juxtaposed against the weaker clays of the Drake Formation. Following Ferrill et al.'s (2017) arguments, this would create a fault weakness at the level of the Drake Formation in the footwall that reactivated at a later stage in the faults evolution, resulting in two separate foci of displacement maximum.

Tusse North exhibit a larger, more diffuse, central zone of maximum displacement within the middle Sognefjord interval, interpreted as an amalgamation of the two zones within Tusse South (C. in Figure 6.2). This is expected as this northern fault segment is spatially situated closer to the centre of the entire Tusse fault's length. For a normal fault with isolated tips, the

displacement is generally greatest at the centre of the fault and decreases to zero towards the fault tips (Rotevatn et al., 2019; Watterson, 1986). Considering vertical displacement of the Svartalv fault segments, a lesser maximum is observed in the centre of Svartalv North, in the same interval as Tusse North (A. and B. in Figure 6.2). The consideration of fault growth and interaction styles has minimal bearing on current-day fault reactivation analysis. This subject is hence not discussed any further.

Four of the fault segments mapped in this study fall into the 1st-order population. Namely, the Svartalv North, Svartalv South, Tusse North and Tusse South. The faults were not mapped to their full vertical extent to save time and data handling issues. This was an advised choice that did not impede or affect the analytical methods applied. These faults have been previously determined to be nucleated during Rift Phase 1 within Permo-Triassic successions, with reactivation occurring during Rift Phase 2 (Holden, 2021; Whipp et al., 2014).

The remaining six faults were recognized as 2nd-order faults and given arbitrary names loosely based on their spatial location. The population of 2nd-order faults, #1-6, were picked to their full lateral and vertical extent within the space of the GN10M1 3D seismic survey. Some of these faults have previously been investigated concerning fault activity timing, growth, and interaction styles, and have been determined to have been restricted to post-Triassic to Cretaceous successions (e.g. Duffy et al., 2015; Whipp et al., 2014). Most likely their growth was initiated in the inter-rift phase and Rift Phase 2 (Middle Jurassic to Cretaceous) and exhibited synchronous growth with the 1st-order faults in the Late Jurassic (Holden, 2021; Whipp et al., 2014). One might also consider fault initiation and growth not in terms of timing, as has been previously determined, but in terms of failure modes and fracture mechanics. Experiments have demonstrated that strain accumulated from tectonic activity in mechanically layered strata will cause rupture and faulting in brittle layers first, as ductile layers can accommodate larger amounts of strain prior to faulting (e.g. Ferrill et al., 2017, and references therein). Because mechanical properties are mainly controlled by mineralogy, porosity and texture, it is reasonable to assign sandstones such as the ones within the Sognefjord interval a brittle, or competent classification, given its lithology and cohesive strength (subchapter 4.5.2). Ductile layers, such as clay-rich shales, is a classification designated to the Draupne Formation, overlying the Sognefjord Formation, or indeed the underlying Drake Formation, given their high clay content (see subchapters 2.2.3 and 4.5). Given this litho-structural subdivision, faults would initiate within the Upper Jurassic Sognefjord Formation, or similarly positioned sandstones within the region, before driving displacement into the less competent surrounding

shales, where fault-tips may get arrested and thus exhibit limited throw. This reasoning also explains why the 2nd-order faults are found within post-Triassic to Cretaceous successions.

As shown in Figures 6.5, 6.6 and Table 6.1, there are significant size differences between this study's fault models of the 1st- and 2nd-order populations, both in vertical and lateral extent. The depth of penetration is much deeper for the thick-skinned faults, as shown in previous research where they are mapped as propagating up from the basement (e.g. Duffy et al., 2015). They also propagate further up-dip than the thick-skinned populations, the 2nd-order faults are generally found to not propagate up past ~1440 m, which is a depth penetrating the Upper Cretaceous Shetland interval only in wells 31/5-7 and 31/8-1 (see Table 4.2). The only exception is fault #1, whose fault tip is observed at -1238 m, and this depth only intersects the Shetland interval in the north (Table 6.1). Observations herein support the claims that this secondary population nucleated in the Lower Cretaceous, or at least the middle Upper Cretaceous as was determined by Whipp et al. (2014) and Duffy et al. (2015).

Moreover, there is also a large difference in terms of lateral extent between the two populations, where the 2nd-order fault segments mapped in this study generally are traceable to lengths shorter than 10 km at the Sognefjord Formation level. One exception is the southern fault #4, whose length at the Sognefjord Formation level was found to be 18.1 km. Table 6.1 reveal differences even within the 2nd-order population, as the southern faults #5 and #6 were found to be ~4.2±0.3 km long, and northern faults #1, #2 and #3 were found to be ~8.8±0.3 km long. Interestingly, the spatial location of the largest fault #4 and the smallest faults #5 and #6 coincides with the scarcity of faults in the southern parts of the study area, in contrast to the aforementioned abundance in the north.

7.1.1 Variations in Fault Dip

Investigation of the ten faults in the study area reveals numerous instances of internal changes in dip angles within the fault segments intersecting the four intervals (Figures 6.9, 7.1 and Table 6.1). This characteristic is prominent for the thick-skinned faults, but not unique to them, as any fault that cut mechanically layered strata commonly exhibit dip variations related to the mechanical properties of the strata (e.g. Childs et al., 1996; Ferrill et al., 2017). Consequently, it is rather common that normal faults in stratified rocks exhibit dip variations, a feature that is abundantly clear within the Shetland interval, suggesting that the lithological properties therein

differ from that of the other intervals. Most variations in normal fault dip are caused by either differential compaction of sedimentary layers, active fault deformation style (slip or shear), linkage of originally vertical fault segments or simply because angles during fault initiation was controlled by rock properties or effective stresses, at the time of failure, that has since changed (see Chapter 3.1, Childs et al., 1996; Ferrill et al., 2017). As neither the Shetland interval nor dip variations were the focus of this study, this subject was not pursued further.

Because dip variations were found within the Shetland interval, which is considered as a tertiary cap rock, one might expect a similar occurrence of dip variations within the Drake interval, as it is considered the primary cap rock. Only one such instance of significant dip variation was found within the study area, occurring immediately after the fault trace enters the top of the Drake Formation, as can be seen on Tusse South in Figure (Figure 7.1).

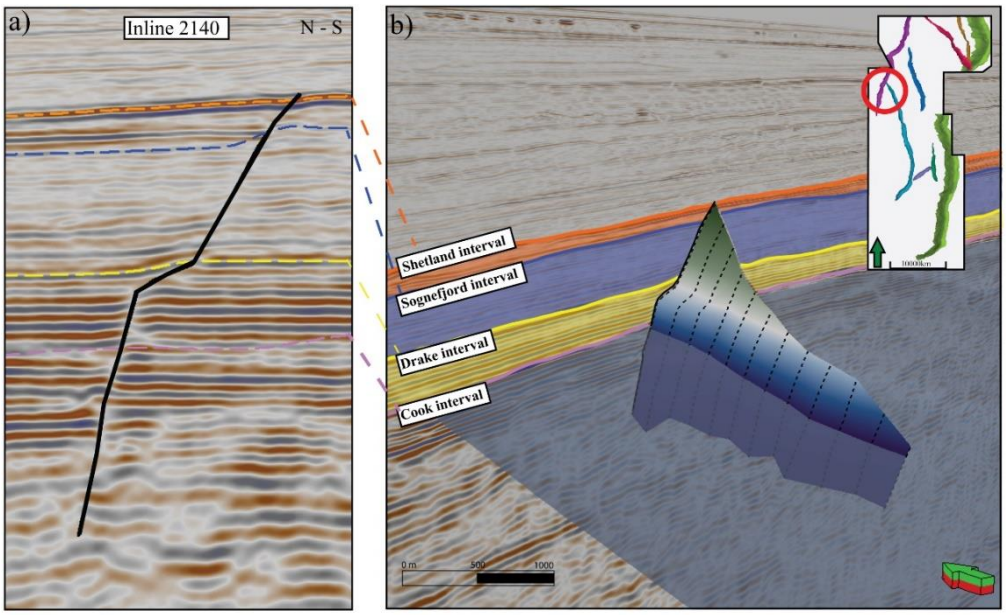

Figure 7.1: a) Cross-section of Inline 2140. b) 3D view of the Tusse South fault surface, showing the one instance of significant dip variation across the Drake Formation. The horizon surface seen in b) is the top Cook Formation. Note that very little displacement is seen at the fault tip of Tusse South and that the surfaces displayed are significantly smoothed.

This result is not repeated beyond the Tusse South segment except for very small variations in the middle of faults #1 and #4, and no displacement variation is observed to be associated with the change in dip (Figures 6.9 and 7.1). It is plausible that in the case of the Drake interval, the likely responsible event is a linkage between two near-vertical fault segments. It is well known that extension causes faults to rotate to progressively gentler dip angles, and so bedding angles

and pre-existing faults might become unsuitably oriented for slip, at which point the creation of a new fault surface is required to accommodate strain. The reactivation of such new faults might cause them to propagate and connect to faults across strata (Ferrill et al., 2017). That this occurrence of local dip variation was observed only once within the Drake interval suggests that differences in composition and geomechanical status to the surrounding layers had no great impact on the position of the dip variation, but rather the result of two fault segments being linked by a third.

7.2 Fault Reactivation Potential in the Aurora Area

A regional investigation of stress conditions and fault reactivation potential is herein discussed by considering the entire study area and the four chosen intervals within it. In chapter 6, it is shown how the Drake interval is in stark contrast to the other intervals in terms of tolerance to increasing pressures, and hence will be emphasized in the forthcoming subchapter 7.3.

Previous research by Thompson et al. (2022) determines that the entire study area is of a relaxed normal faulting regime in a state of tectonic quiescence (see subchapter 4.5.1). The maximal principal stress (σ_1) is vertical, produced by the weight of the overburden and affecting the faults at a 90° angle from above. The maximum horizontal stress (σ_2) impacts the fault surfaces from 90°N and the minimal (σ_3) from 180°N. Previous research has shown that slip and dilation tendency is strongly influenced by the orientation of the fault relative to the principal stresses and their magnitude (Miocic et al., 2014; Streit & Hillis, 2004). In addition to the in-situ stresses, the orientation of a fault's strike significantly alters the outcome of the reactivation analysis. The same is true for dip, the angle of which particularly affects the magnitude of the vertical pressure (σ_v) that the fault segment experiences. It is an important reminder that whether a fault actually reactivates by dilation or shear mainly depends upon the fault rock's inherent cohesive strength and coefficient of friction.

7.2.1 Slip and Dilation Tendency vs. Strike Direction

Out of the ten faults mapped in this study, nine of them exhibit a mean strike direction at a near-perpendicular angle to the maximum horizontal stress orientation (σ_H = 90°N), with strike directions of N-S or NW-SE (Tables 4.1 and 6.1). This categorically designates them as

belonging to either of the two fault populations described by previous research (e.g. Holden, 2021; Whipp et al., 2014). Notable deviations from the general strike direction are observed as westward striking jogs at the fault tips of both Tusse South and Svartalv North (see Figure 5.3). Ferrill et al. (2020) argue that tensile and hybrid failure prevails in conditions where effective σ_3 acts in a tensile manner, as would be the case in E-W striking, northwards dipping fault segments such as the aforementioned jogs. Both of which are identified as areas of high risk of reactivation in subchapter 7.3.

Only the smallest fault in the mapped population, fault #5, exhibit a significantly different strike direction (55°N); an oblique angle to σ_H (Table 6.1). This fault segment, which abuts against both faults #4 and #6 (see above), provides an opportunity to investigate how the in-situ stresses in the area affect faults with a strike and dip orientations that are atypical to the northern North Sea. It can be observed in Figure 6.11a that fault #5 exhibits high values of dilation tendency compared to its neighbouring faults. Ferrill et al. (2020) argue that compactive shear and compactive failure occur in conditions where σ_3 is compressive. This would be the case for a ~W-E striking, southwards dipping fault, such as fault #5. Ferrill et al. (2020) advocate that failure surfaces that strike normal to σ_3, as is the case in both these scenarios, have a dilation tendency at nearly 1, and indeed fault #5 is identified as a fault with very low tolerance to increases in pressure in subchapter 7.3. Because of the faults location down-dip of the 31/5-7 injection well, it was not investigated further in this study in terms of strike deviation. However, surfaces with high dilation tendency might open Mode I fractures, and so create conduits for fluids, the influence of strike orientation in relation to in-situ stresses on fault reactivation potential is deserving of further research.

7.2.2 Slip and Dilation Tendency vs. Dip Angle

Despite Thompson et al. (2022) labelling the Aurora area as a relaxed region in terms of stress, the stresses at the depth of the investigated successions in this study can be said to be of moderate magnitude, where weak normal stresses would occur on near-vertical faults (A. Braathen, personal communication). Results herein show that the study area is dominated by the higher dip angles, which increases down-dip (Figure 7.2). A classic view is that steeper fault segments occur in competent sandstones and limestones, whereas more gently dipping segments occur within weaker shales (e.g. Wallace, 1861). This view is not quite true for this

part of the Horda Platform, as data in this study reveal a consistent trend of down-dip increase in dip angles (Table 6.2). This trend is probably a consequence of increasing sedimentary compaction with burial depth, as the porosity, density, permeability and indeed shear strength of sediments are observed to increase with compaction, thus resulting in a steeper dip (Nooraiepour et al., 2017). In this study, the lowest dip angles are concentrated within the Shetland cap rock interval, as seen in Table 6.2 and Figure 7.2.

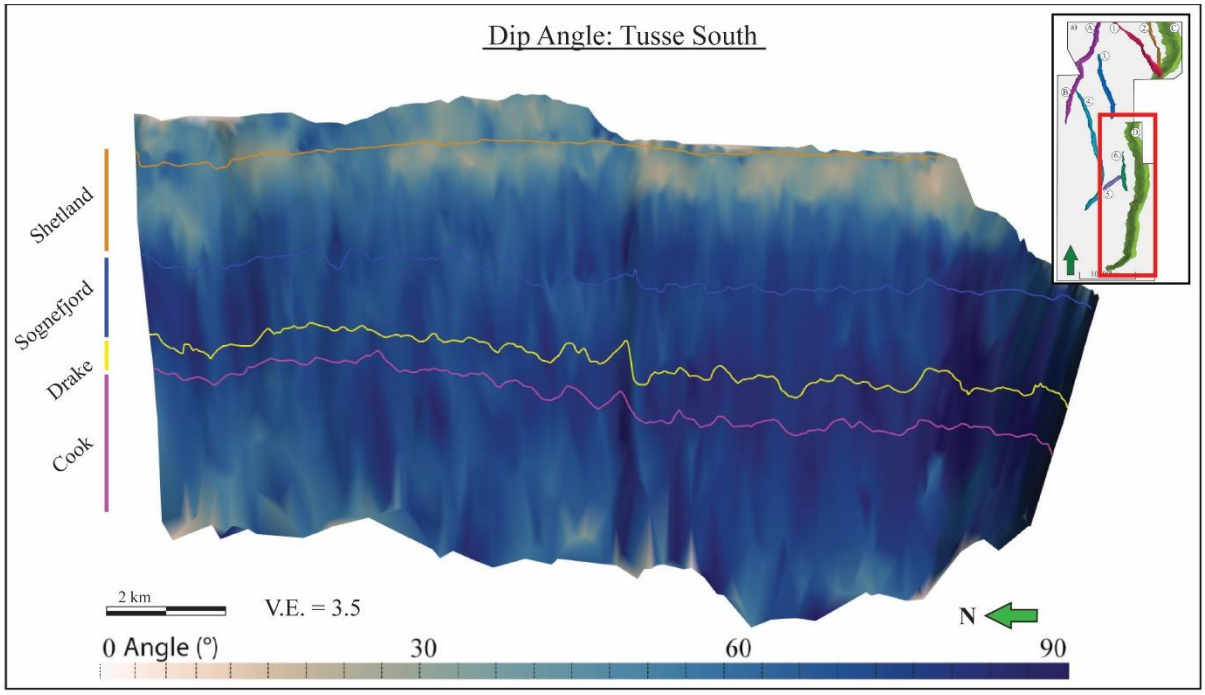

Figure 7.2: Example of the dominant dip angles, here within Tusse South. The figure is a magnified version of figure 6.9. Note that the lowest dip values are within the Shetland interval and above. Colours are slightly exaggerated to display contrasts.

Previous research on the Horda Platform by Mulrooney et al. (2022) found a strong relationship between dip, slip and dilation tendency, and points out that shallower fault dips often are associated with fine-grained sediments, which is the case for their Smeaheia faults and indeed much of the Cretaceous sediments of the northern North Sea. This includes the Shetland interval (see Subchapter 2.2.3, Deegan, 1977; Lepercq & Gaulier, 1996).

Because it is the uppermost interval mapped in this study, the pressure acting on the sediments in the Shetland interval is minute compared to the lower successions, as is documented by Thompson et al. (2022) when resolving pressures from well 31/5-7 (see Table 4.1). Therefore,

it is reasonable to assume that compaction of the Shetland interval deviates from that of underlying successions and that Shetland is of lesser competence than the others, thus creating a surface through which more gently dipping shear failure is possible (see Nooraiepour et al., 2017)**.** This effect might also be aided by the significant amount of weak mudrock and shale constituents in the Shetland interval (see subchapter 2.2.3). Thus, it is reasonable to assume that the low values of dip angle in the Shetland interval are not due to differences in fault deformation style or lithology, but rather because it was controlled by reduced compaction. Another possibility is that the effective stresses at the time of failure acted differently than at present time and that this favoured initiation of more gently dipping faults. However, this is speculative. Additionally, because only the 1st-order faults and fault #1 actually penetrates the Shetland interval, it is reasonable to assume that the low fault dip within Shetland is not due to the linkage of previously vertical segments.

Considering fault reactivation within the Shetland interval, Ferrill et al. (2017) advocate that any kind of slip initiation on a low-angle fault in a normal faulting regime (where the maximum stress (σ_V) is produced by the overburden), is highly improbable due to the high resolved normal stress mechanically preventing slip. In such a case where surfaces are near-normal to σ_1, the dilation tendency would be 0 and the resolved shear stress would be negligible (Ferrill et al., 2017). By this reasoning, it is not mechanically viable for reactivation to occur in the more gently dipping fault segments of the Shetland interval. Thus, it is concluded that fault reactivation in the Shetland interval is highly unlikely. Furthermore, within the study area, it is the Shetland interval that exhibits by far the lowest values of slip tendency (Figure 6.10). For the Shetland interval, values strongly concentrate around 0.1±0.05 suggesting the fault rocks within the interval would need to have an irrationally low value of the coefficient of friction for reactivation of slip to actually occur. While some lithologies enriched by smectite could exhibit coefficients of friction as low as 0.1±0.05 (Ferrill et al., 2017; Saffer & Marone, 2003), such constituents are not reported within the Shetland Group (Deegan, 1977). The same can be seen for dilation tendency, where again the Shetland interval exhibit distinctly lower values than the underlying intervals. This is presented in Figure 7.3a, where the plot for the Shetland interval deviates from the other three intervals in Figure 7.3b,c,d. The slip vs dilation tendency plot in Figure 7.3a shows that the interval exhibit values that fall under no clear category of failure mode. This suggests that in a scenario where the faults within Shetland interval reactivate, it would be by neither slip nor dilation, but rather as a mix between Mode IV and V, a mode between compactive shear and compactive failure (Figure 7.3a).

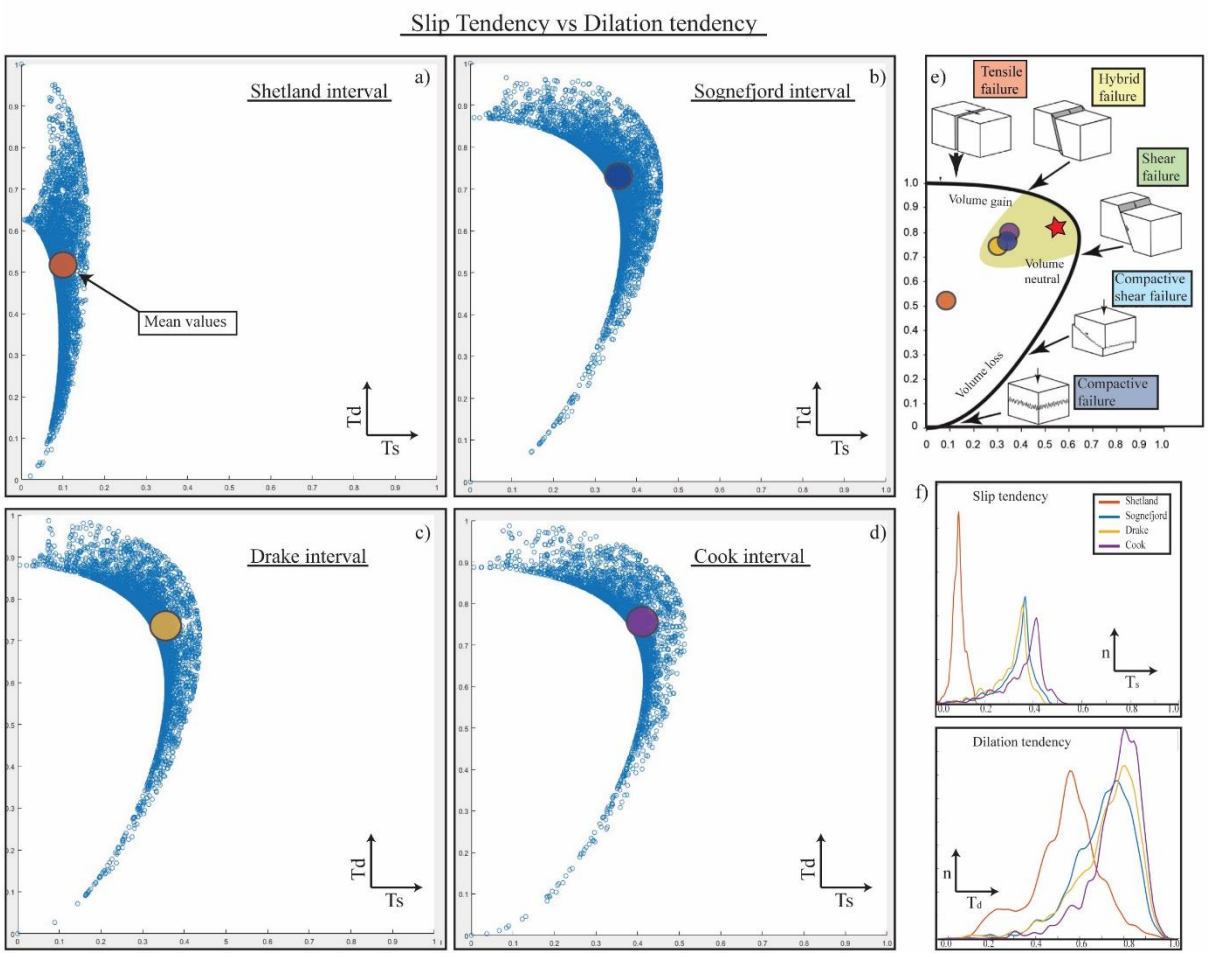

Figure 7.3: Slip tendency vs dilation tendency plots with vertex attribute data points generated by the Stress Analysis tool in Move. a-d) Plots for the respective intervals. The coloured dots within the plots represent mean values for each interval, which can be seen as peaks in the Ksd plots f). e) inset from Figure 3.3b, with added coloured dots of mean values. The red star in the yellow area signifies where the mode of failure is a mix between hybrid and shear. f) insets from Figures 6.10b and 6.11b. Abbreviations: T_s = Slip tendency, T_d = Dilation tendency.

The more steeply dipping intervals underlying the Shetland interval exhibit far greater values of dilation tendency. This suggest that if fault reactivation were to occur in the Shetland interval, reactivation by pre-eminently dilation would occur in the down-dip sections. This is in accordance with Ferril et al. (2014), who shows that slip along gently dipping fault segments could result in dilation of underlying, more steeply dipping fault segments.

As stated, it is implausible that slip occurs on low-angle faults. However, this would not be the case considering high-angle faults, where slipping is mechanically achievable. The Drake interval exhibits higher values of dip than the overlying intervals, with correspondingly high values of dilation tendency, with lower values only appearing locally on e.g., faults #1 and #4

in Figure 6.11. An abundance of dilation tendencies concentrated around 0.8±0.1 in Figure 6.11b, suggest that the majority of the Drake interval fault segments pass the criteria for tensile failure. Furthermore, slip tendency, which is also heavily dependent on dip angles, is considerably monotonous in the Drake interval throughout the study area. Slip tendency values for the Drake interval, as displayed by the Ksd curve in Figure 6.10b, strongly concentrate around ~0.38. This approaches a critical state for the Drake interval, as its designated value of the coefficient of friction was 0.45 (Figure 6.10, Table 4.2). Considering these results from the slip tendency analysis, the Drake interval is the interval that has the highest likelihood of reactivating by slip. The occurrence high slip and dilation tendency suggests that if fault surfaces within the Drake interval were to reactivate, they would do so in a mix between Mode II and III, a hybrid-to-shear-failure mode (Figure 7.3c,e).

The Cook interval, having the steepest dip (see Table 6.2) and underlying the Drake interval whose slip tendency values are very high, exhibit the highest values of dilation tendency measured in this study (Figure 6.11b). While it is expected that very high dip values result in high dilation tendency, it also coincides with Ferril et al.'s (2014) findings that more gently slipping faults segments (as in the Drake Formation) result in increased dilation tendency of underlying, steeply dipping fault segments.

It would be expected for relatively massive strata, like the competent Cook and Sognefjord interval sandstones, to fail with a consistent failure angle (Ferrill et al., 2017). Consistency of dip angles can be observed from the Ksd curve in Figure 6.10b, where the curves for the Cook and Sognefjord intervals strongly concentrate around 65° and 60°, respectively. This is also apparent in the low standard deviation for the Cook and Sognefjord intervals as presented in Table 6.3. Figure 7.3b,d displays all the values for slip and dilation tendency for the Cook and Sognefjord intervals, showing that the highest concentration of data represents high values of dilation tendency and intermediate values of slip tendency. Although the Sognefjord interval exhibit slightly lower average values of dip angles, slip tendency and dilation tendency, results displayed in Figure 7.3b,d suggests that failure in both the Cook and Sognefjord intervals would occur as a mix between hybrid and shear (Mode II/III), the same mode as the Drake cap rock interval (Figure 7.3c,e). Mulrooney et al. (2022) considered the Cook Formation as the primary storage aquifer in the Smeaheia area and conclude that the prevailing mode of failure within this interval is dilation. To compare, results in this study also find the highest values of both slip and dilation tendency within the Cook interval but find slightly higher values of slip tendency than Mulrooney et al.'s (2022) findings, thus shifting the mode of failure towards

hybrid and shear (Figure 7.3d,e). However, in this study both the Cook and Sognefjord intervals were designated high values of coefficient of friction compared to the Shetland and Drake intervals, and so has a stronger resistance to frictional slip.

It is worth noting that Mulrooney et al. (2022) investigated the neighbouring Smeaheia area using the same methods, with similar results. The investigated cap rock was found to exhibit extremely monotonous values of slip tendency, concentrated around 0.4. In contrast to this study, Mulrooney et al. (2022) used a slightly different approach by applying a failure criterion T_s>0.6 for all faults, a commonly accepted value for crustal rocks. Herein, faults were divided into intervals with separate failure criteria based on their designated coefficient of friction: the fault rocks in the Shetland and Drake intervals were designated $\mu = 0.45$, the Sognefjord interval $\mu = 0.8$ and the Cook interval $\mu = 0.6$ (see Table 4.4). Consequently, the slip tendency analysis in Mulrooney et al. (2022) consider the ~0.4 value of slip tendency for the Drake Formation cap rock as safe, wherein this study the same results suggest a significant risk of reactivation by slip.

Considering dilation tendency, Mulrooney et al.'s (2022) result varies little from the results produced in this study. One difference is that they found a contrast between the deepest and shallowest parts of the modelled faults, where the shallower parts exhibit far less dilation tendency. In this study, the contrast lies more specifically between the uppermost Shetland interval and those underlying it (Figure 6.11).

7.2.3 Slip and Fracture Stability vs. Cohesion and Fault Tolerance

The previous subchapter discusses the faults within the Aurora area only considering the in-situ stresses as resolved from Thompson et al.'s (2022) investigation of the 31/5-7 EOS well, as well as fault strike and dip angles. When injecting CO_2 especially one of these pressures will dramatically change: the pore pressure. Post-charge increases in pore pressure might induce failure and so cause seal breach by reducing the minimum effective stress below the tensile strength of the rock (Mildren et al., 2005). It is therefore important to take increases in pore pressure into account when a fault reactivation analysis is performed. This is done by considering the Critical Perturbation Pressure (CPP) which predicts the extra pore pressure (ΔP in MPa), required to put a fault or fracture into shear failure where a lower number means a higher risk of reactivation (see subchapter 3.5). CPP is calculated when performing slip and

fracture stability analysis, two methods that can be used separately or together, with the only difference between them being that fracture stability allows the consideration of cohesive strength within fault rocks.

In chapter 4 the four considered sedimentary intervals were designated lithologies and rock properties based on mineralogy, expected fault rock composition, SGR, and results from previous research (see subchapter 4.5). The four intervals considered in this study were designated a cohesive strength, a coefficient of friction and an angle of internal friction, i.e. Drake was given: C = 1.0 MPa, $\mu = 0.45$ and $\varphi = 24°$ (see Table 4.2). This determination primed the fault segments in the study area for the calculation of CPP.

Figures 6.12 and 6.13 present the results of slip and fracture stability, respectively. As expected from the regional pore pressure gradient (increasing with depth), as provided by Thompson et al. (2022), the deeper Dunlin group (Drake and Cook intervals), exhibit significantly lower values of slip stability compared to the upper Viking Group (Shetland and Sognefjord intervals). Ksd plots reveal this in a ready manner, where graphs for the lower Dunlin Group intervals are significantly shifted towards lower values of CCP, and more strongly concentrated than their Viking group counterparts (Figure 6.12b, Figure 6.13b). Figure 6.12 showcases how close the Drake and Cook intervals are to a critically stressed state. In fact, northern parts of the Drake interval exhibit near-zero values of CPP, indicating a significant risk of reactivation (Table 6.2). Mildren et al. (2005) state that if the segments of the fault that exhibit low CCP are at the top of the sealing structure, then reactivation may lead to breaching of the (hydrocarbon) column. In the case of this study, the fault segments where low CPP are found intersect with both the cap rock and the "body" of a reservoir interval, and so a reactivation within them might jeopardize any column of hydrocarbons or, more relevantly CO_2.

If failure occurs by inducing pore pressure, the structural permeability of the rock would be altered through reactivation of brittle structures such as shear, hybrid or tensile fractures (Mildren et al., 2005). Previous research has demonstrated how such fractures, especially those induced by shear reactivation, act as important conduits for fluid flow (e.g. Barton et al., 1995). Indeed, Wiprut & Zoback (2002) conclude that any fault in a critically stressed state tends to leak, whereas non-critically stressed faults tend to seal. In the previous subchapter, three out of four intervals, the Sognefjord and Cook reservoir intervals and the Drake cap rock interval, were determined to reactivate by a mix of hybrid and shear failure if failure was to occur. It is

very likely, then, that such a reactivation would increase the structural permeability of the faults, and so act as conduits for fluids such as reservoir brine and even supercritical CO_2.

Fortunately, there is abundant evidence that post-deformation lithification and cementation of previously cohesionless fault rocks results in a significant regaining of cohesive strength (see subchapter 3.2, Dewhurst & Jones, 2002). Results created in this study reveal the importance of cohesion when considering fault reactivation and seal assessment (Figure 6.15, 7.4). When considering faults as having cohesive strength, the CPP is significantly reduced to the point where no fault segment exhibits near-zero conditions. This study assigned the lowest value of cohesion to the Drake interval (C = 1 MPa), and the second lowest to the Shetland interval (C = 2 MPa), both cap rocks. An interesting observation is the impact of this +1 MPa of cohesion assigned to the Shetland interval. Despite the in-situ stresses being decidedly lower within the upper Viking group intervals, the result of adding cohesion is significant. Comparing Figure 6.12a to Figure 6.13a, there is a very large difference between the Shetland interval without and with cohesion, while the difference within the Drake interval is minute in comparison, suggesting that even though the pressures in the Viking group are lower, the added cohesion made a critical impact on the calculated tolerance of the fault surfaces. This is also observed in Figure 7.4.

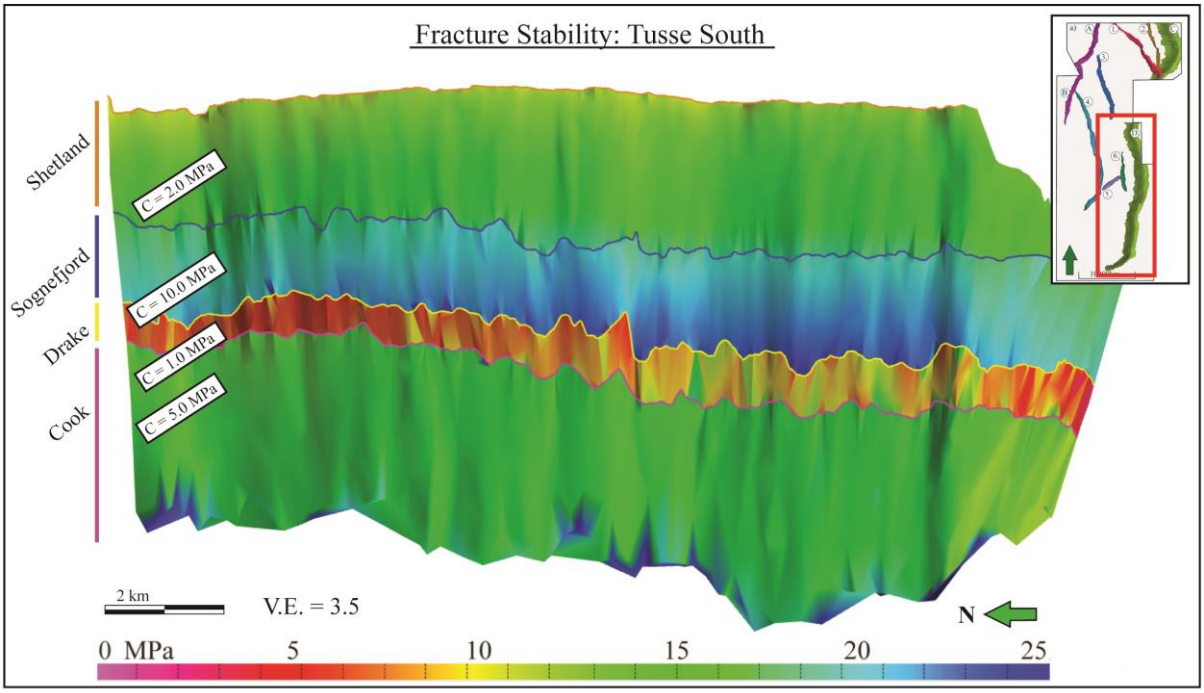

Figure 7.4: Enhanced view of the Tusse South fault segment, showing how Drake deviates from the other three intervals, even within an area where the Drake interval exhibits a significantly high tolerance to increased pressure in comparison to the rest of the study area.

However, an examination of the faults in Figure 6.14a reveals that some fault segments in the southern Aurora area, particularly on the Tusse South fault segment, exhibit significantly higher values where the CPP approach 10.0-14.0 MPa. This particular fault is presented in Figure 7.4, where the Drake interval is compared to the other intervals. It is clear that the contrast between the Drake interval and the other layers is considerable, even in areas where the Drake interval exhibits the highest tolerance to increased pressure found within the study area (Figure 7.4). These results suggest that the southern part of the Tusse South fault can tolerate significantly more extra pressure induced from CO_2 injection, in comparison to the average for fault segments within the Drake interval. Table 6.1 reports that the Tusse South fault does not deviate considerably from the other 1st-order faults, albeit having a strike orientation closest to a perfect N-S direction. Some factors other than dip, strike and cohesion must exist for the Tusse South fault to separate it from the others so dramatically, but this was not investigated further as it is beyond the scope of this study.

Mulrooney et al.'s (2022) investigation of the faults intersecting cap rocks within the Smeaheia area reveals much the same results: it is concluded that when considering faults as cohesionless, >75% of the faults exceeded a failure criterion by an increase of pore pressure of 2 MPa. Adding cohesion reduced this percentage to zero. The criterion used by Mulrooney et al. (2022) was defined specifically for the Smeaheia area. Albeit not operating with a definite CPP failure criterion in this study, a near-complete consensus would exist if set to 2 MPa (see the scale in Figure 6.12b). Furthermore, Mulrooney et al. (2022) discovered a correlation between slip stability and fault dip, where intermediate values of dip (60-65˚) correspond to low values of slip stability. This correlation is indeed recreated in this study, where there is a very strong correlation between S_s< 5 MPa and dip angles between 45-75˚, with the lowest values of slip stability being concentrated around 50-60˚ dip (Figure 7.5a).

Mulrooney et al. (2022) did not find any correlation between dip and fracture stability, whereas results in this study discover an equally strong correlation between these two factors, especially for the Drake interval fault segments (Figure 7.5b). In fact, the correlation between dip angle and slip/fracture stabilities appears identical, which might be expected, as only a single factor separates the two analyses: cohesion.

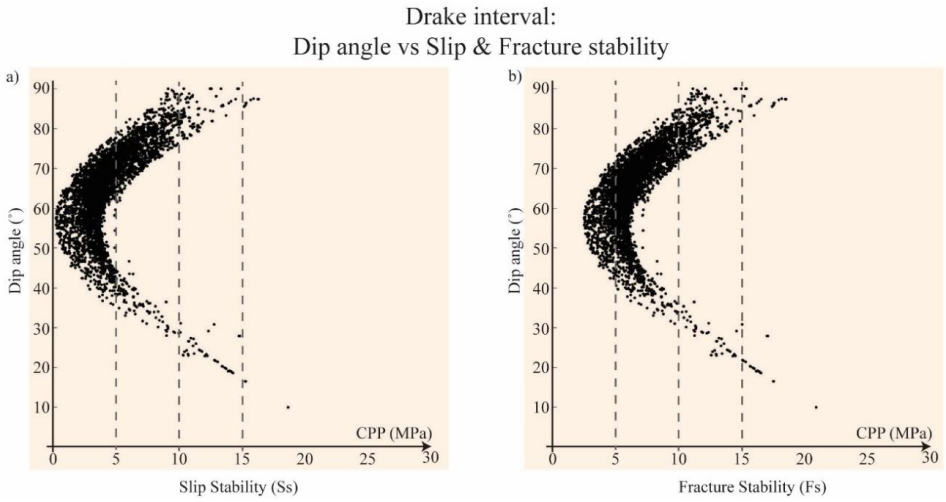

Figure 7.5: Plots made in MatLab with 24666 data points belonging to the Drake interval, showcasing: a) correlation between slip stability (S_s) and dip angle (˚), b) correlation between fracture stability (F_s) and dip angle (˚). Note their extreme similarity, except that b) is shifted towards higher values of CPP.

The correlations found in this study yield an arcuate shape where dip angles gentler and steeper than ~60° result in a progressively increased CPP (Figure 7.5). Table 6.2 reports that, despite local dip variations, the mean dip value for faults intersecting all four intervals lie in the range of 60-68°, showing that no worst-case conditions in terms of dip vs. fracture stability are to be found within the study area. Calculated CPP resulting from the lowest dip values exceed those of the highest dip values, suggesting that gently dipping faults are the most tolerant to an increase in pore pressure. This conforms to suggest that the prevalent mode of failure in such faults would be by compressive shear or compressive failure, which mechanically prevents slip (see subchapter 7.2.2).

As a final remark to this subchapter, for fault segments within the Sognefjord and Cook reservoir intervals the cohesion assigned was comparatively high: 10 MPa and 4 MPa respectively. This amount of cohesive strength has an indisputably positive effect on fault tolerance, as can be observed in Figure 6.13. It is clear that none of the reservoir intervals even approach precarious conditions as both exhibit >10 MPa values of CPP (see Table 6.3). Given the two reservoir interval's large difference in cohesive strength, mineralogy and general lithology, but the conjunctively high tolerance to increased pressures, it is quite clear that sedimentary successions generally accepted as potential reservoir rocks might avoid severe scrutiny with regards to fault reactivation and induced pressure from CO_2 injection. It is the author's opinion that attention and time allotment would be more appropriately directed towards the cap rock evaluation.

7.3 The Drake Interval Reactivation Potential

As mentioned earlier, the intended scenario for CO_2 injection of the Northern Lights project is to utilize Johansen and Cook as storage formations and Drake as the sealing cap rock formation (e.g. Thompson et al., 2022). This subchapter will focus on reactivation potential and risks thereof for the Drake interval in particular, to address the results derived from subchapter 6.4. Appendix B shows more detailed results for the Drake interval slip tendency, dilation tendency and slip stability than is presented in chapter 6. To the author's knowledge, no measurement in terms of expected pressure increase from CO_2 injection has been defined for the Aurora area. Instead, based on Mulrooney et al. (2022), a criterion of 2 MPa will be used as a reference value to assess the threshold of "safe" levels of CPP.

Note that because slip and fracture stability are strongly influenced by in-situ stresses one might expect a trend of much higher CPP values at the northern, shallower elevations. However, no distinction in terms of pressure was made within the analysed intervals. Each interval was assigned a single value for the three principal stress directions and pore pressure, at the top of each interval at the depth they were identified in at well 31/5-7 (see subchapter 4.5.1). In the case of the Drake interval these were: σ_1 = 51.2, σ_2 = 38.0, σ_3 = 36.2 and P = 25.0 in MPa (Table 4.3). It is unknown how the Move software takes elevation into account unless a pressure gradient is specified. As such, each interval had a single pressure profile, regardless of depth. This implies that a factor separated from in-situ stresses exists to differentiate the northern and southern areas. This investigation exceeds the scope of this study but using a pressure gradient deserves further research.

7.3.1 Sensitivity Analysis, Fault Rocks and Tolerance

As previously stated, cohesion reflects a property of the fault rocks within a fault segment. In this study, the Drake interval was given a minute amount of cohesion of 1.0 MPa considering its high percentage of clay minerals, especially smectite (see subchapter 4.5.2, Thompson et al., 2022). By increasing the value of cohesion throughout the sensitivity analysis, what is essentially changed is the expected fault rocks found within faults intersecting the Drake Formation.

Results herein show that the sensitivity analysis of fracture stability strongly depends on cohesion as its leading parameter. In Figure 6.15a or Figure 7.6a what is essentially a slip stability analysis reveals that considering faults as cohesionless puts significant parts of the fault segments within the Drake interval into a critically stressed state. A cohesionless fault corresponds to an active slip plane where the only possible mode of failure is Mode III, shear failure (Mildren et al., 2005). The sensitivity analysis presented in Table 6.3 reports the lowest value of CPP = 0.24 MPa for zero cohesion, implying that only a minute increase in pressure would induce fractures when faults are considered cohesionless. Adding just 0.5 MPa cohesion, as in Figure 6.15b, reveal the importance of faults healing from a cohesionless state. With a 0.5 MPa cohesion, none of the fault segments are critically stressed, albeit very nearly so. An increase from 0.0 to 0.5 MPa cohesion increases the lowest value of CPP by a factor of ~5.5, from 0.24 to 1.36 MPa CPP, whereas the mean value increased by +1.12 CPP (Table 6.3). It should be stated that measuring fault reactivation potential using classic cohesionless faults might lead to an unreasonably low estimate of fault strength within the northern North Sea (see subchapter 4.5.2), although using this condition as a method of highlighting areas of increased risk of reactivation has proved very useful.

Interestingly, Mulrooney et al. (2022) considered PFFR's and smectite-rich fault rocks as having a cohesive strength of 0.5 and 2.0 MPa respectively, thus matching the values of the sensitivity analysis in Figures 6.15b and 6.15d. As described in subchapter 6.4.2, a significant increase in a faults tolerance to induced pressure occurs when considering faults with increased cohesive strengths, e.g. between 0.5, 1.0 and 2.0 MPa (see Figures 6.14a and 6.15b,d). It is determined that for every 0.5 MPa cohesion, the CPP increases by approximately 1.12 MPa. In this study, the Drake Formation's high clay and especially smectite constituents as determined by Thompson et al. (2022) warrant a lower value of cohesion than that of the "smectite-rich" faults in Mulrooney et al. (2022).

Doubling the cohesion parameter from the initial 1.0 to 2.0 MPa appears to have a particularly large impact on the analysis (Figures 6.14a, 6.15d and 7.6b,c). Fault segments that exhibited purple-red colours with the initial conditions now completely fade in favour of orange-yellow-coloured areas. When the fault rocks are measured with 2.0 MPa cohesion, very few areas within the faults exhibit CPP values below ~5.0 MPa (Figure 6.15d). For fracture stability with 2.0 MPa cohesion, Table 6.3 reports the minimum value of CPP being 4.73 MPa, a near-doubled increase of +2.25 MPa from the CPP reported with the initial condition of 1.0 MPa cohesion. Table 6.3 also reports an expected trend in all statistical parameters, where an

increase in cohesive strength progressively increases the mean, minimum, and maximum values of CPP, whereas the standard deviation decreases.

As previously stated, Mulrooney et al. (2022) considered smectite-rich fault rocks as having 2.0 MPa cohesive strength. In this study, 2.0 MPa was the cohesive strength assigned to the Shetland interval, a mudstone-rich cap rock with an SGR of 20-40% (subchapter 4.5, Wu et al., 2021). By utilizing Fisher and Knipe's (1998) classification scheme for fault rocks, the Shetland interval fault rock was interpreted as a clay smear with an increased amount of cohesion compared to the clay smears in the Drake interval. Although being considered as having the same type of fault rock, it is evident how large of a difference the added +1.0 MPa cohesion had for the analysis. For the Drake interval sensitivity analysis, the same effect can be seen by comparing Figures 7.6b and 7.6c, where an added +1.0 MPa cohesion removes purple-red-coloured areas in favour of red-orange and even green, thus relaying a considerable increase in fault tolerance.

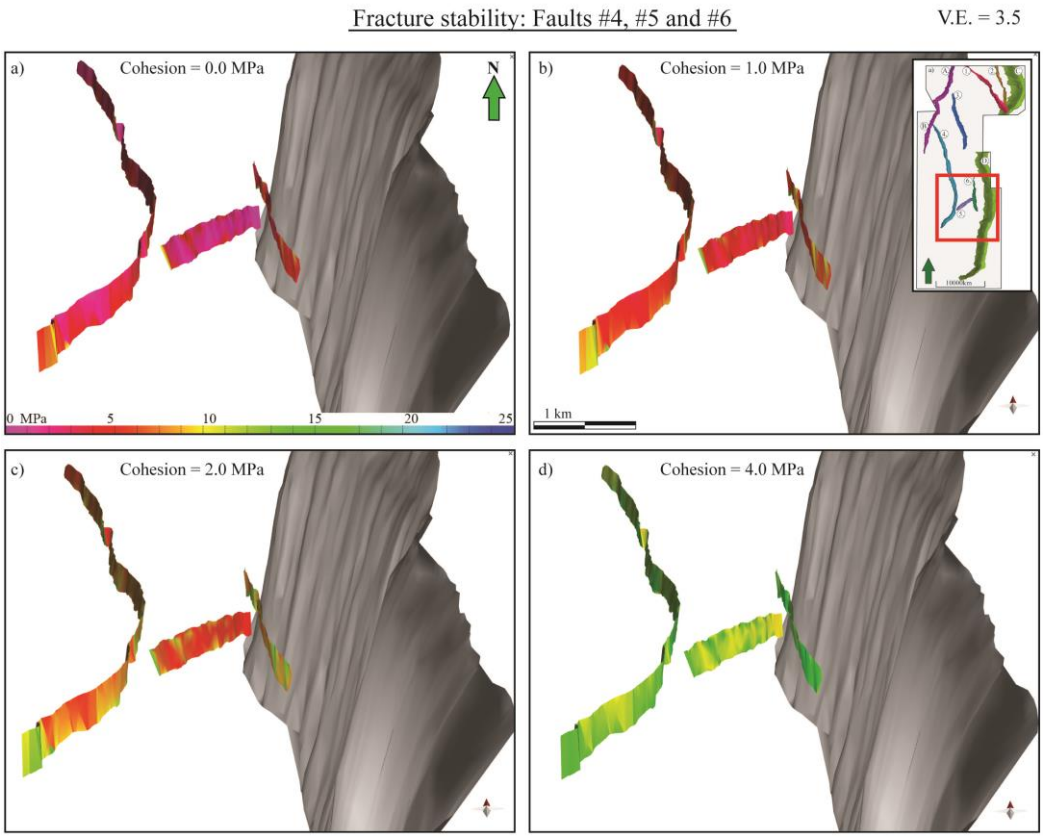

Figure 7.6: Faults #4, 5 and 6 colour draped by fracture stability with different values of cohesion, corresponding to fault rocks discussed in this thesis. a) C = 0.0 MPa, a cohesionless active slip plane, b) C = 1.0 MPa, such as a clay smear with significant amounts of smectite (Drake Formation), c) C = 2.0 MPa, such as the "smectite-rich" fault rocks used by Mulrooney et al. (2022), d) C = 4.0 MPa, close to the cohesive strength designated to the sandstones of the Cook Formation.

By comparing the results herein with the results of Mulrooney et al. (2022) it becomes clear how high an impact the choice of fault rock properties had on the fracture stability analysis, and subsequently the calculated CPP. It is clear that the availability of detailed lithological information, fault rock rheology and reports on proximate in-situ stresses is essential for a fault reactivation study.

The end member of the sensitivity analysis designates the Drake interval with an unreasonably high value of cohesion of 4.0 MPa, considering the intervals very high (~70%) amount of clay mineral constituents (see subchapter 4.5). The results of the analysis reveal that an exaggerated amount of cohesion within the fault rocks of the Drake interval adds an extreme tolerance to increase of pressure (Figure 6.15e, 7.6d and 7.7). Table 6.3 now reports the lowest value of CPP as high as 9.20 MPa, with a mean value of 13.10 MPa, meaning even the most exposed fault segments do not even approach the criterion used by Mulrooney et al. (2022).

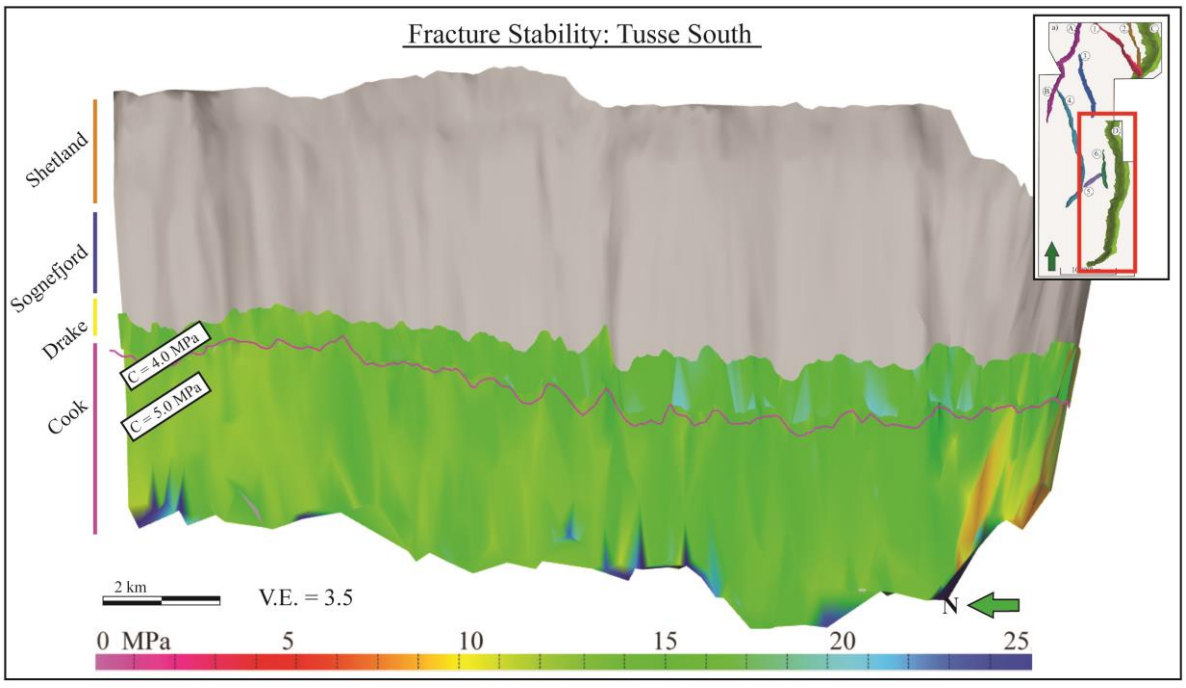

Figure 7.7: Comparison between the Drake and Cook intervals on the Tusse South fault, where the Drake shales are designated an unreasonably high amount of cohesive strength (4.0 MPa). The sandstones of Cook were designated a cohesive strength of 5.0 MPa.

Considering the results of the Drake interval sensitivity analysis with 4.0 MPa cohesion, a comparison can be made between the shales of the Drake interval and sandstones of the Cook interval, whose designated value of cohesion was 5.0 MPa (Figure 7.7). By observing the colours of the Drake and Cook intervals in Figure 7.7, it becomes clear that they are now more or less equal, and not close to a critical condition. Although it might not make geological sense for a shale to exhibit the same cohesive strength as a sandstone, it nevertheless highlights the dependence of cohesion as a parameter when performing a fault reactivation analysis.

7.3.2 Exposed Fault Segments and Consequences of Reactivation

Investigation of the results from the slip stability and fracture stability analyses reveals that some fault segments within the Drake interval display disconcerting values of critical perturbation pressure (see Figure 6.14). This is visualized as the short distance between the failure envelope and the Mohr circle in Figure 6.14c, a feature that is enhanced in the cohesionless slip stability analysis presented in Appendix B.3. This distance represents the CPP and is equal to the extra pressure (ΔP) needed to put the fault into a critically stressed state (see Figure 3.4).

Consider fault segments within the Drake cap rock as having a cohesion of $C \leq 1.0$. If faults are considered cohesionless, then close to 90% of all fault segments in the study area are already within range of a critically stressed state, correspondingly exceeding the failure criteria for the Smeaheia area by far (Appendix B.3). The lowest value of slip stability found in the study area was 0.2 MPa, which is significantly lower than the threshold used by Mulrooney et al. (2022) of 2.0 MPa (Table 6.2).

Figure 7.8 presents a magnified version of all Drake interval fault segments colour draped with slip- and fracture stability analysis, in a) and b) respectively. Areas where the slip stability analysis display values below Mulrooney et al.'s (2022) criteria of 2.0 MPa CPP are highlighted by rings (Figure 7.8a). These zones of low CPP signify areas that should be more closely observed and further researched as areas of increased risk of fault reactivation due to an increase in pressure from CO_2 injection. Six zones were identified, two of which reside underneath the Troll oil and gas fields. Another two are situated south of the injection well 31/5-7, at the southern tip of fault #4 and the entire fault #5 (Figure 7.8). Since these two zones and the two underneath the Troll oil and gas fields are distal and/or down-dip from the injection

well they were not considered further. However, one zone is situated at the northern tip of fault #4 where it bends towards the Tusse fault segments (termed Zone 1), and another is in close proximity to the intersecting point between Tusse North and Tusse South (termed Zone 2), see notations in Figure 7.8a. Due to their proximate position immediately north and up-dip from the EOS injection well 31/5-7, Zone 1 and 2 are considered critical with regards to achieving geological control.

When considered as cohesionless or with 1.0 MPa cohesion, faults Tusse South, Tusse North and #4 exhibit overall levels of CPP ≈ 5.0 MPa, suggesting intermediate tolerance to an increase of pressure (Figure 7.8). However, the chain is only as strong as its weakest link. Thus, the local occurrences of significantly decreased CPP within Zone 1 and 2 might jeopardize the accommodation of CO_2 in the area. In fact, even with the designated value of cohesive strength for the Drake interval of 1.0 MPa, segments within Zone 1 and 2 might approach an unacceptably low value of CPP > 2.0 MPa. With 1.0 MPa cohesion, the lowest value of CPP from the fracture stability analysis was 2.5 MPa, with a mean value of 6.8 MPa. This is presented in Table 6.2 and is seen as red colours present throughout the entire study area (Figure 7.8b). This means that a reservoir-wide increase of 2.5 MPa would put the most exposed segments of the faults into a critically stressed state, even when considered with a cohesive strength of 1.0 MPa.

Although no hard linkage between the Tusse fault segments and fault #4 was mapped in this study, other authors have indeed mapped 2nd-order faults in proximity to the 31/5-7 injection well that is hard-linked to the Tusse fault zone (i.e. Duffy et al., 2015; Holden, 2021). If hard linkages exist between the Tusse fault and 2nd-order faults in its vicinity, then the occurrence of structural traps is a possibility and CO_2 injected into the 31/5-7 well could migrate up-dip and accommodate into such structural traps. Indeed, Holden (2021) assessed plausible CO_2 migration pathways from the 31/5-7 injection well into structural traps produced by the Tusse fault and abutting 2nd-order faults. Holden (2021) argues that a sufficiently large plume of CO_2 in the underlying Cook reservoir interval would encounter what is in this study called fault #4. Subsequently, the migrating CO_2 plume would be channelled parallel to fault #4's strike, along which accumulations and pressure build-ups are unlikely. However, the presence of triangular, fault-bound traps constructed by the abutting of 2nd-order faults into the Svartalv fault segments might accumulate significant amounts of CO_2 (Holden, 2021). The location of these closures approximately corresponds to Zone 2 (Figure 7.9).

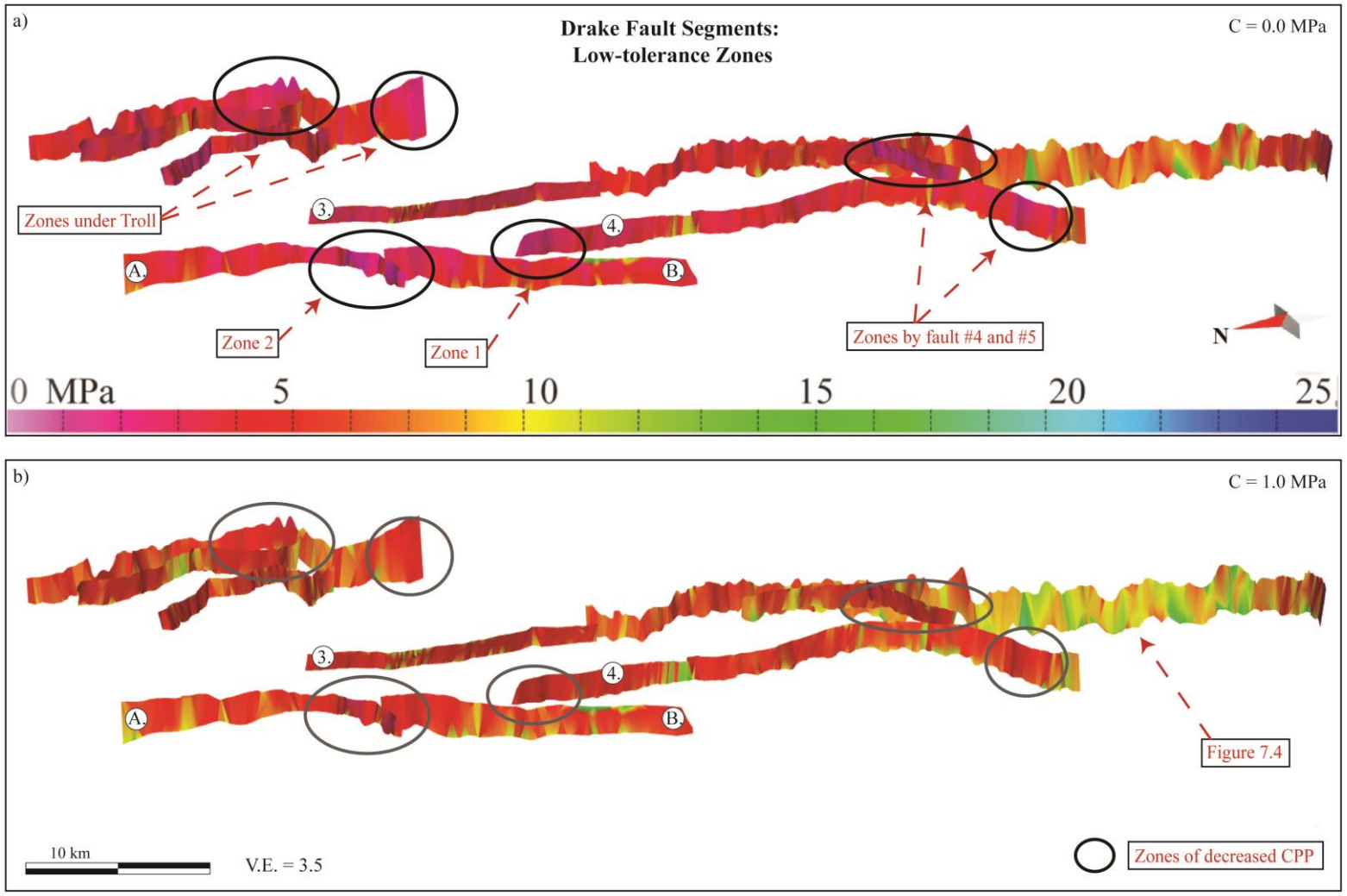

Figure 7.8: Considerably exposed zones within the Drake interval fault segments. a) fracture stability analysis is used with 0.0 MPa cohesion to highlight exposed areas. b) fracture stability analysis performed with the Drake intervals initial parameters (1.0 MPa cohesion), areas from a) are duplicated. Faults A, B, 3, and 4 are the Svartalv North, South, fault #3 and #4, respectively. Areas beneath the Troll oil and gas fields are indicated.

Along the CO_2 migration pathway into the third triangular closure, as postulated by Holden (2021), the migrating CO_2 plume would first encounter Zone 1 and subsequently Zone 2 of increased risk of fault reactivation (Figure 7.9). The accumulation of CO_2 in these zones would inevitably lead to an increase in pressure that the fault segments within the zones might not be able to withstand.

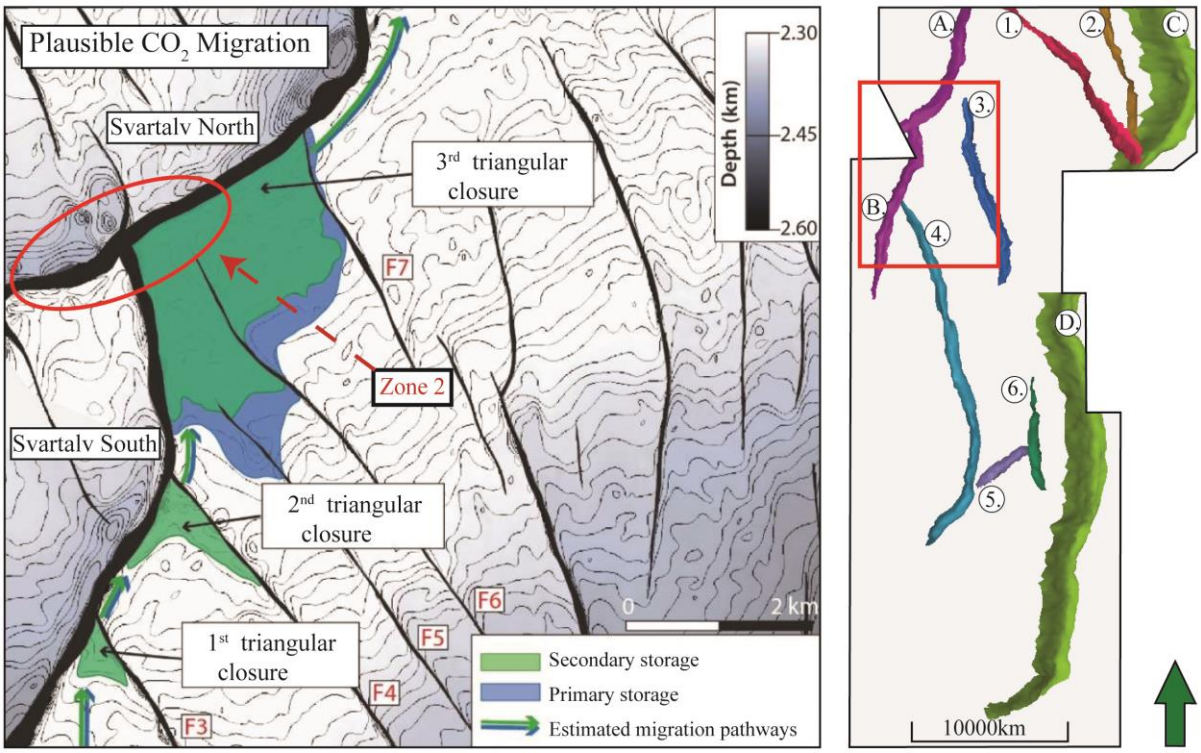

Figure 7.9: Magnified part of the Tusse North and South fault segments, with plausible storage complexes as advocated by Holden (2021). The approximate location of Zone 2 from this study is highlighted. Note that fault F3 corresponds to fault #4, and fault F7 approximately corresponds to fault #3. Modified from Holden (2021).

Figure 7.10 displays the fault segments within Zone 1 and 2 colour draped by fracture stability given different amounts of cohesion representing the sensitivity analysis. The calculated critical perturbation pressure in Figure 7.10a,b shows how induced pressure amounting to a local increase of 2.5 MPa might put these segments of the Drake fault into a critically stressed state (see Table 6.2). Although a CPP of 2.5 MPa surpasses the criterion used by Mulrooney et al. (2022) for the Smeaheia area, it is nevertheless proposed herein that the fault tolerance of these segments should exceed this criterion. Given the large mass of CO_2 that Holden (2021) suggests can be stored within these closures (cumulatively 0.259 Mt CO_2 within Zone 2), the local increase in pressure might exceed 2.5 MPa.

Results within this study imply that the integrity of the structural closures and the faults that produce them are highly dependent on the cohesive strength of the faults, and thus the nature of the fault rocks found within these segments. As discussed above, fault rocks exhibiting a cohesive strength of 0.0-1.0 MPa might not be strong enough to withstand the extra pressure induced by a large amount of injected CO_2. Especially when considering fault rock heterogeneity or local points of weakness smaller than what the seismic resolution allows to be mapped. Nevertheless, if future endeavours were to prove the fault rocks within the Drake Formation in these zones as having a cohesive strength of ≥2.0 MPa, then injection of CO_2 could with high certainty be completed without much concern. With these conditions, the fault tolerance of the Drake interval segments in Zone 2 exceeds 4.5 MPa CPP, even in the most exposed areas (see Figure 7.10c,d).

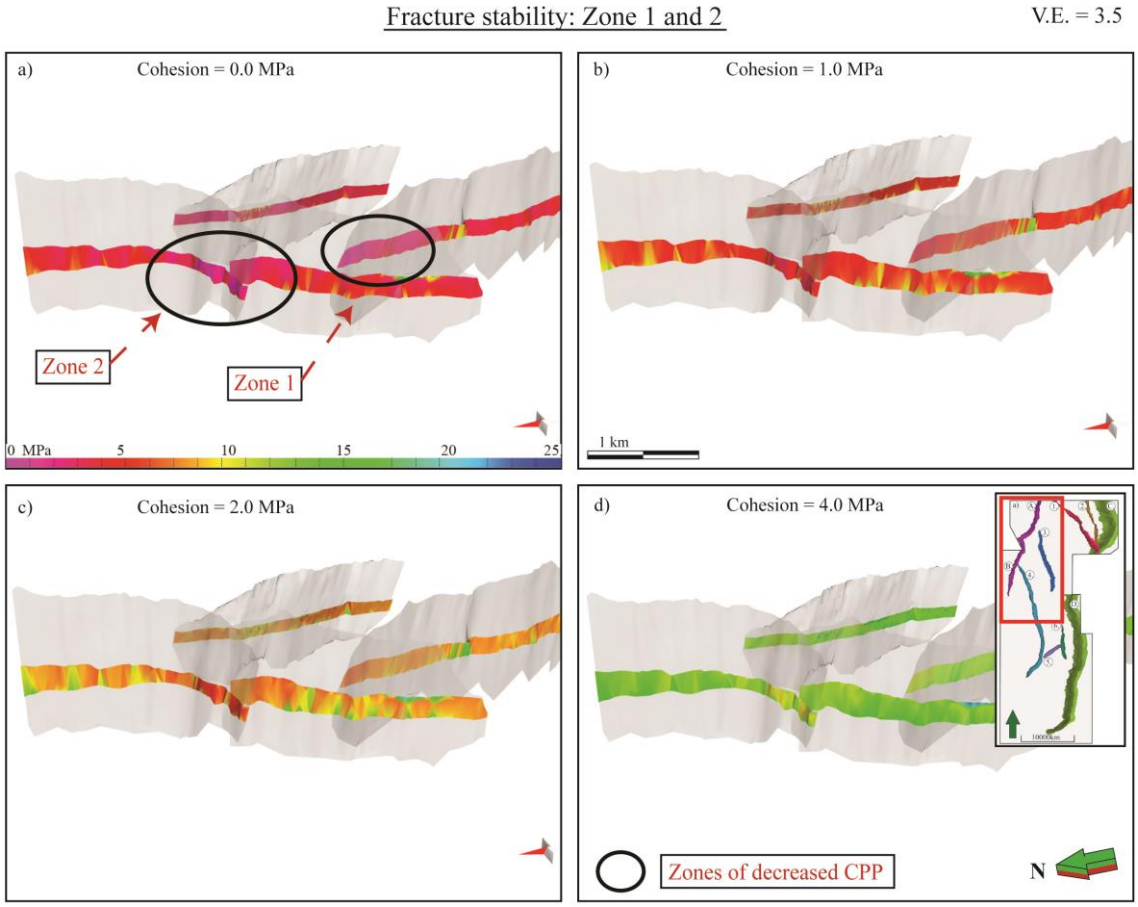

Figure 7.10: Faults surrounding Zone 1 and 2, colour draped by fracture stability performed with different values of cohesion used in the sensitivity analysis. a) C = 0.0 MPa, a cohesionless active slip plane, b) C = 1.0 MPa, such as a clay smear with significant amounts of smectite (Drake Formation), c) C = 2.0 MPa, such as the "smectite-rich" fault rocks used by Mulrooney et al. (2022), d) C = 4.0 MPa, close to the cohesive strength designated to the sandstones of the Cook Formation. The figure is intended to highlight that the tolerance to increased pressure due to CO_2 injection strongly relies on the nature of the fault rocks within the Drake interval.

As a final remark, there are several possible outcomes for a scenario where sufficient pressure is induced to reactivate the fault segments of Drake within Zone 1 or 2. Abundant research shows that critically stressed or active faults provide conduits for fluid flow during deformation (e.g. Barton et al., 1995; Sibson, 1995; Wiprut & Zoback, 2000). This is often achieved by destroying juxtaposition seals or by creating conduits through opening Mode I fractures (Mildren et al., 2005). These conduits can be used by overpressured pore fluids, leading to an episodical up-dip discharge of fluids until a hydrostatic gradient is regained (e.g. Sibson, 1995). While results herein indicate that a mixed failure mode between hybrid and shear failure is a more likely outcome than purely tensile, at least for the Dunlin Group intervals, all critically stressed faults might act as such conduits (Figure 7.3, Wiprut & Zoback, 2002).

Holden (2021) calculate that CO_2 injected into the 31/5-7 well would take approximately 161-210 years to reach the storage closure at Zone 2. Up until this point, the pressure would increase incrementally but the reservoir would be filled exclusively with brine. Accordingly, and given sufficient geological control of the faults in this zone (Svartalv North, South and fault #4), controlled fault reactivation could be induced to episodically funnel brine out of the reservoir. Thus sustaining a hydrostatically pressured reservoir for the injected CO_2 without the concern of intolerable pressure build-ups.

7.4 Limitations

Managing limitations and uncertainties will always be a part of sub-surface modelling and analysis. As described in subchapter 4.4 the limitations to conventional seismic interpretation are many and often unsolvable for the common user. In this subchapter, the limitations of the interpreted geomodel and the subsequent fault reactivation analyses will be disclosed:

- The foundation of the analyses used in this study is a good interpretation. Alas, manual interpretation will always be influenced by the interpreter and human errors. These uncertainties will follow through the creation of fault and horizon models and the subsequent analysis. Choosing the right strategy for fault interpretation is essential, but even the best strategy might omit details (e.g. Michie et al., 2021).

- Faults zones consist of complex geometries, damage zones and multiple slip surfaces. A seismic interpretation of a fault is a single 2D surface, and so omits features that are

guaranteed to exist in nature. The geomodel is thus dependent on the vertical and horizontal limits of the seismic data, and the general quality thereof. Furthermore, lateral variations and fault zone heterogeneity always exist, and so a generalization of lithology within a fault segment cannot match what is found in nature.

- In this study, the sedimentary successions were divided into four different intervals and assigned a simplified host rock lithology. This is an over-simplification, especially given the size of the intervals. Additionally, in-situ pressure magnitudes were extracted for the top of the intervals from data by Thompson et al. (2022), at the depth of which the intervals are identified in well 31/5-7. An implication of this is that the pressure data is very accurate for the area encompassing this well, but degrading in accuracy with distance. A different approach would be to apply a pressure gradient for the region using the data Thompson et al. (2022) presents However, this was not possible due to limitations within the Move software.

- Using current-day fault reactivation analyses, results herein show that a fault segment's tolerance to increased pressure is significantly dependent on cohesion as a property of the fault rocks within a segment. As mentioned, exact measurements of the fault rocks within each fault are exceedingly rare and expensive to provide, and so their geomechanical properties have to be inferred from their respective host rock and laboratory results from previous studies. This lack of data entails severe uncertainties for the analysis made in this study and probably applies to the coefficient of friction as well.

7.5 Suggestions for Further Research

This study provides research that adds to the geomodel and geological understanding of the Horda Platform and the Aurora area, especially concerning the reactivation potential of the faults therein. However, several subjects are outside the limits or the scope of this study or deserve more research. This includes:

- Applying a pressure gradient instead of specific values for the Drake and Cook formations allows for a better assessment of what bearing factors such as burial depth and overburden pressure have on the analysis.

- Further investigation into the correlation between fault reactivation and fault strike orientation in relation to the in-situ stresses. Herein, a contrast is observed between faults segments that strike perpendicular to σ_H and those faults that do not e.g., fault #5 and jogs on Tusse North, but no further investigation was undertaken. It could prove interesting to investigate how much impact the strike direction has, and how much influence the strike of jogs has on the rest of the fault segment.

- Investigation of the links between fault interaction styles and fault tolerance, or other factors such as dip variations, jogs in strike direction and hard linkage of fault segments. A study specifically on fault rocks vs. fault tolerance could prove very useful, considering that the cohesive strength of fault rocks is a decisive factor. Furthermore, in this study, a sensitivity analysis was performed by varying only cohesion. A more detailed analysis where different values of cohesion, coefficient of friction and in-situ stresses were tested could prove interesting.

- Ferrill et al. (2017) advocate that fault strength tends to be greatest where competent layers are in contact across the fault, and that weak beds smeared between juxtaposed competent layers tend to weaken the overall fault strength. In this study, faults were divided horizontally based on the cut-off lines of the hanging wall strata of reservoir and cap rocks. A different division based on the juxtaposition of sand-on-sand or sand-on-shale could be of interest, wherein Ferrill et al.'s (2017) hypothesis could be tested.

- A case study where Zone 1 and Zone 2 of this study are investigated in greater detail, considering that they coincide with the storage complexes found by Holden (2021). A more detailed sub-division of the Drake Formation based on Thompson et al. (2022), as well as a separation of the Cook and Johansen reservoir formations could be attempted to narrow down where the potential threat to fault reactivation lies.

8 Conclusion

The Northern Lights project is an ongoing mission that aims to start injection of CO_2 into the Aurora area by using well 31/5-7, thus developing a full-scale CCS value chain by the year 2024. Injection of CO_2 will inevitably lead to an increase of pressure within the reservoir that eventually propagate into the intended cap rock. Out of concern that critically stressed faults might leak fluids, an investigation into the integrity of the fault systems within the Aurora area was undertaken. In light of this, the main objectives of this study were to:

i) Advance geological control of 1st- and 2nd-order faults within the Aurora area by investigating fault scale, displacement, dip angle and strike orientation.
ii) Use literature to determine the orientation and magnitude of the in-situ stresses in the Aurora area as well as the lithology and geomechanical properties of inherent fault rocks.
iii) Utilize four methods of assessing fault reactivation potential and investigate links between critical perturbation pressure, failure mode, fault rock composition, fault dip angle, strike orientation, and in-situ pressures.
iv) Especially investigate the Drake Formation, the intended cap rock, considering increased pressures due to CO_2 injection and the integrity of the storage complexes.
v) Detect and highlight zones of considerably high risk of fault reactivation, and determine the faults' tolerance to increased pressure within the zones.

Objectives i) and ii) were met by creating a geomodel of selected faults and horizons within the Aurora Area using the GN10M1 3D seismic survey and well data. Subsequently, four separate fault reactivation analyses were performed along with an assessment of their links to fault geometries such as strike, dip, and displacement. Fault reactivation potential and failure mode and their dependence on fault- and host rock lithological composition and geomechanical properties were also investigated. Objectives iii) and iv) were met by focusing the investigation on the Drake interval and exploring areas of especially high risk of reactivation, and subsequently highlighting such areas. A sensitivity analysis centred on the cohesion parameter was performed to test the designated properties of the fault rocks within the Drake interval and to compare them with other possible fault rocks.

The main observations and results for these objectives are:

- The fault systems within the Aurora Area consist of two distinct populations that vary in degrees of vertical and lateral extent. The 1st-order population are basement-involved and overall larger-scaled with considerably more displacement than the 2nd-order population. The latter is smaller-scaled, exhibits very low displacement and is stratabound to post-Triassic and Cretaceous successions.

- The fault populations vary little in terms of strike direction or dip angle. The majority of faults strike N-S or NW-SE, with only one exception – fault #5 strikes NE-SW at 55°N. In terms of dip, all mapped faults exhibit a large range of angles, but they all have a mean angle between 55-65°. The four 1st-order fault segments mapped in this study are the Tusse North and South and Svartalv North and South, all with a westwards dip direction. Of the six 2nd-order populations, three are synthetic and three are antithetic to the 1st-order faults.

- Results herein show that slip and dilation tendency strongly depend on fault geometries, especially dip and strike, and their relation to the regional in-situ stresses. The orientation of dip and strike strongly affect the stresses that a fault surface experiences. Faults that strike near-parallel to σ_H exhibit lower dilation tendencies (e.g., fault #5) in contrast to those segments that strike at a perpendicular angle. It is also shown how fault segments with steeper dip exhibit higher slip tendencies.

- A relationship is found between dip angles and slip vs. dilation tendency, subsequently allowing an assessment of which failure mode is plausible for the fault segment. Herein, the relationship is used to decide that the most plausible mode of failure for the Shetland interval is a mode between compactive shear and compactive failure (Mode IV and V), although reactivation in Shetland is unlikely. Failure mode for the Sognefjord, Drake and Cook intervals is most likely a mix of hybrid and shear failure (Mode II and III). In contrast to previous studies, results herein show a significant risk of reactivation by slip and/or dilation within the Drake interval fault segments.

- Results herein show that slip and fracture stability strongly depend on the cohesion parameter, in addition to the regional in-situ stresses and fault geometries. Fault rocks

with greater cohesive strength significantly increase a fault segment's tolerance to increased pressure. For every 0.5 MPa extra cohesive strength, the CPP increases by approximately 1.12 MPa. A relationship is also found between slip and fracture stability and dip angles, where intermediate dip angles (~60°) lead to the lowest calculated CPP, i.e., low tolerance to increases in pressure.

- Results herein show that the Aurora area overall exhibit considerable tolerance to increased pressure due to CO_2 injection, although the Drake interval fault segments are revealed as considerably less tolerant. Considering the fault rocks within the Drake interval as classic cohesionless put some segments into a near-critical state, where even a minute amount of pressure could induce reactivation. This condition is used to highlight areas of high risk of reactivation. Six zones of high risk are identified, where two zones (Zone 1 and 2), are further discussed due to their proximity to the 31/5-7 injection well, and their relationship to storage complexes investigated in previous research.

- Considering the Drake interval with the initially designated cohesive strength of 1 MPa allows a pressure build-up of ~2.5 MPa before the segments within Zones 1 and 2 reach a critically stressed state, in which they are likely to start episodical leakage of reservoir brine or CO_2. Increasing the cohesive strength, corresponding to stronger fault rocks, further increases the tolerance these zones exhibit.

References

Andersen, T. B., & Jamtveit, B. (1990). Uplift of deep crust during orogenic extensional collapse: A model based on field studies in the Sogn-Sunnfjord region of western Norway. *Tectonics*, *9*(5), 1097-1111.

Anderson, E. M. (1905). The dynamics of faulting. *Transactions of the Edinburgh Geological Society*, *8*(3), 387-402.

Andrews, J., Fintland, T., Helstrup, O., Horsrud, P., & Raaen, A. (2016). Use of unique database of good quality stress data to investigate theories of fracture initiation, fracture propagation and the stress state in the subsurface. 50th US Rock Mechanics/Geomechanics Symposium.,

Anell, I., Thybo, H., & Rasmussen, E. (2012). A synthesis of Cenozoic sedimentation in the North Sea. *Basin Research*, *24*(2), 154-179.

Badley, M., Freeman, B., Roberts, A., Thatcher, J., Walsh, J., Watterson, J., & Yielding, G. (1991). Fault Interpretation During Seismic Interpretation and Reservoir Evaluation: Fractured Reservoirs: Origin, Description, Evaluation.

Badley, M., Price, J., Dahl, C. R., & Agdestein, T. (1988). The structural evolution of the northern Viking Graben and its bearing upon extensional modes of basin formation. *Journal of the Geological Society*, *145*(3), 455-472.

Bartholomew, I., Peters, J., & Powell, C. (1993). Regional structural evolution of the North Sea: oblique slip and the reactivation of basement lineaments. Geological Society, London, Petroleum Geology Conference Series.,

Barton, C. A., Zoback, M. D., & Moos, D. (1995). Fluid flow along potentially active faults in crystalline rock. *Geology*, *23*(8), 683-686.

Bell, R. E., Jackson, C. A. L., Whipp, P. S., & Clements, B. (2014). Strain migration during multiphase extension: Observations from the northern North Sea. *Tectonics*, *33*(10), 1936-1963.

Bjørlykke, K. (2010). Well logs: a brief introduction. In *Petroleum Geoscience* (pp. 361-373). Springer.

Bolle, L. (1992). Troll Field: Norway's Giant Offshore Gas Field: Chapter 28.

Brown, A. R. (2011). *Interpretation of three-dimensional seismic data*. Society of Exploration Geophysicists and American Association of Petroleum Geologists.

Byerlee, J. (1978). Friction of rocks. In *Rock friction and earthquake prediction* (pp. 615-626). Springer.

Childs, C., Nicol, A., Walsh, J. J., & Watterson, J. (1996). Growth of vertically segmented normal faults. *Journal of Structural Geology*, *18*(12), 1389-1397.

Corfu, F., Andersen, T., & Gasser, D. (2014). The Scandinavian Caledonides: main features, conceptual advances and critical questions. *Geological Society, London, Special Publications*, *390*(1), 9-43.

Coulomb, C. (1773). Test on the applications of the rules of maxima and minima to some problems of statics related to architecture. *Mem Math Phys*, *7*, 343-382.

Cunningham, J. E., Cardozo, N., Townsend, C., & Callow, R. H. (2021). The impact of seismic interpretation methods on the analysis of faults: a case study from the Snøhvit field, Barents Sea. *Solid Earth*, *12*(3), 741-764.

Davies, R. J., Turner, J., & Underhill, J. R. (2001). Sequential dip-slip fault movement during rifting: a new model for the evolution of the Jurassic trilete North Sea rift system. *Petroleum Geoscience*, *7*(4), 371-388.

Deegan, C. E. S., B.J. . (1977). A standard lithostratigraphic nomenclature for the Mesozoic of the central and northern North Sea. *Oljedirektoratet*(Report 77/25 - Bulletin 1).

Deng, C., Fossen, H., Gawthorpe, R. L., Rotevatn, A., Jackson, C. A., & FazliKhani, H. (2017). Influence of fault reactivation during multiphase rifting: The Oseberg area, northern North Sea rift. *Marine and Petroleum Geology, 86*, 1252-1272.

Denham, L., & Sheriff, R. (1981). What is horizontal resolution? *Proceedings Indonesian Petroleum Association, Tenth Annual Convention*.

Dewhurst, D. N., & Hennig, A. L. (2003). Geomechanical properties related to top seal leakage in the Carnarvon Basin, Northwest Shelf, Australia. *Petroleum Geoscience, 9*(3), 255-263.

Dewhurst, D. N., & Jones, R. M. (2002). Geomechanical, microstructural, and petrophysical evolution in experimentally reactivated cataclasites: Applications to fault seal prediction. *AAPG bulletin, 86*(8), 1383-1405.

Dewhurst, D. N., & Jones, R. M. (2003). Influence of physical and diagenetic processes on fault geomechanics and reactivation. *Journal of Geochemical Exploration, 78*, 153-157.

Duffy, O. B., Bell, R. E., Jackson, C. A.-L., Gawthorpe, R. L., & Whipp, P. S. (2015). Fault growth and interactions in a multiphase rift fault network: Horda Platform, Norwegian North Sea. *Journal of Structural Geology, 80*, 99-119.

Eigestad, G. T., Dahle, H. K., Hellevang, B., Riis, F., Johansen, W. T., & Øian, E. (2009). Geological modeling and simulation of CO 2 injection in the Johansen formation. *Computational Geosciences, 13*(4), 435.

Etris, E. L., Crabtree, N. J., Dewar, J., & Pickford, S. (2001). True depth conversion: more than a pretty picture. *CSEG recorder, 26*(9), 11-22.

Færseth, R. (1996). Interaction of Permo-Triassic and Jurassic extensional fault-blocks during the development of the northern North Sea. *Journal of the Geological Society, 153*(6), 931-944.

Faleide, J. I., Bjørlykke, K., & Gabrielsen, R. H. (2015). Geology of the Norwegian continental shelf. In *Petroleum Geoscience* (pp. 603-637). Springer.

Faleide, J. I., GABRIELSEN, R., JORDT, H., & FANAVOLL, S. (2002). Tectonic impact on sedimentary processes during Cenozoic evolution of the northern North Sea and surrounding areas. *Exhumation of the North Atlantic Margin: Timing, mechanisms and implications for petroleum exploration*(196), 235.

Faleide, T. S., Braathen, A., Lecomte, I., Mulrooney, M. J., Midtkandal, I., Bugge, A. J., & Planke, S. (2021). Impacts of seismic resolution on fault interpretation: Insights from seismic modelling. *Tectonophysics, 816*, 229008.

Ferrill, D. A., & Morris, A. P. (2008). Fault zone deformation controlled by carbonate mechanical stratigraphy, Balcones fault system, Texas. *AAPG bulletin, 92*(3), 359-380.

Ferrill, D. A., Morris, A. P., McGinnis, R. N., Smart, K. J., Wigginton, S. S., & Hill, N. J. (2017). Mechanical stratigraphy and normal faulting. *Journal of Structural Geology, 94*, 275-302.

Ferrill, D. A., Smart, K. J., & Morris, A. P. (2020). Fault failure modes, deformation mechanisms, dilation tendency, slip tendency, and conduits v. seals. *Geological Society, London, Special Publications, 496*(1), 75-98.

Fisher, Q., & Knipe, R. J. (1998). Fault sealing processes in siliciclastic sediments. *Geological Society, London, Special Publications, 147*(1), 117-134.

Fjellanger, E., Olsen, T. R., & Rubino, J. L. (1996). Sequence stratigraphy and palaeogeography of the Middle Jurassic Brent and Vestland deltaic systems, northern North Sea. *Norsk Geologisk Tidsskrift, 76*, 75-106.

Fossen, H. (2010). Extensional tectonics in the North Atlantic Caledonides: a regional view. *Geological Society, London, Special Publications*, *335*(1), 767-793.

Fossen, H. (2016). *Structural geology*. Cambridge University Press.

Fossen, H., & Dunlap, W. J. (1998). Timing and kinematics of Caledonian thrusting and extensional collapse, southern Norway: evidence from 40Ar/39Ar thermochronology. *Journal of Structural Geology*, *20*(6), 765-781.

Gabrielsen, R. H., Kyrkjebø, R., Faleide, J. I., Fjeldskaar, W., & Kjennerud, T. (2001). The Cretaceous post-rift basin configuration of the northern North Sea. *Petroleum Geoscience*, *7*(2), 137-154.

Gassnova. (2011). *Structural Geology of the Horda Platform* (Report: TL-GTL-G-RA-0002, Issue. G. R. Offshore.

Gassnova. (2012). *Geological storage of CO2 from Mongstad. Interim report Johansen Formation* (Report: TL02-GTL-Z-RA-0001, Issue. G. R. Offshore.

Gee, D. G., Fossen, H., Henriksen, N., & Higgins, A. K. (2008). From the early Paleozoic platforms of Baltica and Laurentia to the Caledonide Orogen of Scandinavia and Greenland. *Episodes*, *31*(1), 44-51.

Gee, D. G., Juhlin, C., Pascal, C., & Robinson, P. (2010). Collisional orogeny in the Scandinavian Caledonides (COSC). *Gff*, *132*(1), 29-44.

Haines, S., Marone, C., & Saffer, D. (2014). Frictional properties of low-angle normal fault gouges and implications for low-angle normal fault slip. *Earth and Planetary Science Letters*, *408*, 57-65.

Halland, E., Mujezinovic, J., Riis, F., Bjørnestad, A., Meling, I., Gjeldivk, I., Tappel, I., Bjørheim, M., Rød, R., & Pham, V. (2014). CO 2 Storage Atlas: Norwegian Continental Shelf: Norwegian Petroleum Directorate. *Stavanger, Norway*.

Harris, S. N. (2019). *The Tectono-Sedimentary Development of Smeaheia on the Horda Platform with a Focus on the Cretaceous, and Implications for CO2 Storage* University of Oslo].

Helland-Hansen, W., Ashton, M., Lømo, L., & Steel, R. (1992). Advance and retreat of the Brent delta: recent contributions to the depositional model. *Geological Society, London, Special Publications*, *61*(1), 109-127.

Holden, N. (2021). *Structural characterization and across-fault seal assessment of the Aurora CO2 storage site* University of Oslo].

Ikari, M. J., Marone, C., & Saffer, D. M. (2011). On the relation between fault strength and frictional stability. *Geology*, *39*(1), 83-86.

Isaksen, D., & Tonstad, K. (1989). A revised Cretaceous and Tertiary lithostratigraphic nomenclature for the Norwegian North Sea, Bulleti 5: Norwegian Petroleum Directorate.

Kirkland, C., Daly, J., Eide, E., & Whitehouse, M. (2006). The structure and timing of lateral escape during the Scandian Orogeny: a combined strain and geochronological investigation in Finnmark, Arctic Norwegian Caledonides. *Tectonophysics*, *425*(1-4), 159-189.

Kyrkjebø, R., Gabrielsen, R., & Faleide, J. (2004). Unconformities related to the Jurassic–Cretaceous synrift–post-rift transition of the northern North Sea. *Journal of the Geological Society*, *161*(1), 1-17.

Lepercq, J.-Y., & Gaulier, J.-M. (1996). Two-stage rifting in the North Viking Graben area (North Sea): inferences from a new three-dimensional subsidence analysis. *Marine and Petroleum Geology*, *13*(2), 129-148.

Lothe, A., Gabrielsen, R., Hagen, N. B., & Larsen, B. (2002). An experimental study of the texture of deformation bands: effects on the porosity and permeability of sandstones. *Petroleum Geoscience*, *8*(3), 195-207.

Lothe, A. E., Bergmo, P. E. S., Emmel, B., & Eliasson, P. (2018). Effects of uncertainties in fault interpretations on pressure depletion and CO2 storage injection at Horda Platform, offshore Norway. 14th Greenhouse Gas Control Technologies Conference Melbourne,

Lothe, A. E., Bergmo, P. E. S., & Grimstad, A. A. (2019). Storage resources for future European CCS deployment; a roadmap for a Horda CO2 storage hub, offshore Norway. *The 10th Trondheim Conference on CO2 Capture, Transport and Storage*(SINTEF Proceedings no 4).

Lyon, P., Boult, P., Mitchell, A., & Hillis, R. (2004). Improving fault geometry interpretation through'pseudo-depth'conversion of seismic data in the Penola Trough, Otway Basin.

Marjanac, T., & Steel, R. J. (1997). Dunlin Group sequence stratigraphy in the northern North Sea: a model for Cook Sandstone deposition. *AAPG bulletin*, *81*(2), 276-292.

McKenzie, D. (1972). Active tectonics of the Mediterranean region. *Geophysical Journal International*, *30*(2), 109-185.

Meng, Z., Zhang, J., & Peng, S. (2006). Influence of sedimentary environments on mechanical properties of clastic rocks. *Environmental geology*, *51*(1), 113-120.

Michie, E. H., Mulrooney, M., & Braathen, A. (2021). Fault interpretation uncertainties using seismic data, and the effects on fault seal analysis: a case study from the Horda Platform, with implications for CO2 storage. *Solid Earth*, *12*, 28.

Mildren, S. D., Hillis, R. R., Lyon, P. J., Meyer, J. J., Dewhurst, D. N., & Boult, P. J. (2005). FAST: a new technique for geomechanical assessment of the risk of reactivation-related breach of fault seals.

Miocic, J. M., Johnson, G., & Gilfillan, S. M. (2014). Fault seal analysis of a natural CO2 reservoir in the Southern North Sea. *Energy Procedia*, *63*, 3364-3370.

Mondol, N. H. (2010). Seismic exploration. *Petroleum Geoscience*, 375-402.

Morris, A., Ferrill, D. A., & Henderson, D. B. (1996). Slip-tendency analysis and fault reactivation. *Geology*, *24*(3), 275-278.

Morrow, C., Moore, D. E., & Lockner, D. (2000). The effect of mineral bond strength and adsorbed water on fault gouge frictional strength. *Geophysical research letters*, *27*(6), 815-818.

Mulrooney, M. J., Osmond, J., Michie E. H., Skurtveit, E., & Braathen, A. (2022). Fault reactivation analysis of the Smeaheia fault block, northern Horda Platform, North Sea: Implications for CO2 storage.

Mulrooney, M. J., Osmond, J., Skurtveit, E., Wu, L., & Braathen, A. (2018). Smeaheia, a potential Northern North Sea CO2 storage site: Structural description and de-risking strategies. 5th CO2 Geological Storage Workshop,

Mulrooney, M. J., Osmond, J. L., Skurtveit, E., Faleide, J. I., & Braathen, A. (2020). Structural analysis of the Smeaheia fault block, a potential CO2 storage site, northern Horda Platform, North Sea. *Marine and Petroleum Geology*, *121*, Article 104598. https://doi.org/10.1016/j.marpetgeo.2020.104598

Nazarian, B., Thorsen, R., & Ringrose, P. (2018). Storing Co2 in a Reservoir Under Continuous Pressure Depletion; a Simulation Study. 14th greenhouse gas control technologies conference Melbourne,

NCCS. (2020). *2020 Annual Report*.

NCCS. (2021). *Structural Derisking (Task 9)* Norwegian CCS Research Centre. https://www.sintef.no/projectweb/nccs/research/structural-derisking/#/

NGI. (2021). *FRISK*. https://www.ngi.no/eng/Projects/FRISK

Nooraiepour, M., Mondol, N. H., Hellevang, H., & Bjørlykke, K. (2017). Experimental mechanical compaction of reconstituted shale and mudstone aggregates: Investigation

of petrophysical and acoustic properties of SW Barents Sea cap rock sequences. *Marine and Petroleum Geology*, *80*, 265-292.
Norton, M. (1986). Late Caledonide extension in western Norway: A response to extreme crustal thickening. *Tectonics*, *5*(2), 195-204.
Nottved, A., Johannessen, E. P., & Surlyk, F. (2008). The mesozoic of western Scandinavia and East Greenland. *Episodes*, *31*(1), 59.
Nottvedt, A., Gabrielsen, R., & Steel, R. (1995). Tectonostratigraphy and sedimentary architecture of rift basins, with reference to the northern North Sea. *Marine and Petroleum Geology*, *12*(8), 881-901.
NPD. (2021). *Norwegian Petroleum Directorate: FactMaps*. factmaps.npd.no. Retrieved 24.03.2021 from https://factmaps.npd.no/factmaps/3_0/
NPD. (2022, 17.02.2022). *NPD Factpages*. Retrieved 17.02.2022 from https://factpages.npd.no/en
Osmond, J. L., Mulrooney, M. J., Holden, N., Skurtveit, E., Faleide, J. I., & Braathen, A. (2022). Structural traps and seals for expanding CO2 storage in the northern Horda platform, North Sea. *AAPG bulletin*(20,220,404).
Osmond, J. M., M.J.; Skurtveit, Elin; Faleide, Jan Inge; Braathen, Alvar. (2021). Structural traps and seals for expanding CO2 storage in the northern Horda Platform, North Sea. *AAPG bulletin*, *Thematic Set on Geologic Controls on Carbon Subsurface Utilization and Storage*.
Peacock, D., & Sanderson, D. (1992). Effects of layering and anisotropy on fault geometry. *Journal of the Geological Society*, *149*(5), 793-802.
Pei, Y., Paton, D. A., Knipe, R. J., & Wu, K. (2015). A review of fault sealing behaviour and its evaluation in siliciclastic rocks. *Earth-Science Reviews*, *150*, 121-138.
Phillips, T. B., Fazlikhani, H., Gawthorpe, R. L., Fossen, H., Jackson, C. A. L., Bell, R. E., Faleide, J. I., & Rotevatn, A. (2019). The influence of structural inheritance and multiphase extension on rift development, the NorthernNorth Sea. *Tectonics*, *38*(12), 4099-4126.
Platform, P. E. P. S. (2015). *Recommended Seismic Volume Attributes*. Retrieved 09.03.2022 from https://www.software.slb.com/-/media/software-media-items/software/documents/external/product-sheets/petrel_recommended_seismic_volume_attributes_2015_poster.pdf
Rahman, M. J., Fawad, M., & Mondol, N. H. (2020). Organic-rich shale caprock properties of potential CO2 storage sites in the northern North Sea, offshore Norway. *Marine and Petroleum Geology*, *122*, 104665.
Regjeringen.no. (2021). *Longskip - Approval of plans for CO2-storage*. Retrieved 14.09.2021 from https://www.regjeringen.no/en/aktuelt/godkjenner-utbyggingsplan-for-co2-lagring/id2837595/
Reynolds, J. M. (2011). *An introduction to applied and environmental geophysics*. John Wiley & Sons.
Roberts, D. (2003). The Scandinavian Caledonides: event chronology, palaeogeographic settings and likely modern analogues. *Tectonophysics*, *365*(1-4), 283-299.
Rotevatn, A., Jackson, C. A.-L., Tvedt, A. B., Bell, R. E., & Blækkan, I. (2019). How do normal faults grow? *Journal of Structural Geology*, *125*, 174-184.
Saffer, D. M., & Marone, C. (2003). Comparison of smectite-and illite-rich gouge frictional properties: application to the updip limit of the seismogenic zone along subduction megathrusts. *Earth and Planetary Science Letters*, *215*(1-2), 219-235.
Sheriff, R. E. (1977). Limitations on resolution of seismic reflections and geologic detail derivable from them: Section 1. Fundamentals of stratigraphic interpretation of seismic data.

Sheriff, R. E., & Geldart, L. P. (1995). *Exploration seismology*. Cambridge university press.

Shimamoto, T., & Logan, J. M. (1981). Effects of simulated fault gouge on the sliding behavior of Tennessee sandstone: nonclay gouges. *Journal of Geophysical Research: Solid Earth*, *86*(B4), 2902-2914.

Sibson, R. (1977). Fault rocks and fault mechanisms. *Journal of the Geological Society*, *133*(3), 191-213.

Sibson, R. H. (1985). A note on fault reactivation. *Journal of Structural Geology*, *7*(6), 751-754.

Sibson, R. H. (1995). Selective fault reactivation during basin inversion: potential for fluid redistribution through fault-valve action. *Geological Society, London, Special Publications*, *88*(1), 3-19.

Sibson, R. H. (2003). Brittle-failure controls on maximum sustainable overpressure in different tectonic regimes. *AAPG bulletin*, *87*(6), 901-908.

Skurtveit, E., Choi, J. C., Osmond, J., Mulrooney, M., & Braathen, A. (2018). 3D fault integrity screening for smeaheia CO2 injection site. 14th Greenhouse Gas Control Technologies Conference Melbourne,

Smart, K. J., Ferrill, D. A., & Morris, A. P. (2009). Impact of interlayer slip on fracture prediction from geomechanical models of fault-related folds. *AAPG bulletin*, *93*(11), 1447-1458.

Smart, K. J., Ofoegbu, G. I., Morris, A. P., McGinnis, R. N., & Ferrill, D. A. (2014). Geomechanical modeling of hydraulic fracturing: Why mechanical stratigraphy, stress state, and pre-existing structure matterGeomechanical Modeling of Hydraulic Fracturing. *AAPG bulletin*, *98*(11), 2237-2261.

Spencer, A., & Larsen, V. (1990). Fault traps in the northern North Sea. *Geological Society, London, Special Publications*, *55*(1), 281-298.

Sperrevik, S., Gillespie, P. A., Fisher, Q. J., Halvorsen, T., & Knipe, R. J. (2002). Empirical estimation of fault rock properties. In *Norwegian Petroleum Society Special Publications* (Vol. 11, pp. 109-125). Elsevier.

Steel, R. (1993). Triassic–Jurassic megasequence stratigraphy in the Northern North Sea: rift to post-rift evolution. Geological Society, London, Petroleum Geology Conference series,

Streit, J. E., & Hillis, R. R. (2004). Estimating fault stability and sustainable fluid pressures for underground storage of CO2 in porous rock. *Energy*, *29*(9-10), 1445-1456.

Sundal, A., Miri, R., Ravn, T., & Aagaard, P. (2015). Modelling CO2 migration in aquifers; considering 3D seismic property data and the effect of site-typical depositional heterogeneities. *International Journal of Greenhouse Gas Control*, *39*, 349-365.

Sykes, L. R. (1978). Intraplate seismicity, reactivation of preexisting zones of weakness, alkaline magmatism, and other tectonism postdating continental fragmentation. *Reviews of Geophysics*, *16*(4), 621-688.

Tembe, S., Lockner, D., & Wong, T. f. (2009). Constraints on the stress state of the San Andreas Fault with analysis based on core and cuttings from San Andreas Fault Observatory at Depth (SAFOD) drilling phases 1 and 2. *Journal of Geophysical Research: Solid Earth*, *114*(B11).

Thompson, N., Andrews, J. S., Wu, L., & Meneguolo, R. (2022). Characterization of the in-situ stress on the Horda platform–A study from the Northern Lights Eos well. *International Journal of Greenhouse Gas Control*, *114*, 103580.

Underhill, J. R., & Woodcock, N. H. (1987). Faulting mechanisms in high-porosity sandstones; new red sandstone, Arran, Scotland. *Geological Society, London, Special Publications*, *29*(1), 91-105.

Van den Ende, M., & Niemeijer, A. (2019). An investigation into the role of time-dependent cohesion in interseismic fault restrengthening. *Scientific Reports*, *9*(1), 1-11.

van Ruth, P. J., Nelson, E. J., & Hillis, R. R. (2006). Fault reactivation potential during CO2 injection in the Gippsland Basin, Australia. *Exploration Geophysics*, *37*(1), 50-59.

Vollset, J. D., A.G. (1984). A revised jurassic lithostratigraphic nomenclature for the norwegian north sea. *Oljedirektoratet*(NPD-bulletin no 3).

Wallace, W. (1861). *The laws which regulate the deposition of lead ore in veins: illustrated by an examination of the geological structure of the mining districts of Alston Moor*. E. Stanford.

Watterson, J. (1986). Fault dimensions, displacements and growth. *Pure and Applied Geophysics*, *124*(1), 365-373.

Weiss, J., Pellissier, V., Marsan, D., Arnaud, L., & Renard, F. (2016). Cohesion versus friction in controlling the long-term strength of a self-healing experimental fault. *Journal of Geophysical Research: Solid Earth*, *121*(12), 8523-8547.

Whipp, P., Jackson, C. L., Gawthorpe, R., Dreyer, T., & Quinn, D. (2014). Normal fault array evolution above a reactivated rift fabric; a subsurface example from the northern Horda Platform, Norwegian North Sea. *Basin Research*, *26*(4), 523-549.

Wiprut, D., & Zoback, M. D. (2000). Fault reactivation and fluid flow along a previously dormant normal fault in the northern North Sea. *Geology*, *28*(7), 595-598.

Wiprut, D., & Zoback, M. D. (2002). Fault reactivation, leakage potential, and hydrocarbon column heights in the northern North Sea. In *Norwegian Petroleum Society Special Publications* (Vol. 11, pp. 203-219). Elsevier.

Wu, L., Thorsen, R., Ottesen, S., Meneguolo, R., Hartvedt, K., Ringrose, P., & Nazarian, B. (2021). Significance of fault seal in assessing CO2 storage capacity and containment risks–an example from the Horda Platform, northern North Sea. *Petroleum Geoscience*, *27*(3), petgeo2020-2102.

Würtzen, C. L., Osmond, J. L., Faleide, J. I., Nystuen, J. P., Anell, I. M., & Midtkandal, I. (2021). Syn-to post-rift alluvial basin fill: seismic stratigraphic analysis of Permian-Triassic deposition in the Horda Platform, Norway. *Basin Research*.

Yielding, G. (2009). Using Probabilistic Shale Smear Factor to relate SGR predictions of column height to fault-zone heterogeneity. 2nd EAGE International Conference on Fault and Top Seals-From Pore to Basin Scale 2009,

Yielding, G., Freeman, B., & Needham, D. T. (1997). Quantitative fault seal prediction. *AAPG bulletin*, *81*(6), 897-917.

Ziegler, P. (1982). Triassic rifts and facies patterns in Western and Central Europe. *Geologische Rundschau*, *71*(3), 747-772.

Ziegler, P. (1990). Tectonic and palaeogeographic development of the North Sea rift system. Tectonic evolution of the North Sea rifts,

Ziegler, P. (1992). North Sea rift system. *Tectonophysics*, *208*(1-3), 55-75.

Zoback, M. D. (2010). *Reservoir geomechanics*. Cambridge university press.

Appendices

Appendix A

Table Appendix A.1: Important parameters and abbreviations used in this study. Undefined abbreviations: R = resistive force, N = normal force.

Symbol	Description	Function	Comment
σ_1	Maximum principal stress	Tensor	Typically the overburden pressure
σ_2	Intermediate principal stress	Tensor	Typically horizontal
σ_3	Minimum principal stress	Tensor	Typically horizontal
σ'	Effective stress	$\sigma' = \sigma - P$	Annotation applicable to all stress tensors
σ_d	Differential stress	$\sigma_d = (\sigma_1 - \sigma_3)$	Difference between σ_1 and σ_3
σ_n	Normal stress	$\sigma_n = \sigma cos^2\theta$	Stress component acting perpendicular to a plane
τ	Shear stress	$\tau = (\sigma \sin 2\theta)/2$	Stress component acting parallel to a plane
R	Reactivation	$R = (1 + \mu cot\theta) / (1 - \mu tan\theta)$	Stress ratio for reactivation
μ	Coefficient of friction	$\mu = R/N = \tau / \sigma_n$	A ratio, ca. $0.2 < \mu < 0.75$ for fault rocks/gouges
φ	Angle of internal friction	$\varphi = \tan^{-1}(\mu)$, $\mu = \tan(\varphi)$	
F	Frictional resistance to sliding	$F \leq \tau = \mu \sigma_n$	Proportional to normal stress and/or coefficient of friction
θ	Angle of intersect	Angle	Between the normal to a plane and σ_1, proxy for dip angle
P	Pore pressure		Pressure in the fluid in pore spaces, in MPa
CPP	Critical perturbation pressure	ΔP	The extra amount of pore fluid pressure required to put a fault into a critically stressed state
T	Tensile rock strength	$T \approx C/2$	The inherent tensile strength of a rock, in MPa
C	Cohesive rock strength	$C \approx 2T$	The inherent shear strength of a rock, in MPa
λ	Wavelength	m	Length of the acoustic wave, in metres
ν	Seismic velocity	ms^{-1}	Increases with depth, in milliseconds
f_d	Dominant frequency	s^{-1}	Of the seismic signal, in Hz

Appendix B

Detailed fault reactivation analysis for the Drake interval, generated by the Stress Analysis tool in the Move software. Included in this appendix are the results from slip tendency, dilation tendency and slip stability.

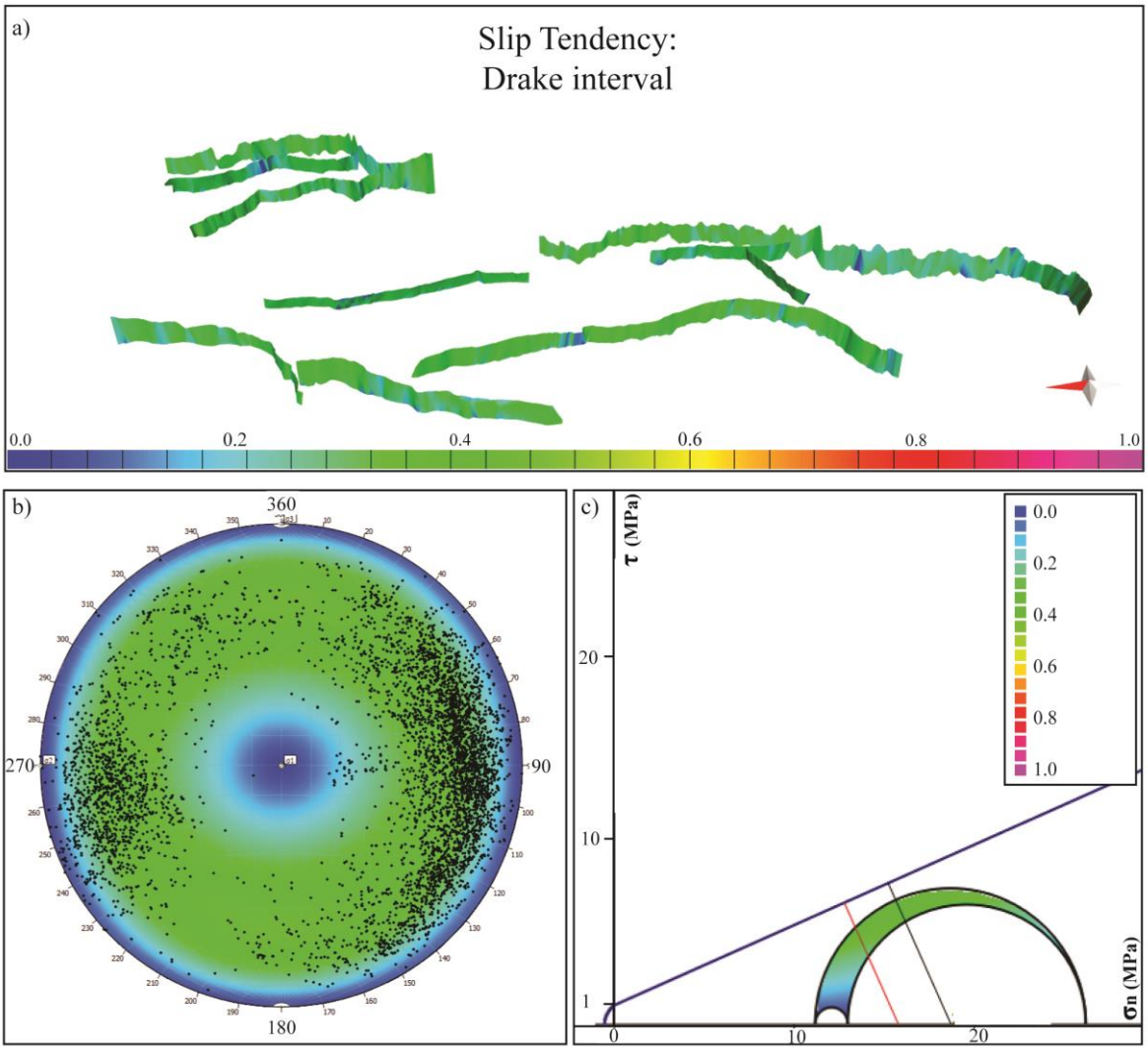

Appendix B.1: Slip tendency (T_s) analysis of the Drake interval showcasing: a) all Drake interval fault segments, b) polar diagram of slip tendency with dip orientations displayed as black dots, c) Mohr-Coulomb diagram of the in-situ stresses acting on the fault surfaces. The colour draping is the same in a) and b) as the colour bar in c). Note the vast abundance of T_s values ranging between 0.2-0.4.

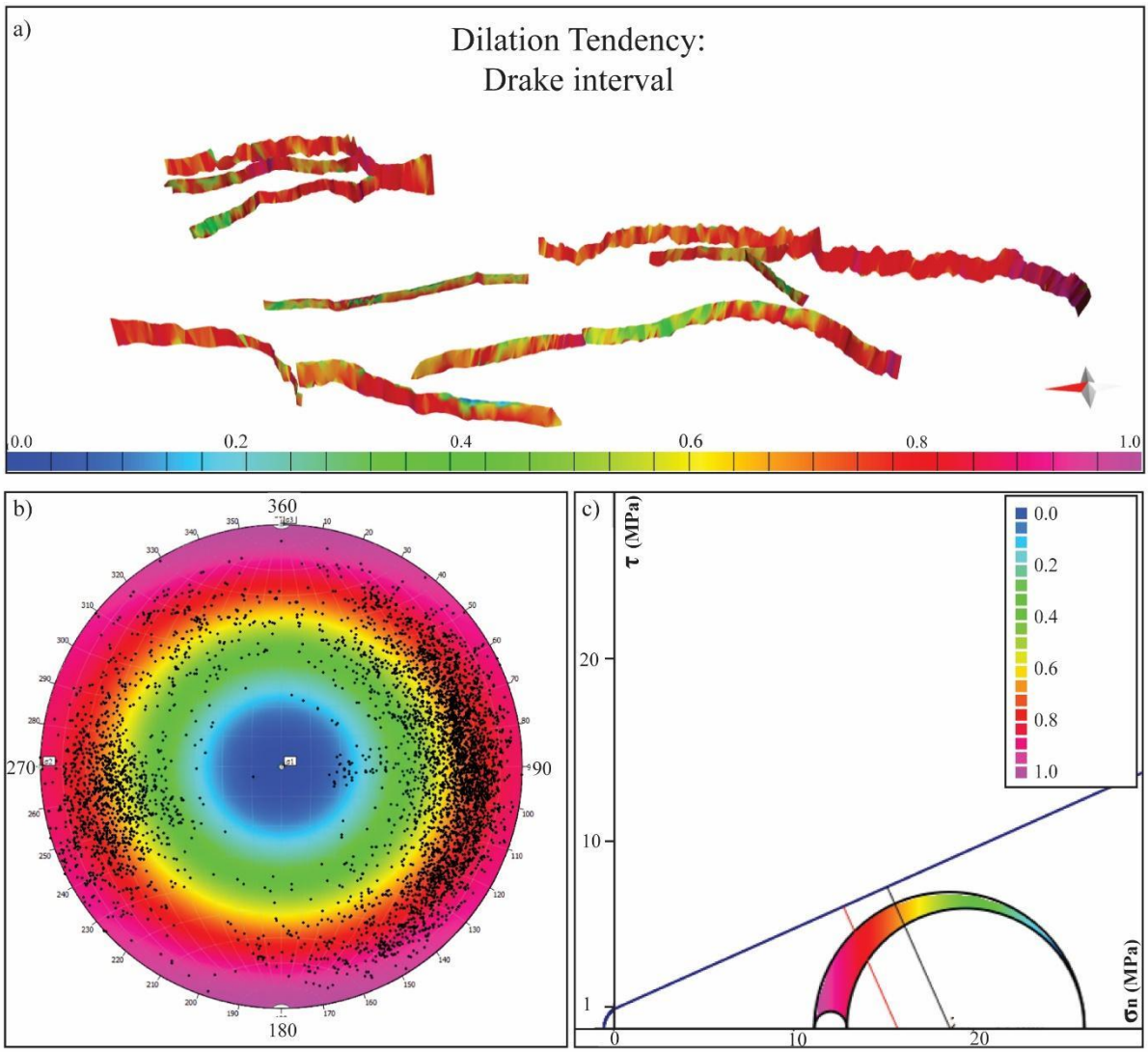

Appendix B.2: Dilation tendency (T_d) analysis of the Drake interval showcasing a) all Drake interval fault segments, b) polar diagram of dilation tendency with dip orientations displayed as black dots, c) Mohr-Coulomb diagram of the in-situ stresses acting on the fault surfaces. The colour draping in the same in a) and b) as the colour bar in c). Values are given in CPP (MPa), the amount of extra pore pressure needed to put the fault into a critically stressed state (see chapter 3).

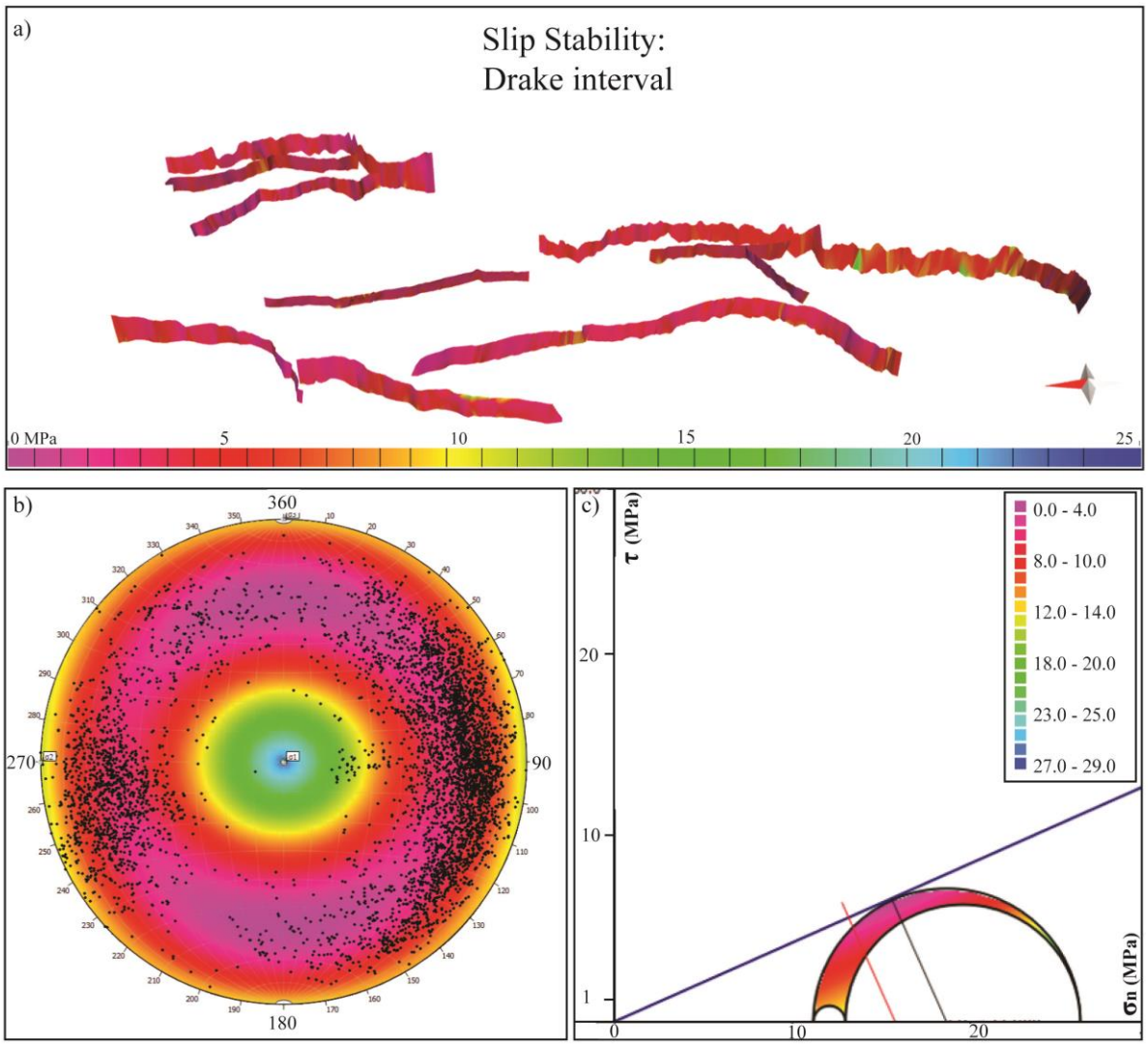

Appendix B.3: Slip stability (S_s) analysis of the Drake interval showcasing a) all Drake interval fault segments, b) polar diagram of slip stability with dip orientations displayed as black dots, c) Mohr-Coulmb diagram of the in-situ stresses acting on the fault surfaces. Note that slip stability considers scenarios without cohesion (c)), and that the colour scale is different in a) than in b) and c) due to limitations in Move's Stress Analysis tool.